Active Region Doping Strategies in O-band InAs/GaAs Quantum-Dot Lasers

Lydia Jarvis

School of Physics and Astronomy Cardiff University

A thesis submitted as partial fulfilment for the degree of

Doctor of Philosophy

June 2022

Abstract

Three techniques for improving gain in InAs quantum dot lasers are examined.

Silicon photonics is a promising solution for meeting increasing global data bandwidth demands. However, silicon itself is a poor emitter due to its indirect bandgap. One potential candidate for light sources for on-chip devices is the monolithic growth of III-V quantum dot materials onto silicon, however, III-V quantum dot materials exhibit reduced gain due to the differences in the population of electron and hole states and ultimately because of the difference in electron and hole effective masses.

P-type modulation doping is a well-established strategy for improving gain in InAs quantum dot lasers on both native GaAs and silicon substrates. The doping density and positioning is optimised for a given wafer design, and ground state lasing at room temperature for a 400μm lasing cavity is demonstrated, in addition to reduced sensitivity of threshold current to temperature.

Optimized p-type modulation doping is compared to a relatively new approach to enhancing gain – direct n-type doping of the quantum dots. It is found to improve the gain in low loss operation, unlike p-type modulation doping. However, direct n-type doping detrimentally showed increased threshold current dependence compared with p-type modulation doping and decreased the maximum temperature at which ground state lasing could be attained.

A novel third method is investigated in which both p-type modulation doping and direct n-type doping are applied to a device simultaneously, referred to as co-doping. Co-doping reduced the threshold current density from 245Acm^{-2} to 132Acm^{-2} at 27 °C and 731Acm^{-2} to 312Acm^{-2} at 97 °C, compared to undoped devices. The reduction was greater than for either individual doping strategy alone. Co-doping also retained the beneficial reduction in the sensitivity of the threshold current density to temperature provided by the p-type modulation doping.

Contents

Papers and Conferences

Papers

H. Deng*, L. Jarvis*, Z. Li*, Z. Liu*, M. Tang, K. Li, J. Yang, B. Maglio, S. Shutts, J. Yu, L. Wang, S. Chen, C. Jin, A. Seeds, H. Liu, and P.M. Smowton, "The role of different types of dopants in 1.3 μm InAs/GaAs quantum-dot lasers," Journal of Physics D: Applied Physics, vol. 55, no. 21, p. 215105, May 2022

*These authors contributed equally to this paper.

Conference Papers

B. Maglio, L. Jarvis, C. P. Allford, SJ. Gillgrass, S. Shutts, M. Tang, H. Liu, P. M. Smowton, "The limits to peak modal gain in p-modulation doped indium arsenide quantum dot laser diodes," 2021 IEEE Photonics Conference (IPC), 2021

J. Mahoney, P. M. Smowton, B. Maglio, L. Jarvis, C. Allford, S. Shutts, M. Tang, H. Liu, and N. Abadía, "QCSE and Carrier Blocking in P-modulation Doped InAs/InGaAs Quantum Dots," Conference on Lasers and Electro-Optics, (CLEO) OSA Technical Digest, 2021

B. Maglio, L. Jarvis, M. Tang, H. Liu and P. M. Smowton, "Modeling the effects of p-modulation doping in InAs quantum dot devices," 2021 International Conference on Numerical Simulation of Optoelectronic Devices (NUSOD), 2021

E. D. Le Boulbar, L. Jarvis, D. Hayes, S. Shutts, Z. Li, M. Tang, H. Liu, A. Samani, P. M. Smowton, and N. Abadía, "Temperature Dependent Behavior of the Optical Gain and Electroabsorption Modulation Properties of an InAs/GaAs Quantum Dot Epistructure," 2019 21st International Conference on Transparent Optical Networks (ICTON), 2019

S. Shutts, C. Spinnler, Z. Li, L. Jarvis, E. D. Le Boulbar, D. Hayes, M. Tang, H. Liu, P. M. Smowton, "Increasing Maximum Gain in InAs Quantum Dot Lasers on GaAs and Si," 2018 IEEE Photonics Conference (IPC), 2018

Conference Presentations

L. Jarvis, B. Maglio, S. Shutts, A. Enderson, H. Deng, M. Tang, H. Liu, P. M. Smowton, "Co-doping 1.3μm InAs Quantum Dot Lasers with P-type modulation doping and direct N-type doping," SIOE, UK, 2022

B. Maglio, L. Jarvis, M. Tang , H. Liu, P. M. Smowton, "Predicting limitations to the performance of p-modulation doped InAs/InGaAs quantum dot lasers and modulators," SIOE, UK, 2022

L. Jarvis, B. Maglio, S. Shutts, Z. Li, H. Deng, M. Tang, H. Liu, P. M. Smowton, "Active region doping strategies in O-band InAs/GaAs quantum-dot lasers," Photonics West, US, 2022

L. Jarvis, B. Maglio, C. P. Allford, Z. Li, S. Shutts, M. Tang, H. Liu and P. M. Smowton, "Increasing Gain in p-modulation doped InAs Quantum Dot Lasers," Photonics West, US, 2020

L. Jarvis, S. Shutts, M. Tang, H. Liu and P. M. Smowton, "Temperature Dependant Characteristics of P-doped Laser Devices," UK Semiconductors, UK, 2019

L. Jarvis, S. Shutts, C. Spinnler, J. Wu, M. Tang, H. Liu, and P. M. Smowton, "The effects of P-doping on 1.3μm quantum dot lasers grown on GaAs and Si substrates," SIOE, UK, 2018

Conference Posters

F.T. Albeladi, SJ. Gillgrass, T. R. Albiladi, C. P. Allford, L. Jarvis, S. Shutts and P.M. Smowton, "Design of low-loss GaAs based optical waveguides incorporating low-index AlOx layers," SIOE, UK, 2022

List of Figures

List of Tables

Acknowledgements

"No man is an island..." rarely becomes more apparent than when trying to write a summary thanking everyone who has helped them.

Firstly, to my supervisors, Peter Smowton and Sam Shutts; thank you for giving me this opportunity and for all the support you have given me, both academic and otherwise. Your relentlessly positive approach to problem solving is admirable, and I would do well to heed it.

I have gained so much from being part of such an interesting and diverse research group, so to the members of the Cardiff Optoelectronics group who I had the good fortune to share my time here with, I sincerely thank you all. Special thanks to Ben, Joe and Clemens, a finer set of allies in the quest to master the mysteries of p-modulation doping I could not have asked for. And thanks to Peter Blood, whose enthusiasm and help in answering questions both on the mechanisms of p-type modulation doping and the history of the laser have been useful and interesting. In addition I'd like to thank Reem, Curtis and Jack for your engaging discussions, encouragement and excellent company!

As this has been an experimental project, I have benefited from a wealth of technical support. To name a few, Joise Nabliek and Richard Forest, for near endless patience with almost as endless wire bonding. Many thanks to Andrew Harrison and the electronics workshop for expert and expedient repair of the mircostat on multiple occasions.

I would like to acknowledge and thank the support of Rank Prize who awarded me a COVID-19 hardship grant which helped me complete my studies.

My involvement with the wider PGR community was somewhat curtailed due to a certain event of 2020, but persisted in the groupchat "Ladies Wot Science" whose humour and insight have been of great help to me.

Outside of the university, I thank my parents Jos and Richard for their unconditional love and support and for encouraging my love of science from an early age. And for the continuation of this scientific interest, I also have to thank the string of excellent science teachers I have had over the years.

Many thanks go out to friends and acquaintances, old and new, whose faith in me has often far exceeded my own and enabled me to stay the course. My gratitude is more than I could state and if I listed you all it would run on longer than this thesis.

Special thanks go to Cel, Pixie and our fluffiest housemate Nya whose company, particularly over the pandemic, has resulted in this being a much brighter time.

James, you have shared the highs and lows throughout so much of this, I thank you for your council, your companionship and the vast quantities of tea supplied. Your presence is a source of joy and inspiration to me, I love the life we build together.

And finally to Cardiff, the city who has been my home for most of my adult life. The view of the hills looking up the train tracks by the bridge on the way to the physics department has seldom failed to lift my spirits.

No Man is an Island

No man is an island, entire of itself;

every man is a piece of the continent,

a part of the main.

If a clod be washed away by the sea,

Europe is the less,

as well as if a promontory were,

as well as if a manor of thy friend's

or of thine own were.

Any man's death diminishes me,

because I am involved in mankind;

and therefore never send to know

for whom the bell tolls;

it tolls for thee.

John Donne

(1624)

1 Introduction

1.1 Thesis Rational

This thesis contains an examination of three different approaches to improve gain in 1.3μm O-band InAs quantum dot (DQ) lasers. The O-band is a telecommunications band covering wavelengths 1260–1360nm.

These devices are developed for eventual application in silicon photonics. Combining photonics with pre-existing silicon infrastructure has attracted a lot of interest in recent years as a leading candidate for optoelectronic integration with particular focus in communications, computing and sensing applications [1]. Silicon photonics facilitates low cost production of optical devices using standard semiconductor fabrication techniques, and ultimately can be integrated alongside microelectronics on chip. A key driving force behind this research is ever-increasing demands on technology for higher rates of data transmission. This could be realized by the production of optical interconnects that overcome the current bottleneck in high data bandwidths which is currently imposed by electronic interconnects. The information and communications technology sector is comprised of telecommunications networks, data centres and personal electronics use such as mobile telephones and home computers. The sector is projected to take up 21% of the world's electricity demand by 2030 with data centres using up to a third of this [2]. Intel provides a range of commercial silicon based optical transceivers [3], for data communications applications. A monolithically integrated approach should be beneficial in terms of cost, providing satisfactory laser performance can be achieved. Devices are required which can tolerate high temperatures and harsh environments and for high temperature operation, uncooled operation on chip at temperatures up to 80 °C is required.

To move towards the implementation of silicon photonics, further improvements of both passive and active components are required to achieve commercial viability [4, 5]. A particular challenge is the development of suitable laser sources [6, 7, 8]. This work seeks to improve the performance of InAs lasers, to make progress towards lasers suitable for this purpose.

Quantum dot lasers have already successfully been grown on silicon, with long lifetimes [9, 10] and low threshold currents [11]. However, to date the lasing material has had comparatively low gain relative to

quantum well devices grown on native III-V substrates and this leads to issues such as a large increase in operating current at high temperatures. Therefore, these devices have required longer cavity lengths, which becomes a limiting factor for modulation speed. Growing QD devices onto silicon is more complex than growing them on native substrates, therefore the starting point for this project has been to examine structures grown on native III-V substrates to better understand the effects of the doping methods prior to producing devices on silicon.

Due to the lattice mismatch of 4.1% between GaAs and silicon, and a thermal expansion coefficient mismatch of 60% [12], GaAs lasers grown on silicon have high defect densities. The defects act as sites for non-radiative recombination, which causes the defect to propagate [13]. Reduced dislocation densities result in longer lifetimes in GaAs based QD lasers grown on silicon [9].

An experimental approach is employed to investigate and increase the benefits of the doping methods. Successive series of wafers are grown and fabricated into laser devices to compare and understand the impact of the three doping strategies. Results are used to inform further improvements and identify potential uses.

The first approach investigated is p-type modulation doping, which is a well established method to improve gain in III-V materials grown on both native [14, 15] and silicon [11, 16] substrates. Furthermore, p-type modulation doping increases confinement of electrons within the dot, reducing the likelihood of electrons entering defect states [17], which is thought to improve laser lifetime.

A second technique, direct n-type doping, has recently been shown to improve the gain in InAs quantum dot lasers grown on GaAs substrates [18, 19].

A novel technique is then investigated where samples are doped with both direct n-type doping and p-type modulation doping to investigate if the benefits can be conferred simultaneously.

Gain in III-V materials is limited by reduced ground state hole populations. P-type modulation doping adds a thin layer of doped material near to the active region, the additional holes diffuse to the quantum dots and increase the ground state hole population and hence gain. In direct n-type doping, the dopants are added as a flux during dot growth and are incorporated into the dots. The dopants ionize, leaving a

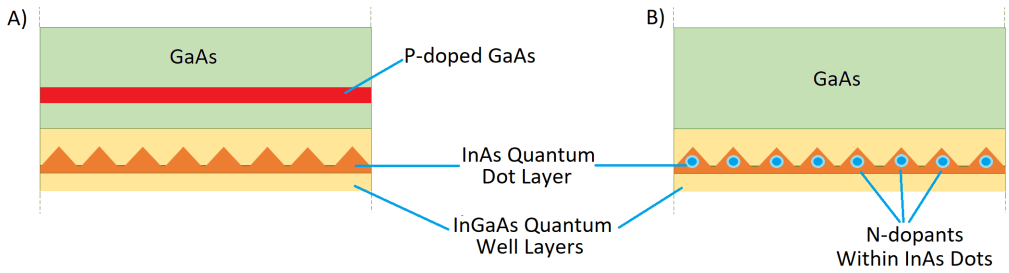

Figure 1.1: Schematic diagram showing an a) p-type modulation doping, b) direct n-type doping.

positive charge in the dot. This alters the dot potential, reducing the number of confined hole states, which increases the ground state hole population as there are fewer states to spread out over. The increase in ground state hole population increases the gain. The implementation of the two doping types are shown in figure 1.1. In the co-doping approach, both techniques are implemented within a single wafer.

A schematic wafer diagram to show the implementation of the three doping types and an undoped reference is given in figure 1.2.

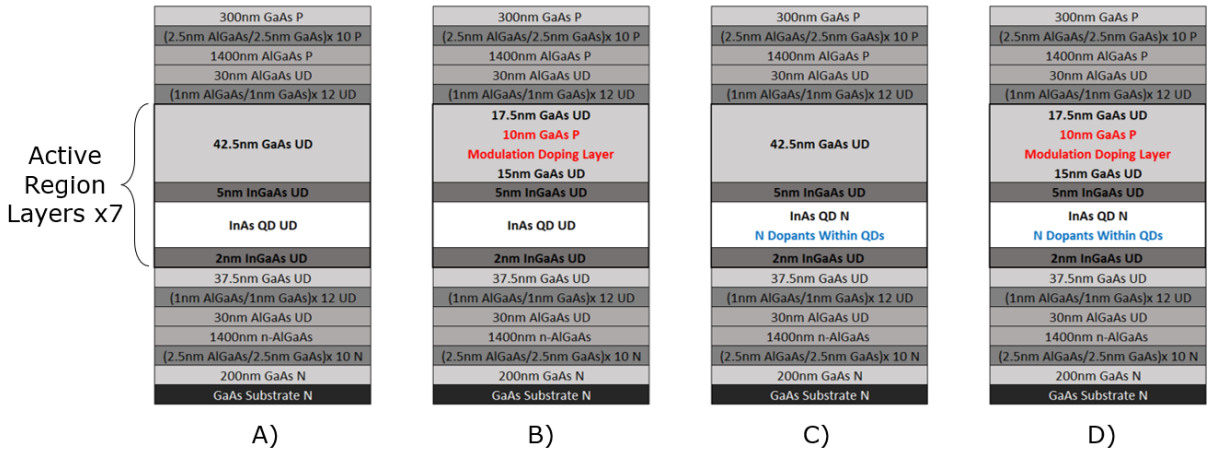

Figure 1.2: Schematic diagram showing an a) undoped, b) p-type modulation doped, c) direct n-type doped and d) p-type modulation and direct n-type co-doped wafer structures.

1.2 Thesis Outline

In Chapter 2, the background physics underpinning this work is discussed, a brief overview of lasing is provided and the limits to gain in III-V materials is discussed in further detail. The impact of p-type modulation doping on the threshold current density is explored and an outline of potential mechanisms are

given, followed by a review of integration platforms and laser lifetimes on silicon. Chapter 3 details the experimental methods and fabrication techniques that are utilized to perform the characterizations of the structures examined in this work. Chapter 4 looks at increasing the benefits of p-type modulation doping, considering first the doping density and then the position and thickness of the p-doped layer. Direct n-type doping is introduced in Chapter 5, the underlying theory is discussed along with current achievements. Then the performance of devices with direct n-type doping are examined and compared with both p-type modulation doped and undoped devices. Results pertaining to a second direct n-type doped wafer set explore the impact of increasing the n-type dopant density. In Chapter 6, the novel co-doping is examined, where samples are doped with both direct n-type doping and p-type modulation doping simultaneously. Conclusions and suggestions for further work are presented in Chapter 7.

1.3 Thesis Context

Within the field, this work presents several original contributions.

There exists numerous studies on p-type modulation doping in devices grown on both GaAs and Si substrates. This is the only work to date that examines the position and the width of the doping layer in nominally identical devices, this is presented in Chapter 4, section 4.3.

This work presents the first study of direct experimental examination of normally identical laser devices with p-type modulation doping and direct n-type doping, which has also been published in the Journal of Physics D [20]. In this thesis, these results are discussed in chapter 5.

Direct n-type doping is a new method, with only two other papers published on the matter. Within the current literature, the impact of performance of multiple doping levels is examined by photoluminescence spectroscopy measurements of wafers only. Here, the characterization of laser devices fabricated from wafers with different doping levels is presented. These results are shown in chapter 5, section 5.6.

Finally, a novel method applying both methods within a singular device is investigated, showing significant improvement over either individual strategy alone, and is presented in chapter 6.

References

[1] A. Rickman. "The commercialization of silicon photonics". In: *Nature Photonics* 8.8 (Aug. 2014).

[2] A. S. G. Andrae and T. Edler. "On Global Electricity Usage of Communication Technology: Trends to 2030". In: *Challenges* 6.1 (June 2015).

[3] *Intel® Silicon Photonics: How Does It Work?* Intel. URL: `https://www.intel.com/content/www/uk/en/architecture-and-technology/silicon-photonics/silicon-photonics-overview.html` (visited on 04/29/2022).

[4] D. Thomson, A. Zilkie, J. E. Bowers, T. Komljenovic, G. T. Reed, L. Vivien, D. Marris-Morini, E. Cassan, L. Virot, J.-M. Fédéli, J.-M. Hartmann, J. H. Schmid, D.-X. Xu, F. Boeuf, P. O'Brien, G. Z. Mashanovich, and M. Nedeljkovic. "Roadmap on silicon photonics". In: *Journal of Optics* 18.7 (June 2016).

[5] D. A. B. Miller. "Device Requirements for Optical Interconnects to Silicon Chips". In: *Proceedings of the IEEE* 97.7 (July 2009).

[6] M. Tang, J.-S. Park, Z. Wang, S. Chen, P. Jurczak, A. Seeds, and H. Liu. "Integration of III-V lasers on Si for Si photonics". In: *Progress in Quantum Electronics* 66 (Aug. 2019).

[7] D. Dai, J. Bauters, and J. E. Bowers. "Passive technologies for future large-scale photonic integrated circuits on silicon: polarization handling, light non-reciprocity and loss reduction". In: *Light: Science and Applications* 1.3 (Mar. 2012).

[8] Z. Zhou, B. Yin, and J. Michel. "On-chip light sources for silicon photonics". In: *Light: Science and Applications* 4.11 (Nov. 2015).

[9] D. Jung, R. Herrick, J. Norman, K. Turnlund, C. Jan, K. Feng, A. C. Gossard, and J. E. Bowers. "Impact of threading dislocation density on the lifetime of InAs quantum dot lasers on Si". In: *Applied Physics Letters* 112.15 (Apr. 9, 2018).

[10] C. Shang, E. Hughes, Y. Wan, M. Dumont, R. Koscica, J. Selvidge, R. Herrick, A. C. Gossard, K. Mukherjee, J. E. Bowers, and J. E. Bowers. "High-temperature reliable quantum-dot lasers on Si with misfit and threading dislocation filters". In: *Optica* 8.5 (May 20, 2021).

[11] S. Chen, W. Li, J. Wu, Q. Jiang, M. Tang, S. Shutts, S. N. Elliott, A. Sobiesierski, A. J. Seeds, I. Ross, P. M. Smowton, and H. Liu. "Electrically pumped continuous-wave III–V quantum dot lasers on silicon". In: *Nature Photonics* 10.5 (May 2016).

[12] S. F. Fang, K. Adomi, S. Iyer, H. Morkoç, H. Zabel, C. Choi, and N. Otsuka. "Gallium arsenide and other compound semiconductors on silicon". In: *Journal of Applied Physics* 68.7 (Oct. 1990).

[13] P. M. Petroff. "Chapter 6 Defects in III–V Compound Semiconductors". In: *Semiconductors and Semimetals*. Ed. by W. T. Tsang. Vol. 22. Lightwave Communications Technology. Elsevier, Jan. 1, 1985.

[14] O. Shchekin and D. Deppe. "Low-threshold high-T0 1.3-μm InAs quantum-dot lasers due to p-type modulation doping of the active region". In: *IEEE Photonics Technology Letters* 14.9 (Sept. 2002).

[15] P. M. Smowton, I. C. Sandall, H. Y. Liu, and M. Hopkinson. "Gain in p-doped quantum dot lasers". In: *Journal of Applied Physics* 101.1 (Jan. 2007).

[16] J. C. Norman, Z. Zhang, D. Jung, C. Shang, M. Kennedy, M. Dumont, R. W. Herrick, A. C. Gossard, and J. E. Bowers. "The Importance of p-Doping for Quantum Dot Laser on Silicon Performance". In: *IEEE Journal of Quantum Electronics* 55.6 (Dec. 2019).

[17] S. Shutts, C. P. Allford, C. Spinnler, Z. Li, A. Sobiesierski, M. Tang, H. Liu, and P. M. Smowton. "Degradation of III–V Quantum Dot Lasers Grown Directly on Silicon Substrates". In: *IEEE Journal of Selected Topics in Quantum Electronics* 25.6 (Nov. 2019).

[18] Z.-R. Lv, Z.-K. Zhang, X.-G. Yang, and T. Yang. "Improved performance of 1.3- μ m InAs/GaAs quantum dot lasers by direct Si doping". In: *Applied Physics Letters* 113.1 (July 2, 2018).

[19] Y.-Q. Qiu, Z.-R. Lv, H. Wang, H.-M. Wang, X.-G. Yang, and T. Yang. "Improved linewidth enhancement factor of 1.3- μ m InAs/GaAs quantum dot lasers by direct Si doping". In: *AIP Advances* 11.5 (May 1, 2021).

[20] H. Deng, L. Jarvis, Z. Li, Z. Liu, M. Tang, K. Li, J. Yang, B. Maglio, S. Shutts, J. Yu, L. Wang, S. Chen, C. Jin, A. Seeds, H. Liu, and P. M. Smowton. "The role of different types of dopants in 1.3 μm InAs/GaAs quantum-dot lasers". In: *Journal of Physics D: Applied Physics* 55.21 (May 26, 2022).

2 Background Theory

2.1 Introduction

This chapter provides an overview of the physics pertaining to the laser devices examined in this work. It starts with a brief description of lasing and gain and InAs quantum dots, which form the active layers for all devices discussed in this work. A more complete overview of the fundamentals of lasing can be found in "Diode Lasers and Photonic Integrated Circuits" by L. Coldren, M. Mashanovitch, and S. W. Corzine [1].

A gain limiting phenomena in III-V semiconductors, valence band asymmetry, is outlined. p-type modulation doping is introduced as a method of countering this. Some of the different theories that exist to explain its impact on the temperature dependant behaviour of threshold current density are discussed.

As these devices are being developed for growth on silicon, a brief outline of silicon photonics is given and some of the challenges of growing on silicon and ways that these issues can be overcome are discussed.

The section concludes with an examination of the mechanisms understood to drive degradation in compound semiconductor lasers and typicalities of the type of study used to investigate laser lifetime and failure, often referred to as live test studies. There is particular interest in operation at high temperatures. Elevated temperatures accelerate many of the degradation mechanisms, ageing the device beyond what it would during standard operation.

2.2 Lasing 101

A laser is a device that produces monochromatic light. The vast majority of the light we see around us, such as sunlight and light from incandescent and LED bulbs, arise from spontaneous emission. Laser light, however, is dominated by stimulated emission, giving laser light unique and beneficial properties. Photons that result from stimulated emission are coherent: identical in frequency, direction, phase, and polarisation. Whereas, photons emitted spontaneously are not coherent.

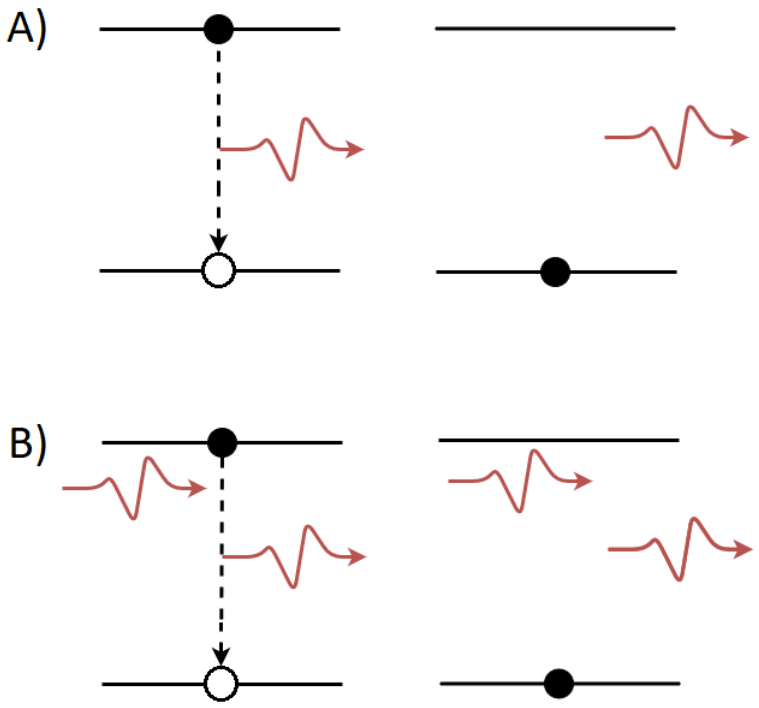

Figure 2.1: A) Spontaneous and B) stimulated (bottom) emission processes between a ground and excited state, during (left) and after (right).

Spontaneous emission occurs when an excited electron spontaneously decays to a lower energy state, emitting a secondary photon with energy equal to the energy separation of the relevant conduction and valence band state.

The valence band is the highest energy level of an atom of any specific material that electrons occupy under no external bias, and the conduction band are the vacant states.

In quantum wells and quantum dots, the energy separation is different to its value as a bulk material as it is affected by quantum confinement effects which arise from the charge carriers being localized to

micrometre and nanometre distances [2]. Smaller structures result in greater increases in energy level spacings [3]. In the process of stimulated emission, an incident photon causes and excited photon to drop to a lower state, emitting a secondary coherent photon. This process only occurs for incident photons with photon energies close to the energy of the energy separation.

To produce light, a laser device needs to emit more photons than are lost to the cavity by absorption. Emitted photons undergo amplification (gain), provided by a gain medium. For the gain medium to enable amplification, and hence emit light, the medium must be in a state of population inversion; a pair of energy states where more charge carriers are in the upper states than the lower state. This is achieved by either electrical or optical 'pumping' of the gain medium, to excite the charge carriers out of the unpumped equilibrium condition.

In most lasing devices, these photons pass many times along a reflective cavity where they initiate further simulated emission events, amplifying the light and providing optical feedback. In laser diodes, photons are emitted from facets that allow a small amount of light to exit, but are mostly reflective. This most basic cavity, consisting of a gain medium and two mirrors, is called a Fabry–Pérot laser [4]. Reflection in a Fabry–Pérot laser only takes place at the mirrors and not within the gain medium.

2.2.1 Gain

Gain is the amount of optical amplification that can be supplied by a material. Unpumped semiconductor material absorbs photons which have energy equal to or greater than the material's bandgap. When the semiconductor material is pumped either optically or electrically, it reaches a point at which the material stops being absorbing to incoming photons. This point is referred to as transparency, and further pumping results in population inversion and optical gain. Net gain means the number of upwards transitions in the lasing system is less than the number of stimulated downward transitions. The number of available transitions is dependent on the relative occupancies of the valence and conduction bands, these can be modeled using Fermi-Dirac statistics and are denoted by f_v and f_c, which are the probability of occupation, with an electron, of the valence state and conduction state respectively.

A thermal distribution of charge carriers can be characterised by a Fermi level. This is the energy level

where the probability of occupancy is 0.5. When the system is pumped, it is displaced from equilibrium. Equilibrium is restored within the bands more quickly than it is between the bands, as the relaxation rate is faster than recombination times. These local equilibria allow for a separate (quasi) Fermi level to be ascribed to each band. When the lattice is in thermal equilibrium the transparency point is equal to the quasi Fermi separation as described by Bernard and Duraffourg in 1961 [5] where it is also shown that the quasi-Fermi separation must exceed the state transition as the condition for population inversion; the minimum condition required for lasing [6].

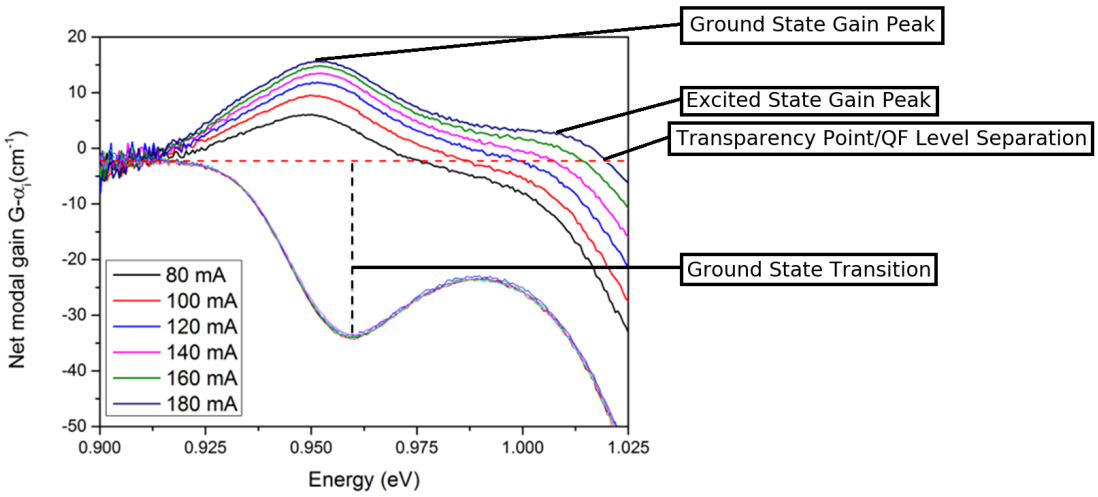

Figure 2.2: Gain and absorption spectra for a InAs quantum dot structure grown on GaAs at a range of currents obtained using the segmented contact method.

The quasi Fermi separation can be found at the convergence of the gain and absorption data, shown in figure 2.2. These spectra were obtained using the segmented contact method, which is described further in section 3.8. Laser operation is determined by the maximal gain for the given current, the peak of maximum gain determines the peak lasing wavelength as the greatest number of photons can be released via stimulated emission with this energy.

For a Fabry–Pérot laser, the threshold gain (g_{th}), where the gain is equal to the cavity loss (α_i), can be calculated mathematically by considering a beam of intensity I_0 making on full 'round trip'. Here, the beam travels along a cavity length L, where a portion of the beam (R_2) is reflected back along the cavity where a portion (R_1) is reflected back to the initial start position by a second mirror as shown in figure 2.3.

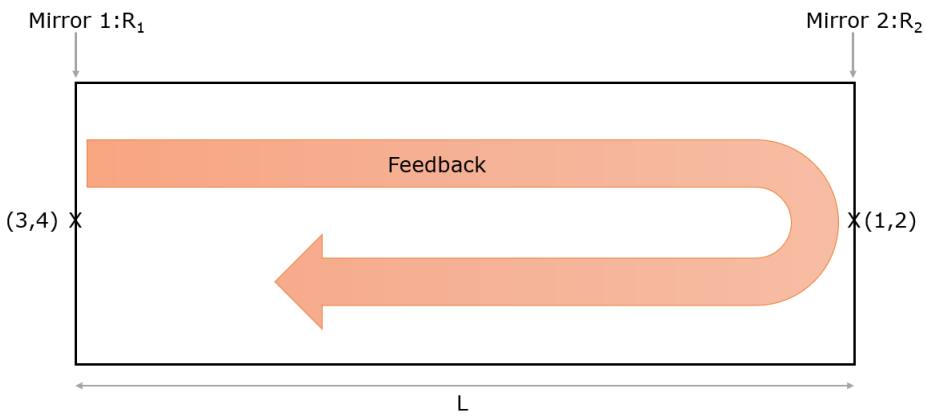

Figure 2.3: Fabry–Pérot laser cavity showing optical feedback.

The locations of the beam as it moves along the cavity are given in figure 2.3. The amplification the beam experiences by the first pass, given by:

$$I = I_0 exp[(g - \alpha_i)L] \tag{1}$$

Which is multiplied by the reflectivity of the mirror to give the intensity at the start of the return pass:

$$I = I_0 exp[(g - \alpha_i)L]R_2 \tag{2}$$

After the beam has returned along the cavity, the intensity is now:

$$I = I_0 exp[(g - \alpha_i)2L]R_2 \tag{3}$$

Where it is reflected by the second mirror to give:

$$I = I_0 exp[(g - \alpha_i)2L]R_1R_2 \tag{4}$$

In the steady state condition, there is no change in the beam intensity, so equating the intensity, I, in equation 4 to I_0 and rearranging to solve for g, which under these conditions is the threshold gain (g_{th}):

$$g_{th} - \alpha_i = (1/2L)ln(1/R_1R_2) \tag{5}$$

2.2.2 Threshold Current and Threshold Current Density

2.2.3 Lasing States

In thermal equilibrium, charge carriers occupy the lowest available energy state preferentially. Lasing that occurs by transitions from the first excited state in the conduction band to the ground state (highest level of the valence band) is referred to as ground state lasing. However, past a certain point, the first excited state becomes full and electrons start to populate the next available energy state. Lasing now takes place by transitions from this higher energy state to the ground state, and is referred to as excited state lasing. States in the valence band are often noted as hole states and are given the notation $H_1, H_2 < H_3...$ with H_1 being the highest state in the valence band. For the conduction band, they are referred to electron states and labelled $E_1, E_2, E_3...$ with E_1 being the first excited state. An example of the position of these states can be seen in figure 2.5.

2.3 Quantum Dots

This project will be examining Quantum Dot (QD) lasers, these devices utilize QDs as the active medium in the laser's light emitting region. QDs are nanoparticles: semiconductor particles with sizes in the nanometer range. They have often been referred to as artificial or tuneable atoms, due to the quantum confinement effects that happen due to their scale. This allows properties like wavelength selected for by way of selecting the size and shape of the dot. Three-dimensional confinement leads quantum dots to have a discretized set of states, as opposed to the near continuum, relative to the average energy k_BT [7], found in quantum well and bulk material. The ideal density of states for QD is a delta function, which results in discrete transitions, producing light that is highly monochromatic. Improvements in threshold current, linewidth enhancement factor and temperature insensitivity are demonstrated [8] relative to bulk semiconductor and quantum well lasers.

The lasing material examined in this project has an active region that consists of quantum dots, which

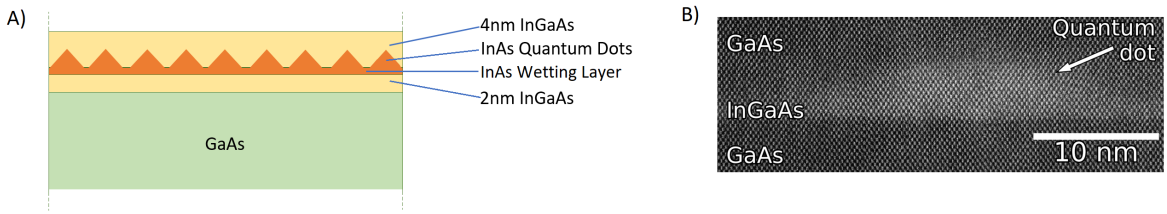

Figure 2.4: A) Schematic diagram of the InAs DWELL system used in this work showing the InAs quantum dot with the wetting layer, InGaAs quantum well layers and GaAs barrier layer and B) atomic resolution scanning transmission electron microscopy image of an InGaAs quantum dot with the wetting layer on a GaAs quantum well layer [9].

form by Stranski–Krastanov growth. In this process, a film is deposited over a substrate, and the lattice mismatch between the film and the substrate leased to the growth of a strained film.

This film usually grows layer by layer until a critical thickness is reached [10]. After this point islands form on top of the deposited film, which serves as a wetting layer, as it is energetically favourable for the higher lattice constant film coalesces via elastic strain relaxation [11]. A schematic diagram and photo of a quantum dot layer in the wetting layer is shown in figure 2.4. This growth method has been shown to form bimodal dot size distributions [12]. This results in distributions centred on two energies, reducing advantages such as the highly discretized emission spectrum that arises from the 3D confinement of the dots. These differences in size and shape of the dots produce inhomogeneous broadening of transitions, which can be seen in the absorption spectra.

For a dot in well (DWELL) system such as those created by Stranski–Krastanov growth, wetting layer states and well states per unit energy can outnumber dot states by three orders of magnitude [7]. In an ideal laser the lasing states would be electronically isolated, however the wetting layer formed has energy levels that are only separated from those of the dot by a few k_BT [13]. As a result of the close spacing, the wetting layer serves as a "reservoir" for the charge carriers, enabling rapid re-distribution. The significantly greater number of wetting layer states have a large influence on the population of the desired dot states. Under bias, this results in the incomplete filling of the dot states. The available gain is reduced as there is a high probability of occupancy in both bands, but poor removal of electrons from the valence band limiting $f_c - f_v$.

The DWELL structure situates the quantum dots within the quantum well layer, both physically and in

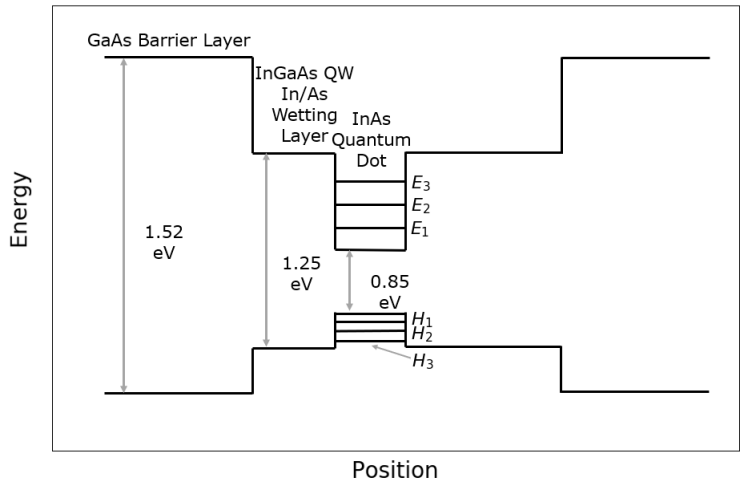

Figure 2.5: Schematic diagram of the InAs DWELL system showing the quantum dot, wetting layers and barrier layers. The first three electron and hole dot states are shown and labeled E_1, E_2, $E_3$and H_1, H_2, H_3.

terms of its energy band gap, offering further advantages in terms of confinement. A schematic diagram of the physical position of the dots and wetting layer for the materials used in the work can be seen in part a) of figure 2.4, part b) shows a scanning transmission electron micrscopy image of a similar DWELL system but with an InGaAs dot on a GaAs well layer. In this work, the DWELL structure is formed by the InAs quantum dot and wetting layer forming within the InGaAs quantum well layers. This is implemented by growing a 2nm InGaAs layer, followed by InAs, which forms a wetting layer and quantum dots via the Stranski–Krastanov process. The dots are then capped with a second InGaAs layer, which forms a continuous electronic level with the first, forming a quantum well. A schematic diagram of the InAs QD/InGaAs QW DWELL energy band diagram is provided in figure 2.5, with the values of the energy gaps provided by [14]. The energy gap of the InAs wetting layer coincides with the energy gap of the wetting layer transition [15].

The schematic diagram of the energy levels in figure 2.5 shows the positions of the different electron (E_1, E_2, E_3) and hole (H_1, H_2, H_3) transitions. The most efficient transition is the lowest energy transition, E_1 to H_1.

2.4 Valence Band Asymmetry

In III-V materials, there is a notable asymmetry between the valence and conduction bands [16]. Electron (conduction) and hole (valence) states have different distributions as they have different effective masses. The conduction band has a substantially smaller density of states, so many populated conduction states lack correspondingly empty valence band states at the same k-value. The limits the available gain as the gain is proportional to the degree of inversion, $f_c - f_v$ [17], and this is maximized when the value is unity, at full inversion between the desired dot states. An example of an $E - k$ diagram for a material with and without valance band asymmetry is shown in figure 2.6.

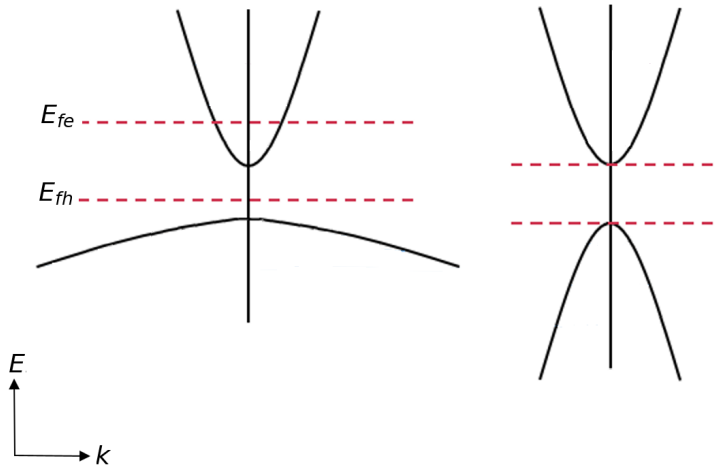

Figure 2.6: E-k diagram and associated quasi-Fermi levels for a typical III-V compound semiconductor and for the ideal case where the conduction and valence bands have equal curvature. E_{fe} and E_{fh} are the quasi-Fermi levels of the electrons and holes respectively.

Quantum dot effective masses serve as an excellent description for charge carrier behaviour in combined bulk / quantum well material. However, quantum dots do not have effective masses. The material that dots are made from have electron and hole effective masses - this leads to the energy level separation when Schrodinger's equation is solved, and this difference in separation is partly responsible for the different movement of the quasi-Fermi levels (when using a quasi-equilibrium model). The derived energy spacing for a 1D infinite potential well is shown in equation 6, a full derivation can be found in [18]. The other factor is the effective electron and hole mass of the wetting layer material, which lead to unequal density of states and provides an additional contribution to the uneven rate of movement of the electron and hole

quasi-Fermi levels as they populate, reducing the available gain.

$$E = \frac{n^2\pi^2\hbar^2}{2mL^2} \tag{6}$$

2.5 Linewidth Enhancement Factor

The linewidth of a laser ($\Delta\nu$) is the width, typically FWHM, of its emission spectrum. Narrow linewidths are required for certain applications including high precision detection, clock synchronization technology and laser radars [19, 20, 21].

The linewidth enhancement factor (LEF), also known as the alpha (Henry) α_H factor, is a measure of the broadening of the linewidth relative to the theoretical minimum. Semiconductor lasers were found to have a much higher linewidth than the theoretically calculated linewidth, the Schawlow–Townes linewidth ($\Delta\nu_{ST}$) [22], which provided a close approximation for many solid state lasers [23]. This discrepancy was found to be proportional to the charge carrier dependant change in gain to the change carrier dependant change in refractive index which is the linewidth enhancement factor, defined by the following equation [6]:

$$\alpha_H = -\frac{4\pi}{\lambda}\frac{dn/dN}{dg/dN} \tag{7}$$

Where dn/dN and dg/dN are the change in refractive index and change in gain that arise from a change in carrier density, dN.

The enhanced broadening from the minimum linewidth is given by equation 8 [24].

$$\Delta\nu = \Delta\nu_{ST}(1 + \alpha_H^2) \tag{8}$$

Low linewidth enhancement factor values have been shown to reduce the degree of filamentation [25], a charge carrier dependent focusing effect, impacting the shape of the nearfield emission of a device [26].

2.6 P-type Modulation Doping

2.6.1 Overview

P-type modulation doping is a well-established used technique to enhance device performance in III-V quantum dot lasers on GaAs substrates [27] and is frequently investigated for quantum dot lasers grown on silicon [28]. P-type modulation doping adds a number of holes close to the device's active region to counter recombination inefficiencies between electrons and holes that are present due to valence band asymmetry described in section 2.4. The additional holes reduce this asymmetry, by increasing the hole population in all valence band states. The increased hole population in the valence band lowers the quasi Fermi levels and improves the number of ground state electrons that can interact with ground state holes, which increases the available gain. The change in carrier distribution within a dot is shown in figure 2.7, the additional holes from the p-doping (red circles) are distributed over the valance states so the population of holes in the ground state is increased. However, the presence of dopants can result in an increase in non-radiative recombination and optical loss [7].

The technique of p-type modulation doping was first suggested for quantum well lasers in 1988 [29] but is more beneficial in quantum dots lasers as the reduced density of states mean that fewer dopants are required to achieve the beneficial effects [6].

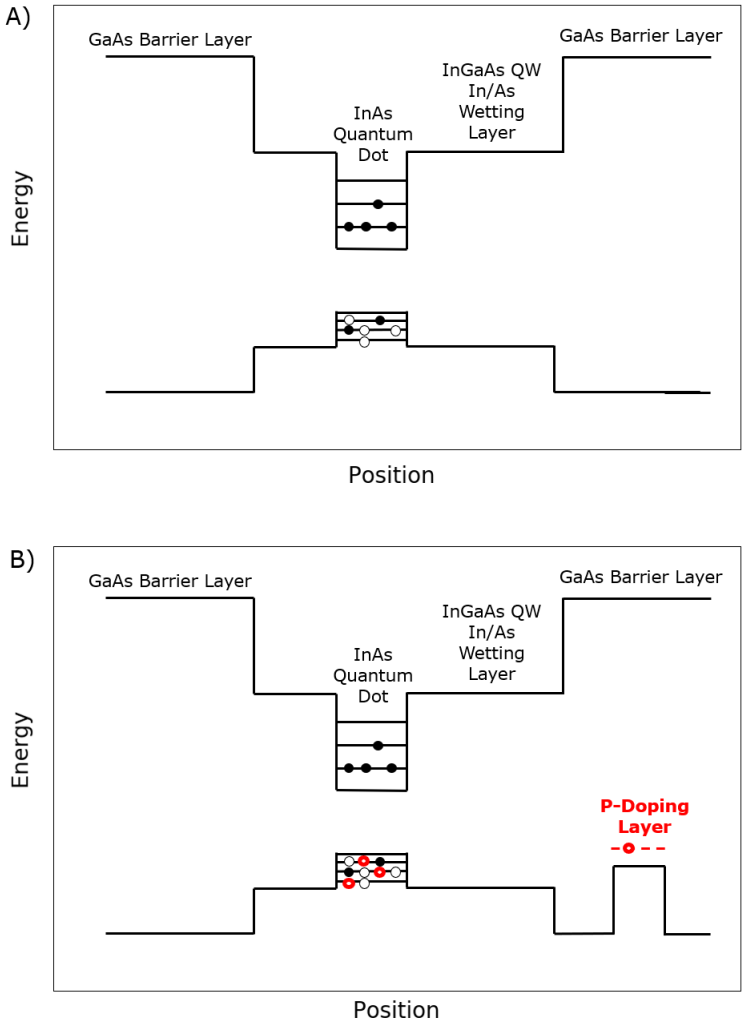

Figure 2.7: Schematic diagram of band structure of a DWELL layer that is a) undoped and b) with p-type modulation doping. Black circles are electrons, white circles are holes and red circles are dopant holes.

Using Nextnano, Benjamin Maglio calculated the full band structure, shown in figure 2.8. A description of using Nextnano software to calculate the band structure, gain and absorption is provided in section 3.2.

The quasi-Fermi levels are lowered in the p-doped case.

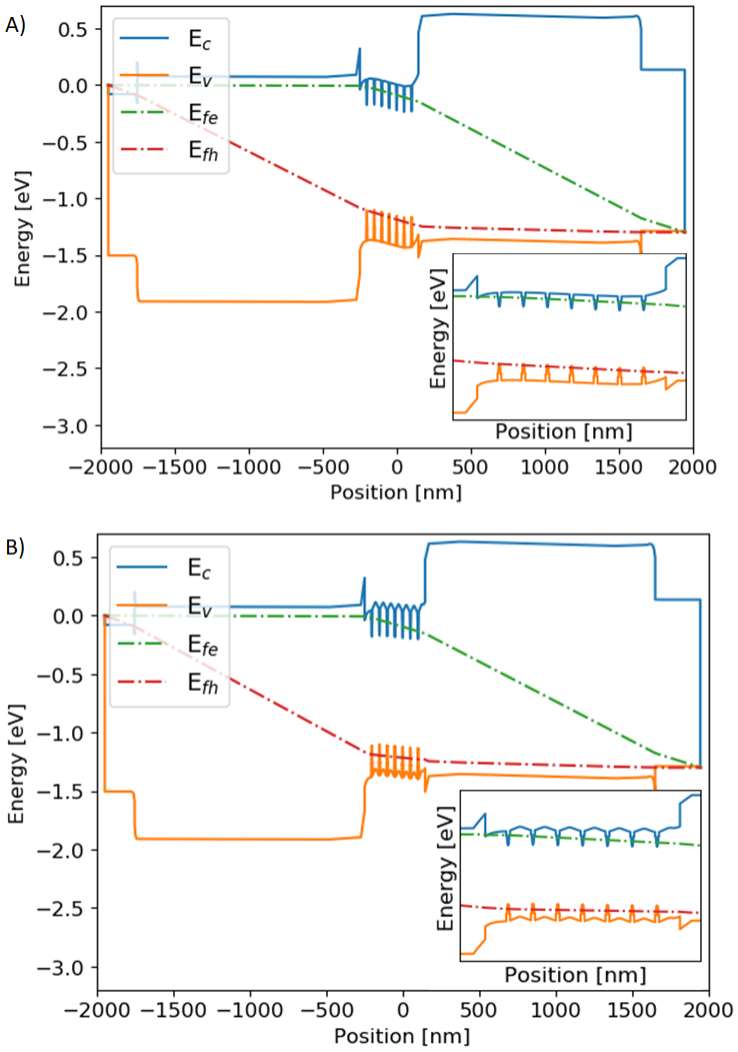

Figure 2.8: Nextnano full device band structure calculation by Benjamin Maglio. Showing a) full laser structure in forward bias for the undoped device, b) device with p-type modulation doping. Here, E_c is the conduction band, E_v is the valence band, E_{fe} is the electron quasi-Fermi level and E_{fh} is the hole quasi-Fermi level.

From this, the degree of inversion between the E_1 and H_1 state is calculated and given in figure 2.9.

Inversion is a measure of the occupancy of the conduction band relative to the valence band ($f_c - f_v$), where 1 is a fully inverted system. The p-doped structure shows an increased inversion up till the point both devices start to saturate.

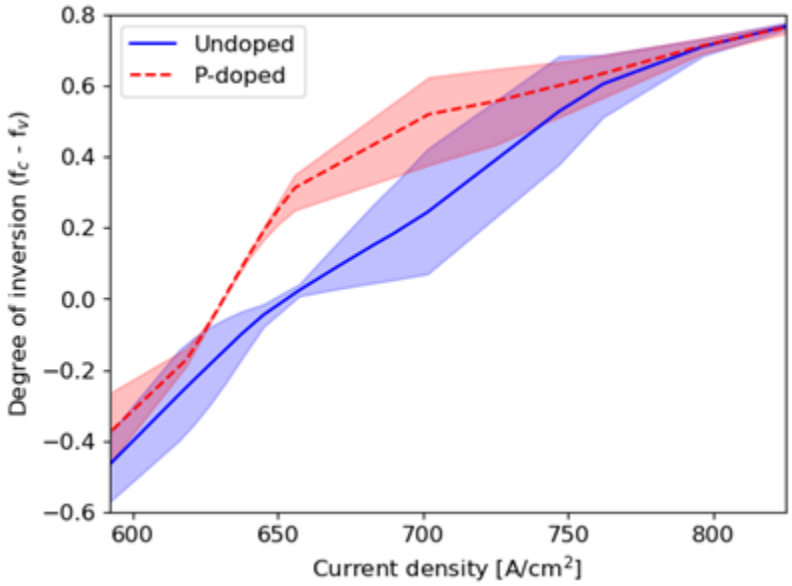

Figure 2.9: Degree of inversion calculated by Benjamin Maglio using Nextnano for the E_1 and H_1 states in each dot layer for undoped and p-doped structures. Solid and translucent lines represent the mean, and the minimum to maximum between the seven layers respectively.

2.6.2 Mechanisms for Temperature Dependence of Threshold Current Density

A threshold current density that changes with temperature in a characteristic manner, leading to a local minimum, is observed in quantum dot lasers [30]. The local minimum in threshold current is often reported at higher temperatures in p-doped samples. The physical mechanisms that cause this characteristic behaviour is highly debated with evidence for a number of models including: additional holes countering the effect of thermal broadening of the holes that arises from the lower density of valance states [31] and coulombic attraction increasing as a result of doping, leading to a greater confinement potential of the electrons within the QDs [32], [33].

Several models focus on non-radiative Auger process, with arguments that focus scattering rate temperature relation [27] and mixed state Auger recombination [34]. Auger recombination is a form of non-radiative recombination where the energy released from an electron-hole interaction is transferred to electrons or holes which is subsequently excited.

A charge carrier distribution model is also considered, with the driving factor behind the threshold dependence being the redistribution of charge carriers. One model claims the process is driven by both

phonon and photon coupling mechanisms [35] and another argues that this process is mediated by phonons [36].

The circumvention of thermal hole broadening [31] (hole broadening being their term for the greater hole energy distribution described in section 2.4) emphasises the way in the additional holes ensure there is adequate population of the ground hole states via the addition of excess holes to enable maximal gain to from the ground state. It was shown that incomplete filling of hole states resulted in gain being achieved via excited state lasing before ground state had fully populated. The temperature dependence is notable as temperature influences population which it determines if the device is operating close to gain saturation [37]. However, this does not provide a full picture, as it does not account for the local reduction threshold current density that is sometimes observed.

2.6.3 Charge Carrier Distribution Model

The case for a charge carrier distribution mediated by phonons was made by O'Driscoll in 2010 [36]. Capitalizing on the bimodal distribution of QDs, the occupancy of two groups of dots could be studied simultaneously. A model was developed that used rate equations coupled with transitions as interactions with a Bose-Einstein distribution of phonons. The results from the model were in good agreement with measured temperature dependence, demonstrating that this is a potential explanation for the behaviour of the threshold current change with temperature.

In this model, the wetting layer holds surplus carriers for the dots, facilitating rapid re-distribution of carriers between dots. This exchange is mediated by the emission or absorption of phonons that have energies equal to the energy separation between dot and wetting layer states, which is of the order of k_BT. As this process is driven by phonons, it is highly temperature dependant. The way in which the carriers are distributed throughout the dot system is most heavily dependent on the rate of carriers moving from the dots into the wetting layer, and the carrier recombination rate. This is because the spontaneous emission of phonons resulting in capture of a carrier into a dot can occur at any temperature but the absorption of phonons and the resultant move of a carrier from the dot into the wetting layer relies on the temperature dependent phonon population.

When the rate of exchange with the wetting layer is greater than the recombination rate, carriers are distributed according to a thermal distribution. Under thermal equilibrium, Fermi-Dirac statistics can be used to describe the distribution of carriers and quasi-Fermi levels for the electrons and holes may be given for the whole set of dot and wetting layer states. However, if recombination rates within the dots are much faster than the thermally driven rate of exchange with the wetting layer, then the distribution of carriers within the QDs becomes non-thermal and in the extreme case random. Here, carriers cannot freely reallocate themselves between dots. In the randomly populated case, the occupation probability uniform, so the system cannot be described by Fermi-Dirac statistics.

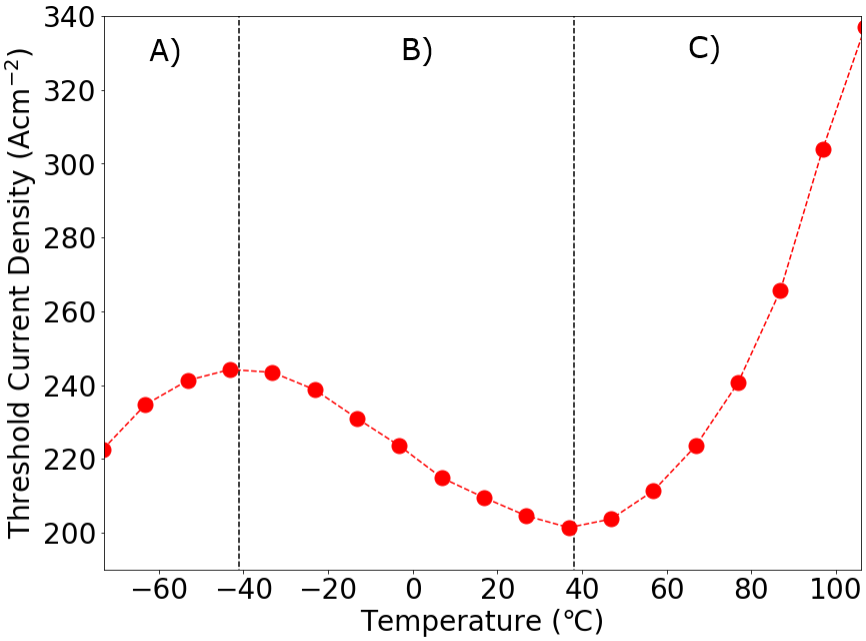

Figure 2.10: Threshold current density as a function of temperature for a QD laser for an uncoated broad area 2000μm long laser with p-type modulation doping , presented in section 4.2.3.

The temperature dependent distribution of carriers can be utilized to explain the temperature dependence of threshold current seen in figure 2.10. Comparable temperature dependencies are found in [35] and [38]. At low temperatures, random, non-thermal distributions, carriers are randomly distributed throughout the dots, requiring high current densities to attain population inversion between desired dot states (A) because all dots, independent of their size, have to reach population inversion at the same time. At higher

temperature, e.g. region (B), randomly distributed carriers gain enough thermal energy to escape from dot states and redistribute to lasing dot states, via the wetting layer. This is a region of temperature and not a single temperature because the differently sized dots have allowed states at different energies below the wetting layer. Threshold continues to decrease as the probability of more of the size distribution gaining sufficient energy to free their captured carriers increases, and the dots with the correct transition energy to take part in the lasing process are filled preferentially. This means lower current densities are needed to attain population inversion for between emitting states. This reaches a local minimum when all are in a thermal distribution, after which (C) the required current increases as the carrier population spreads out in energy according to the thermal distribution.

At higher carrier population, the redistribution of carrier among the dot states occurs at lower temperature as the dot initially fills up from the lowest energy states, which are the furthest from the wetting layer and quantum well states. Higher levels of p-type modulation doping lead to more allowed transitions contributing to gain, which reduces the electron density to achieve lasing. If we assume that it is the electrons that are responsible for the thermalisation process, then modulation p-doping will shift the temperature at which thermalisation occurs to higher temperatures. In the wetting layer states and the dot states, at higher temperature, p-type modulation doping causes excited electron energy states to be relatively depopulated as the quasi-Fermi levels are shifted towards the valence states [7]. Longer cavities require lower threshold carrier densities to lase, as the gain requirement is lower, again leading to the extension of the non-thermal regime to higher temperatures.

When a device is lasing in thermal operation, the stimulated emission rate increases with increasing current, limiting any increase in carrier density. Here, the quasi Fermi levels remain constant or are said to clamp. In a non-thermal distribution, the carrier density in some dots continues to increase because carriers in some dots cannot contribute to the stimulated emission process.

For a random or even a non-thermal distribution of carriers, a broad range of energy states are populated and a broad gain and emission spectrum are produced. Once carriers become thermally distributed, particular emission wavelengths are favoured and the gain and emission spectra narrow.

Some applications of p-type modulation doping do not result in negative threshold dependence [27, 32], here it is likely that increased levels of non-radiative recombination mask the decrease in threshold current, resulting in a threshold that is temperature insensitive over a select range of temperatures.

2.7 Photonic Integrated Circuits (PICs)

Photonic integrated circuits (PICs) utilise photonic signals manipulated by combinations of passive and active components to perform functions on a single chip. They are the optical analogue of the electronic integrated circuit. PICs provide one way of overcoming physical limitations in increasing processing speed, as a result of the integration density in electronic integrated circuits beginning to reach hard limits on the minimum size of transistor, which greatly diminishes return on investment in trying to approach it. [39]. Individual components are often referred to as basic building blocks (BBBs), well understood and characterized individual components that can be used in conjunction to perform more complex functionality.

Passive components include waveguides, multi-mode interferometer (MMI) couplers, spot-size converters, and fibre couplers. Waveguides confine light and allow it to propagate. Optical fibres provide mid and long-range signal transport. Spot size converters couple light from arrays of optical fibres to photonic integrated circuits (PICs) by reducing the beam spread using lithographically defined waveguides. Fibre couplers are devices that split or combine light between two or more fibres or free space.

Active components include lasers, optical amplifiers, and modulators. Modulators modify a property of the beam such as its intensity, phase, or polarization allowing the encoding of information.

PICs attract a lot of research interest and are shown to be promising candidates in a range of applications including sensing [40, 41], especially in biomedical contexts [42, 43] and photonic computing [44] but to date, research has been primarily driven the introduction and scaling of PICs for optical communications [45]. PICs offer strong advantages over electronic integrated circuits, namely higher available speed, large integration capacity, and compatibility with existing processing flows [46].PICs provide opportunities for miniaturisation of bulky optical systems, providing better access to bio-sensing spectroscopy applications

to enable point-of-care diagnostics [47] and size and weight appropriate beam steering for light based sensing systems for utilisation in cars and drones [48].

Many material platforms have been developed for photonics integration, though mainstream PIC platforms are either III-V, IV or a combination of both. PICs grown on III-V materials such as GaAs and InP wafers are technologically mature platforms. InP-based photonic integrated circuits have achieved a high level of integration and enjoy commercial success [49]. They are often utilised as optical communications transmitters and receivers [50]. However, InP is mechanically fragile, therefore not available in large substrates, and is more expensive [51].

Group IV PICs have a significantly less expensive substrates due to the large commercial and natural availability of silicon. The abundance of silicon in the earth's crust is 28%, compared to key compound elements such as gallium and arsenide, which are present in parts per million [52]. Silicon manufacturing has more mature fabrication tools as a result of its ubiquity within the microelectronics industry and larger wafer diameters. Silicon based PICs have attracted a lot of interest due to the potential to integrate them with the currently existing electric integrated circuits. PICs based on solely group IV materials experience challenges in the implementation of active source components due to the indirect bandgap of group IV semiconductors [53].

Current leading platforms for silicon photonic integration is silicon nitride (Si_3N_4), a purely passive platform, its excellent performance makes it ideal for sensing applications [54].

Another competitive platform is silicon on insulator [55], SOI. In this platform, a thin oxide layer is grown over a silicon wafer and a thin layer of silicon on-top. However, it also struggles with active source integration and the oxide layer results in high loss in the mid-infrared region [56] [57].

Germanium lasers with passive silicon is an option but the threshold current is 1000 times higher than III-V based lasers, which is considered to be too high to provide a viable solution [58].

One promising solution is integrating III-V components onto a silicon substrate. Integration on silicon can be achieved via either direct monolithic growth or the transfer and bonding of chips grown on native substrates onto silicon. each of these comes with their own trade-offs and implementation costs. Therefore,

significant focus has been on putting Group III–V semiconductors onto Group IV substrates [49]. The relative size and cost advantages can be seen in table 1 which was adapted from [59].

Material	InP	GaAs	SOI	Si
Substrate Cost ($/cm^2)	4.55	1.65	1.3	0.12
Maximum size (mm)	150	200	450	450

Table 2.1: Approximate minimum cost and maximum diameter of PIC growth substrates: InP, GaAs, SOI and Si.

2.8 Silicon Photonics

Silicon photonics aims to integrate photonic components onto silicon substrates, which are ubiquitous due to their use in microelectronics industry. It is viewed as the greatest opportunity for increasing bandwidth and at low costs. Integration enables direct interface with electronic components and for optical processes to be carried out by the creation of photonic integrated circuits (PICs). It is widely seen as the route to more efficient, cheaper, and scalable data transmission. The improvement in efficiency is achieved by using photonics based devices to process signals as they are capable of much higher switching rates [60], overcoming limitations in the intrinsic speed of electronic translation in copper imposed by electronic transistors and interconnects [61, 62]. Recent work in silicon photonics indicates that devices on this platform offer a competitive alternative to conventional ICs [63, 64, 65, 66, 67].

While good progress has been made in quantum dot lasers grown on silicon, further progress is required to minimise operating current and energy usage requirements, particularly for high temperature operation. The development of active components is technologically immature compared to their passive counterparts [68, 69, 70] due to silicon's suitability for direct implementation of passive structures via silicon-on-insulator (SOI) growth. Whereas silicon itself has challenges as an active medium due to its indirect bandgap. One potential solution is direct growth of III-Vs onto silicon. Quantum dot laser materials that can be grown directly on silicon typically exhibit low gain, leading to issues such as higher current operation and a large increase in operating current at high temperatures (required for uncooled operation on chip). Consequently, longer cavity lengths have been used, which becomes a limiting factor for modulation speed, resulting in a requirement to for improved device performance in this area.

Integration of III-V materials directly on silicon, yielding efficient laser sources that can operate over the full temperature range required and with sufficient reliability, would enable the complete manufacturable silicon photonics platform. Growth of III-Vs on silicon is challenging, as it has a high rate of defects due to mismatches between the lattice and thermal expansion coefficients. Defects negatively impact device performance by acting as traps for charge carriers, increasing the cavity loss and required threshold current. Quantum dots are much better suited for this than quantum wells, as a defect propagating through the active region will interact with a very small number of dots, allowing the majority to lase unaffected. Whereas a defect in a quantum well is more disruptive. P-type modulation doping is an important technique for III-V integration onto silicon, as the doping increases the confinement of change carriers to the dots [71], reducing the probability of electrons moving to defect states.

2.8.1 Overcoming Challenges with Growth on Silicon

The difficulties that arise from growth of III-V semiconductors on silicon stem from mismatches in the lattice and thermal expansion constants; for example, between GaAs and silicon, the discrepancy is 4.1% and 60% respectively [72]. These differences can result in a high defect density.

A number of approaches have been used to reduce or mitigate these effects [71]. Some methods use additional layers between the silicon substrate and III-V material to provide a better growth interface or to form a buffer to reduce strain, reducing the defect density in the subsequent growth.

Quasi 2-dimensional AlAs layers, which suppress 3D growth, to provide a flat layer to help improve the the growth of the QDs [73]. Thin GaP nucleation layers on (001) silicon also help to provide a good surface for subsequent growth by causing growth defects to self-annihilate [74, 75]. Another method involves GaAs grown on v-grooved templates (GoVS) on silicon exactly in the (001) crystal orientation [76]. The grooves encourage the defects that form at the interface to interact with each other and terminate rather than propagate up through the layers.

The use of a ‘virtual’ germanium substrate works as a buffer layer, germanium and silicon is grown with increasing concentration of germanium above the silicon substrate [77] reduces the strain in the GaAs layer as germanium and GaAs have similar lattice constants. Virtual germanium substrates has been very

successful in reducing defect density, however the absorption coefficient of germanium is high for communications frequencies [73] making it less desirable as a strategy for generic integration, but it is appropriate for other applications such as high efficiency solar cells [78].

2.8.2 Lifetime Testing and Degradation

Degradation is often evaluated by examining the rate at which devices deteriorate and what processes cause this. One of the key figures of merit that is considered when looking at degradation is the laser lifetime/extrapolated laser lifetime, typically given as the measured or calculated time for the threshold current to double.

From the late 1980's to around the mid 2000's there was much interest [79] in investigating the potential benefit of growing quantum well lasers on silicon for integration purposes. Devices were shown to have performance similar to those grown on native substrates. However, these devices have had very low extrapolated times to failure, despite decades of research, this figure did not improve beyond a few hundred hours [80], ruling them out as commercially viable.

Devices using quantum dot active layers were anticipated to show improvements as QD photonic devices and have proved to have reduced sensitivity to defects compared to structures made from bulk materials or QWs. Should any defects propagate through the active region, the defects only interact with a small proportion of available quantum dots, leaving plenty intact to provide sufficient gain [73]. The increased strain of the dot layer can cause defect pinning or deflection, as the higher local strain [73] can prevent defects propagating. Another advantage comes from the carrier localization within the dots and hence reduced interaction with the defects [81]. QWs do not deflect dislocations and do not provide carrier localization to the same extent as quantum dots.

Abrupt failure of QD devices in degradation studies [82, 73, 79] are not reported, excluding catastrophic optical damage on the cavity facets and dark-line defects as potential mechanisms. Defects are known to produce pathways for the facilitation of non-radiative recombination. It was observed using transmission electron microscopy that the propagation of defects was occurred due to device operation [83] in a heterojunction GaAs laser. Non-radiative recombination can emit phonons, which are quantized vibrations

of the lattice. This energy dissipates from the defect in a manner that promotes defects [84]. These processes are referred to as recombination-enhanced defect reactions (REDR). Two REDR processes have been found to play a major role in the degradation of devices: recombination-enhanced dislocation glide (REDG) and recombination-enhanced dislocation climb (REDC) [85] The distinction between the two is the direction of the propagation with glide being along the slip plane and climb being perpendicular to this. The slip plane is the plane with the highest density of atoms.

Threading dislocations are defects which extend from the surface of a strained layer, and go through the layers to penetrates the substrate, or bend at the interface into a misfit dislocation [85]. A misfit dislocation is the result of a missing or dangle bond in a lattice. Both are the result of imperfections in the growth. The impact of threading dislocation density (TDD) on laser device lifetimes was investigated, and it was found that a reduction in TDD of x40 was associated with an increase in lifetime of five orders of magnitude [82].

An investigation into the rate of QD laser device degradation in silicon was undertaken by Shutts et al. [71]. The experiment utilized the inverse cavity length dependence of the gain requirement, hence reducing length increases threshold current/carrier density because of the reduced length in which optical amplification can occur. The group found that there was a significantly increased rate of degradation for the shorter devices, i.e. those with higher carrier densities. Shorter devices also showed an increase in optical mode loss, which in turn increased their threshold current requirements, leading to runway style degradation in the shorter (2mm long) device. The optical mode loss was thought to be due to dislocation climb. There was also a notable blue shift in the emitted light due to a greater number of charge carriers, leading to increased population of higher energy states. However, carrier density did not increase to the point where excited state lasing occurred.

A recent study by Buffolo et al. further examines the physical origin of the optical degradation, here REDR was also argued to be the driving mechanism behind the degradation [86].

To examine the impact of threading dislocation on device lifetime, a selection of some of the most comprehensive studies of lifetests is compared in table 2.2 to examine resultant trends.

Year	Description	Extrapolated Laser Lifetime	Jth	Dislocation Density	Ref
2015	InAs/GaAs QDs on Ge/Si, Ridge laser	4600 h, 30 °C, Constant c.w. current x1.75 initial threshold	2000 Acm^{-2}	1x10^6 cm^{-2}	[79]
2016	InAs/GaAs QDs on Si, nucleation layer and dislocation filter layers with in-situ thermal annealing to reduce TDs, Broad area laser	100,158 h, 26 °C Constant c.w. current of 210 mA	60 Acm^{-2}	1x10^5 cm^{-2}	[73]
2018	InAs/GaAs QDs on GaP/Si, Ridge laser	27,000 h, 35 °C, Constant c.w. current, ∼x2 initial threshold current	2000 Acm^{-2}	2x10^8 cm^{-2}	[82]
2018	InAs/GaAs QDs on GaP/Si, InGaAs/GaAs strained layer superlattices as dislocation filter layer, Thermal annealing to reduce TDs, Ridge laser	10x10^6 h, 35 °C, Constant c.w. current stress, ∼x2 initial threshold current	105 Acm^{-2}	7.3x10^6 cm^{-2}	[82]
2021	InAs/GaAs QDs on GaP/Si, InGaAs/GaAs strained layer superlattices as dislocation filter layer, Thermal annealing to reduce TDs, Ridge laser	193,000 h, 80 °C, Constant c.w. current stress, ∼x2 initial threshold current	266 Acm^{-2} (At Room Temperature)	1x10^6 cm^{-2}	[87]

Table 2.2: Comparison of livetest studies of III-V InAs QD lasers grown on silicon substrates.

The fact that the laser with the lowest reported dislocation density does not correspond directly to the highest lifetime could be attributed to a number of possibilities. There is a large amount of uncertainty in measured dislocation density as this is found by counting the observed defects in images taken by electron channelling contrast images and there will be variation in TDD across wafer. In some studies, the time is extrapolated not measured and may not be representative. The results are affected by device geometry, broad area devices create more opportunities for defects to interact with the active region. Variation in the temperature used in the investigation, the threshold current density of the device and selected biasing

condition also reduce the merit of direct comparison, however the device in question was subjected to lower a temperature and current, so these factors would have improved the lifetime relative to the other devices measured.

It seems likely that for devices where there is an appreciable number of carriers populating the 2-dimensional quantum well states degradation will proceed as in a quantum well laser, whereas for devices where all or a high fraction of carriers are localised to the quantum dots, degradation will be slower. While the results [71] are consistent with this idea, lasers of different lengths or ridge widths would differ in charge carrier density potentially producing different results. It would be helpful to gain an understanding of what level of carrier density would be necessary to minimise degradation below an acceptable rate, and therefore what geometric contracts are placed on resultant laser devices.

References

[1] L. A. Coldren, S. W. Corzine, and M. L. Mashanovitch. *Diode Lasers and Photonic Integrated Circuits*. John Wiley & Sons, Mar. 2, 2012. 684 pp.

[2] D. Dorfs, R. Krahne, A. Falqui, L. Manna, C. Giannini, and D. Zanchet. "1.02 - Quantum Dots: Synthesis and Characterization". In: *Comprehensive Nanoscience and Nanotechnology (Second Edition)*. Ed. by D. L. Andrews, R. H. Lipson, and T. Nann. Oxford: Academic Press, Jan. 1, 2011.

[3] G. Schmid. *Nanoparticles: From Theory to Application*. John Wiley & Sons, July 26, 2011. 429 pp.

[4] G. Hernandez. *Fabry-Perot Interferometers*. Cambridge University Press, Aug. 26, 1988. 364 pp.

[5] M. G. A. Bernard and G. Duraffourg. "Laser Conditions in Semiconductors". In: *physica status solidi (b)* 1.7 (1961).

[6] A. Sobiesierski and P. M. Smowton. "6.09 - Quantum-Dot Lasers: Physics and Applications". In: *Comprehensive Semiconductor Science and Technology*. Ed. by P. Bhattacharya, R. Fornari, and H. Kamimura. Amsterdam: Elsevier, Jan. 1, 2011.

[7] P. M. Smowton, I. C. Sandall, H. Y. Liu, and M. Hopkinson. "Gain in p-doped quantum dot lasers". In: *Journal of Applied Physics* 101.1 (Jan. 2007).

[8] P. Blood. *Quantum Confined Laser Devices: Optical Gain and Recombination in Semiconductors.* Oxford University Press, 2015. 433 pp.

[9] Magnunor. *CC BY-SA 4.0, https://commons.wikimedia.org/wiki/File:Gaas$_i$nas$_q$uantum$_d$ot.jpg..* Oct. 22, 2019.

[10] A. Baskaran and P. Smereka. "Mechanisms of Stranski-Krastanov growth". In: *Journal of Applied Physics* 111.4 (Feb. 15, 2012).

[11] J. Venables. *Introduction to Surface and Thin Film Processes.* Cambridge University Press, Aug. 31, 2000. 392 pp.

[12] H. Kissel, U. Müller, C. Walther, W. T. Masselink, Y. I. Mazur, G. G. Tarasov, and M. P. Lisitsa. "Size distribution in self-assembled InAs quantum dots on GaAs (001) for intermediate InAs coverage". In: *Physical Review B* 62.11 (Sept. 15, 2000).

[13] S. A Sobiesierski PM Smowton. *Quantum-Dot Lasers: Physics and Applications.* 2015.

[14] A. Dikshit and J. Pikal. "Carrier distribution, gain, and lasing in 1.3-/spl mu/m InAs-InGaAs quantum-dot lasers". In: *IEEE Journal of Quantum Electronics* 40.2 (Feb. 2004).

[15] I. Sandall, P. Smowton, C. Walker, H. Liu, M. Hopkinson, and D. Mowbray. "Recombination mechanisms in 1.3-μm InAs quantum-dot lasers". In: *IEEE Photonics Technology Letters* 18.8 (Apr. 2006).

[16] E. Yablonovitch and E. Kane. "Reduction of lasing threshold current density by the lowering of valence band effective mass". In: *Journal of Lightwave Technology* 4.5 (May 1986).

[17] P. Blood. "On the dimensionality of optical absorption, gain, and recombination in quantum-confined structures". In: *IEEE Journal of Quantum Electronics* 36.3 (Mar. 2000).

[18] J. H. Davies. *The Physics of Low-dimensional Semiconductors: An Introduction.* Cambridge University Press, 1997.

[19] M. A. Tran, D. Huang, and J. E. Bowers. "Tutorial on narrow linewidth tunable semiconductor lasers using Si/III-V heterogeneous integration". In: *APL Photonics* 4.11 (Nov. 1, 2019).

[20] Z. Bai, Z. Zhao, Y. Qi, J. Ding, S. Li, X. Yan, Y. Wang, and Z. Lu. "Narrow-Linewidth Laser Linewidth Measurement Technology". In: *Frontiers in Physics* 9 (2021).

[21] S. Huang, T. Zhu, M. Liu, and W. Huang. "Precise measurement of ultra-narrow laser linewidths using the strong coherent envelope". In: *Scientific Reports* 7.1 (Feb. 9, 2017).

[22] A. L. Schawlow and C. H. Townes. "Infrared and Optical Masers". In: *Physical Review* 112.6 (Dec. 15, 1958).

[23] M. Osinski and J. Buus. "Linewidth broadening factor in semiconductor lasers–An overview". In: *IEEE Journal of Quantum Electronics* 23.1 (Jan. 1987).

[24] C. Henry. "Theory of the linewidth of semiconductor lasers". In: *IEEE Journal of Quantum Electronics* 18.2 (Feb. 1982).

[25] P. M. Smowton, E. J. Pearce, H. C. Schneider, W. W. Chow, and M. Hopkinson. "Filamentation and linewidth enhancement factor in InGaAs quantum dot lasers". In: *Applied Physics Letters* 81.17 (Oct. 15, 2002).

[26] S. Fathpour, P. Bhattacharya, S. Pradhan, and S. Ghosh. "Linewidth enhancement factor and near-field pattern in tunnel injection In0.4Ga0.6As self-assembled quantum dot lasers". In: *Electronics Letters* 39.20 (Oct. 2, 2003).

[27] S. Fathpour, Z. Mi, P. Bhattacharya, A. R. Kovsh, S. S. Mikhrin, I. L. Krestnikov, A. V. Kozhukhov, and N. N. Ledentsov. "The role of Auger recombination in the temperature-dependent output characteristics (T0=∞) of p-doped 1.3 μm quantum dot lasers". In: *Applied Physics Letters* 85.22 (Nov. 29, 2004).

[28] J. C. Norman, Z. Zhang, D. Jung, C. Shang, M. Kennedy, M. Dumont, R. W. Herrick, A. C. Gossard, and J. E. Bowers. "The Importance of p-Doping for Quantum Dot Laser on Silicon Performance". In: *IEEE Journal of Quantum Electronics* 55.6 (Dec. 2019).

[29] K. J. Vahala and C. E. Zah. "Effect of doping on the optical gain and the spontaneous noise enhancement factor in quantum well amplifiers and lasers studied by simple analytical expressions". In: *Applied Physics Letters* 52.23 (June 6, 1988).

[30] M. Grundmann and D. Bimberg. “Theory of random population for quantum dots”. In: *Physical Review B* 55.15 (Apr. 15, 1997).

[31] O. Shchekin and D. Deppe. “Low-threshold high-T0 1.3-μm InAs quantum-dot lasers due to p-type modulation doping of the active region”. In: *IEEE Photonics Technology Letters* 14.9 (Sept. 2002).

[32] I. P. Marko, N. F. Massé, S. J. Sweeney, A. D. Andreev, A. R. Adams, N. Hatori, and M. Sugawara. “Carrier transport and recombination in p-doped and intrinsic 1.3μm InAs/GaAs quantum-dot lasers”. In: *Applied Physics Letters* 87.21 (Nov. 21, 2005).

[33] T. J. Badcock, R. J. Royce, D. J. Mowbray, M. S. Skolnick, H. Y. Liu, M. Hopkinson, K. M. Groom, and Q. Jiang. “Low threshold current density and negative characteristic temperature 1.3μm InAs self-assembled quantum dot lasers”. In: *Applied Physics Letters* 90.11 (Mar. 12, 2007).

[34] S. Mokkapati, M. Buda, H. H. Tan, and C. Jagadish. “Effect of Auger recombination on the performance of p-doped quantum dot lasers”. In: *Applied Physics Letters* 88.16 (Apr. 17, 2006).

[35] C.-Y. Jin, T. J. Badcock, H.-Y. Liu, K. M. Groom, R. J. Royce, D. J. Mowbray, and M. Hopkinson. “Observation and Modeling of a Room-Temperature Negative Characteristic Temperature 1.3-μm p-Type Modulation-Doped Quantum-Dot Laser”. In: *IEEE Journal of Quantum Electronics* 42.12 (Dec. 2006).

[36] I. O’Driscoll, P. Blood, and P. M. Smowton. “Random Population of Quantum Dots in InAs–GaAs Laser Structures”. In: *IEEE Journal of Quantum Electronics* 46.4 (Apr. 2010).

[37] G. Park, O. Shchekin, and D. Deppe. “Temperature dependence of gain saturation in multilevel quantum dot lasers”. In: *IEEE Journal of Quantum Electronics* 36.9 (Sept. 2000).

[38] R. R. Alexander, D. T. D. Childs, H. Agarwal, K. M. Groom, H.-Y. Liu, M. Hopkinson, R. A. Hogg, M. Ishida, T. Yamamoto, M. Sugawara, Y. Arakawa, T. J. Badcock, R. J. Royce, and D. J. Mowbray. “Systematic Study of the Effects of Modulation p-Doping on 1.3-$\mu\hbox m$ Quantum-Dot Lasers”. In: *IEEE Journal of Quantum Electronics* 43.12 (Dec. 2007).

[39] T. N. Theis and H.-S. P. Wong. “The End of Moore’s Law: A New Beginning for Information Technology”. In: *Computing in Science Engineering* 19.2 (Mar. 2017).

[40] S. Arafin and L. A. Coldren. “Advanced InP Photonic Integrated Circuits for Communication and Sensing”. In: *IEEE Journal of Selected Topics in Quantum Electronics* 24.1 (Jan. 2018).

[41] F. Sang, J. Fridlander, V. Rosborough, S. T. Šuran Brunelli, L. Coldren, J. Klamkin, J. Chen, K. Numata, R. Kawa, and M. Stephen. “Integrated Photonics Technology for Earth Science Remote-Sensing Lidar”. In: *2021 IEEE International Geoscience and Remote Sensing Symposium IGARSS*. July 2021.

[42] E. A. Rank, R. Sentosa, D. J. Harper, M. Salas, A. Gaugutz, D. Seyringer, S. Nevlacsil, A. Maese-Novo, M. Eggeling, P. Muellner, R. Hainberger, M. Sagmeister, J. Kraft, R. A. Leitgeb, and W. Drexler. “Toward optical coherence tomography on a chip: in vivo three-dimensional human retinal imaging using photonic integrated circuit-based arrayed waveguide gratings”. In: *Light: Science and Applications* 10.1 (Dec. 2021).

[43] D. H. Geuzebroek, G. a. J. Besselink, F. Schreuder, F. Falke, A. Leinse, and R. G. Heideman. “Silicon-nitride biophotonic sensing platform”. In: *Integrated Optics: Devices, Materials, and Technologies XXIII*. Vol. 10921. SPIE, Mar. 4, 2019.

[44] W. Bogaerts, D. Pérez, J. Capmany, D. A. B. Miller, J. Poon, D. Englund, F. Morichetti, and A. Melloni. “Programmable photonic circuits”. In: *Nature* 586.7828 (Oct. 2020).

[45] F. Kish, V. Lal, P. Evans, S. W. Corzine, M. Ziari, T. Butrie, M. Reffle, H.-S. Tsai, A. Dentai, J. Pleumeekers, M. Missey, M. Fisher, S. Murthy, R. Salvatore, P. Samra, S. Demars, N. Kim, A. James, A. Hosseini, P. Studenkov, M. Lauermann, R. Going, M. Lu, J. Zhang, J. Tang, J. Bostak, T. Vallaitis, M. Kuntz, D. Pavinski, A. Karanicolas, B. Behnia, D. Engel, O. Khayam, N. Modi, M. R. Chitgarha, P. Mertz, W. Ko, R. Maher, J. Osenbach, J. T. Rahn, H. Sun, K.-T. Wu, M. Mitchell, and D. Welch. “System-on-Chip Photonic Integrated Circuits”. In: *IEEE Journal of Selected Topics in Quantum Electronics* 24.1 (Jan. 2018).

[46] C. Doerr. “Silicon photonic integration in telecommunications”. In: *Frontiers in Physics* 3 (2015).

[47] P. Steglich, G. Lecci, and A. Mai. “Surface Plasmon Resonance (SPR) Spectroscopy and Photonic Integrated Circuit (PIC) Biosensors: A Comparative Review”. In: *Sensors* 22.8 (Jan. 2022).

[48] M. J. R. Heck. "Highly integrated optical phased arrays: photonic integrated circuits for optical beam shaping and beam steering". In: *Nanophotonics* 6.1 (Jan. 6, 2017).

[49] R. Nagarajan, C. Doerr, and F. Kish. "Chapter 2 - Semiconductor Photonic Integrated Circuit Transmitters and Receivers". In: *Optical Fiber Telecommunications (Sixth Edition)*. Ed. by I. P. Kaminow, T. Li, and A. E. Willner. Optics and Photonics. Boston: Academic Press, Jan. 1, 2013.

[50] M. Smit, X. Leijtens, H. Ambrosius, E. Bente, J. van der Tol, B. Smalbrugge, T. de Vries, E.-J. Geluk, J. Bolk, R. van Veldhoven, L. Augustin, P. Thijs, D. D'Agostino, H. Rabbani, K. Lawniczuk, S. Stopinski, S. Tahvili, A. Corradi, E. Kleijn, D. Dzibrou, M. Felicetti, E. Bitincka, V. Moskalenko, J. Zhao, R. Santos, G. Gilardi, W. Yao, K. Williams, P. Stabile, P. Kuindersma, J. Pello, S. Bhat, Y. Jiao, D. Heiss, G. Roelkens, M. Wale, P. Firth, F. Soares, N. Grote, M. Schell, H. Debregeas, M. Achouche, J.-L. Gentner, A. Bakker, T. Korthorst, D. Gallagher, A. Dabbs, A. Melloni, F. Morichetti, D. Melati, A. Wonfor, R. Penty, R. Broeke, B. Musk, and D. Robbins. "An introduction to InP-based generic integration technology". In: *Semiconductor Science and Technology* 29.8 (June 1, 2014).

[51] A. Fontcuberta i Morral, J. M. Zahler, H. A. Atwater, S. P. Ahrenkiel, and M. W. Wanlass. "InGaAs/InP double heterostructures on InP/Si templates fabricated by wafer bonding and hydrogen-induced exfoliation". In: *Applied Physics Letters* 83.26 (Dec. 29, 2003).

[52] M. Fleischer. "The abundance and distribution of the chemical elements in the earth's crust". In: *Journal of Chemical Education* 31.9 (Sept. 1954).

[53] A. Lee, Q. Jiang, M. Tang, A. Seeds, and H. Liu. "Continuous-wave InAs/GaAs quantum-dot laser diodes monolithically grown on Si substrate with low threshold current densities". In: *Optics Express* 20.20 (Sept. 24, 2012).

[54] A. Z. Subramanian, E. Ryckeboer, A. Dhakal, F. Peyskens, A. Malik, B. Kuyken, H. Zhao, S. Pathak, A. Ruocco, A. De Groote, P. Wuytens, D. Martens, F. Leo, W. Xie, U. D. Dave, M. Muneeb, P. Van Dorpe, J. Van Campenhout, W. Bogaerts, P. Bienstman, N. Le Thomas,

D. Van Thourhout, Z. Hens, G. Roelkens, and R. Baets. “Silicon and silicon nitride photonic circuits for spectroscopic sensing on-a-chip [Invited]”. In: *Photonics Research* 3.5 (Oct. 1, 2015).

[55] R. Baets, A. Z. Subramanian, S. Clemmen, B. Kuyken, P. Bienstman, N. Le Thomas, G. Roelkens, D. Van Thourhout, P. Helin, and S. Severi. “Silicon Photonics: silicon nitride versus silicon-on-insulator”. In: *Optical Fiber Communication Conference*. Anaheim, California: OSA, 2016.

[56] J. Chiles and S. Fathpour. “Silicon photonics beyond silicon-on-insulator”. In: *Journal of Optics* 19.5 (Apr. 2017).

[57] W. Bogaerts and S. K. Selvaraja. “13 - Silicon-on-insulator (SOI) technology for photonic integrated circuits (PICs)”. In: *Silicon-On-Insulator (SOI) Technology*. Ed. by O. Kononchuk and B.-Y. Nguyen. Woodhead Publishing, Jan. 1, 2014.

[58] R. E. Camacho-Aguilera, Y. Cai, N. Patel, J. T. Bessette, M. Romagnoli, L. C. Kimerling, and J. Michel. “An electrically pumped germanium laser”. In: *Optics Express* 20.10 (May 7, 2012).

[59] J. E. Bowers, J. T. Bovington, A. Y. Liu, and A. C. Gossard. “A path to 300 mm hybrid silicon photonic integrated circuits”. In: *OFC 2014*. Mar. 2014.

[60] N. Margalit, C. Xiang, S. M. Bowers, A. Bjorlin, R. Blum, and J. E. Bowers. “Perspective on the future of silicon photonics and electronics”. In: *Applied Physics Letters* 118.22 (May 31, 2021).

[61] W. N. Ye and Y. Xiong. “Review of silicon photonics: history and recent advances”. In: *Journal of Modern Optics* 60.16 (Sept. 20, 2013).

[62] G. Roelkens, L. Liu, D. Liang, R. Jones, A. Fang, B. Koch, and J. Bowers. “III-V/silicon photonics for on-chip and intra-chip optical interconnects: III-V/silicon photonics for optical interconnects”. In: *Laser and Photonics Reviews* 4.6 (Nov. 2, 2010).

[63] Z. Zhou, R. Chen, X. Li, and T. Li. “Development trends in silicon photonics for data centers”. In: *Optical Fiber Technology*. Special Issue on Data Center Communications 44 (Aug. 1, 2018).

[64] J. E. Bowers, T. Komljenovic, M. Davenport, J. Hulme, A. Y. Liu, C. T. Santis, A. Spott, S. Srinivasan, E. J. Stanton, and C. Zhang. “Recent advances in silicon photonic integrated circuits”. In: ed. by G. Li and X. Zhou. SPIE OPTO. San Francisco, California, United States, Feb. 13, 2016.

[65] C. Zhang and J. E. Bowers. “Silicon photonic terabit/s network-on-chip for datacenter interconnection”. In: *Optical Fiber Technology* 44 (Aug. 2018).

[66] N. Margalit, C. Xiang, S. M. Bowers, A. Bjorlin, R. Blum, and J. E. Bowers. “Perspective on the future of silicon photonics and electronics”. In: *Applied Physics Letters* 118.22 (May 31, 2021).

[67] W. Bogaerts and L. Chrostowski. “Silicon Photonics Circuit Design: Methods, Tools and Challenges”. In: *Laser and Photonics Reviews* 12.4 (2018).

[68] M. Tang, J.-S. Park, Z. Wang, S. Chen, P. Jurczak, A. Seeds, and H. Liu. “Integration of III-V lasers on Si for Si photonics”. In: *Progress in Quantum Electronics* 66 (Aug. 2019).

[69] D. Dai, J. Bauters, and J. E. Bowers. “Passive technologies for future large-scale photonic integrated circuits on silicon: polarization handling, light non-reciprocity and loss reduction”. In: *Light: Science and Applications* 1.3 (Mar. 2012).

[70] Z. Zhou, B. Yin, and J. Michel. “On-chip light sources for silicon photonics”. In: *Light: Science and Applications* 4.11 (Nov. 2015).

[71] S. Shutts, C. P. Allford, C. Spinnler, Z. Li, A. Sobiesierski, M. Tang, H. Liu, and P. M. Smowton. “Degradation of III–V Quantum Dot Lasers Grown Directly on Silicon Substrates”. In: *IEEE Journal of Selected Topics in Quantum Electronics* 25.6 (Nov. 2019).

[72] S. F. Fang, K. Adomi, S. Iyer, H. Morkoç, H. Zabel, C. Choi, and N. Otsuka. “Gallium arsenide and other compound semiconductors on silicon”. In: *Journal of Applied Physics* 68.7 (Oct. 1990).

[73] S. Chen, W. Li, J. Wu, Q. Jiang, M. Tang, S. Shutts, S. N. Elliott, A. Sobiesierski, A. J. Seeds, I. Ross, P. M. Smowton, and H. Liu. “Electrically pumped continuous-wave III–V quantum dot lasers on silicon”. In: *Nature Photonics* 10.5 (May 2016).

[74] A. Y. Liu, J. Peters, X. Huang, D. Jung, J. Norman, M. L. Lee, A. C. Gossard, and J. E. Bowers. “Electrically pumped continuous-wave 1.3μm quantum-dot lasers epitaxially grown on on-axis (001) GaP/Si”. In: *Optics Letters* 42.2 (Jan. 15, 2017).

[75] K. Volz, A. Beyer, W. Witte, J. Ohlmann, I. Németh, B. Kunert, and W. Stolz. "GaP-nucleation on exact Si (001) substrates for III/V device integration". In: *Journal of Crystal Growth*. 15th International Conference on Metalorganic Vapor Phase Epitaxy (ICMOVPE-XV) 315.1 (Jan. 15, 2011).

[76] Y. Wan, Q. Li, A. Y. Liu, W. W. Chow, A. C. Gossard, J. E. Bowers, E. L. Hu, and K. M. Lau. "Sub-wavelength InAs quantum dot micro-disk lasers epitaxially grown on exact Si (001) substrates". In: *Applied Physics Letters* 108.22 (May 30, 2016).

[77] A. D. Lee, Q. Jiang, M. Tang, Y. Zhang, A. J. Seeds, and H. Liu. "InAs/GaAs Quantum-Dot Lasers Monolithically Grown on Si, Ge, and Ge-on-Si Substrates". In: *IEEE Journal of Selected Topics in Quantum Electronics* 19.4 (July 2013).

[78] R. Ginige, B. Corbett, M. Modreanu, C. Barrett, J. Hilgarth, G. Isella, D. Chrastina, and H. v. Känel. "Characterization of Ge-on-Si virtual substrates and single junction GaAs solar cells". In: *Semiconductor Science and Technology* 21.6 (Apr. 2006).

[79] A. Y. Liu, R. W. Herrick, O. Ueda, P. M. Petroff, A. C. Gossard, and J. E. Bowers. "Reliability of InAs/GaAs Quantum Dot Lasers Epitaxially Grown on Silicon". In: *IEEE Journal of Selected Topics in Quantum Electronics* 21.6 (Nov. 2015).

[80] Z. I. Kazi, P. Thilakan, T. Egawa, M. Umeno, and T. Jimbo. "Realization of GaAs/AlGaAs Lasers on Si Substrates Using Epitaxial Lateral Overgrowth by Metalorganic Chemical Vapor Deposition". In: (2001).

[81] Z. Mi, J. Yang, P. Bhattacharya, G. Qin, and Z. Ma. "High-Performance Quantum Dot Lasers and Integrated Optoelectronics on Si". In: *Proceedings of the IEEE* 97.7 (July 2009).

[82] D. Jung, R. Herrick, J. Norman, K. Turnlund, C. Jan, K. Feng, A. C. Gossard, and J. E. Bowers. "Impact of threading dislocation density on the lifetime of InAs quantum dot lasers on Si". In: *Applied Physics Letters* 112.15 (Apr. 9, 2018).

[83] P. Petroff and R. L. Hartman. "Defect structure introduced during operation of heterojunction GaAs lasers". In: *Applied Physics Letters* 23.8 (Oct. 15, 1973).

[84] J. D. Weeks, J. C. Tully, and L. C. Kimerling. “Theory of recombination-enhanced defect reactions in semiconductors”. In: *Physical Review B* 12.8 (Oct. 15, 1975).

[85] P. M. Petroff. “Chapter 6 Defects in III–V Compound Semiconductors”. In: *Semiconductors and Semimetals*. Ed. by W. T. Tsang. Vol. 22. Lightwave Communications Technology. Elsevier, Jan. 1, 1985.

[86] M. Buffolo, F. Samparisi, C. De Santi, D. Jung, J. Norman, J. E. Bowers, R. W. Herrick, G. Meneghesso, E. Zanoni, and M. Meneghini. “Physical Origin of the Optical Degradation of InAs Quantum Dot Lasers”. In: *IEEE Journal of Quantum Electronics* 55.3 (June 2019).

[87] C. Shang, E. Hughes, Y. Wan, M. Dumont, R. Koscica, J. Selvidge, R. Herrick, A. C. Gossard, K. Mukherjee, J. E. Bowers, and J. E. Bowers. “High-temperature reliable quantum-dot lasers on Si with misfit and threading dislocation filters”. In: *Optica* 8.5 (May 20, 2021).

3 Experimental Methodology

3.1 Introduction

This chapter contains an overview of the techniques and equipment used to model, grow and fabricate laser structures and to collect the data presented in this thesis. Basic information is given about Nextnano, propitiatory software that modelled the band structure of the material, which was used to calculate gain and absorption. The processes for wafer growth and subsequent fabrication into broad area lasers and segmented contact devices are then discussed. Then general testing and screening procedures are described along with specific details of the set-ups used, namely the measuring the near-field, current-voltage-optical power (IVL) and spectral characteristics. Theoretical and experimental details are then given for the segmented contact method for measuring gain and absorption of amplifying material, including details of advantages over competing methods. This is followed by details of how these are modified for an extended temperature range from 200-400K.

3.2 Nextnano Simulations

To understand how the dopant density and position effected the gain, a semi-empirical model was developed by Benjamin Maglio using Nextnano [1] to calculate full device band structures. The structure composition and doping density is entered into the software and some constraints are set using experimentally observed parameters such as wavelength spectrum broadening and the measured band gap. The bands are found by using a Schrödinger-Poisson and current continuity equations in repeated succession until they converge on a self-consistent solution.

Equations were evaluated at a series of points along a grid which was selected by the user, and then the equations are solved using a finite difference approach. In the finite difference approach, the differential components of the equations are replaced with linear finite difference approximations. Unlike differential equations, the linear algebraic equations can be easily solved computationally. The structure is entered into the material database using parameters from the material database and user input. As strain is an integral part of most nanostructures the resultant effect is found by minimising strain for the whole system.

Then the initial charge distribution is set from the valence and conduction band occupancies and fixed quasi-Fermi levels calculated from Fermi-Dirac statistics using donor and acceptor concentrations. The Poisson equation and Schrödinger equations are then solved for that charge distribution. The Poisson equation establishes the potential. From the Schrödinger equation, the energy states and wavefunctions are calculated, finding a new charge carrier distribution. The Poisson equation and Schrödinger are solved iteratively until a self-consistent solution is reached. Then the potential and quantized states fixed and used in the current continuity equation to solve for a new charge distribution, which is fed back to the Schrödinger- Poisson solver until a convergent solution for all three equations is found. Finally, solutions for the bound energy states, wavefunctions, and quasi-Fermi positions are calculated.

These outputs are then used to calculate the gain and absorption. In quantum dots, the three-dimensional confinement results in discrete energy states. In theory these exist at a single energy, however, due to variations in dot size this is inhomogeneously broadened, and the distribution of states can be modelled as a Gaussian distribution. A homogeneous broadening term is approximated by fitting measured absorption spectra, which provides an estimate of the carrier scattering rate. This is typically modelled using a Lorentzian distribution, however, a squared hyperbolic secant function offered superior fit with the experimental results, similarly to [2] and [3]. An experimental factor, γ_b is the combination of the homogeneous and inhomogeneous broadening. Absorption and gain are then calculated using equations expressed by Chuang [4, 5] and Blood [3].

The values used in the model used within this work comes from a combination of those reported in the literature and those measured experimentally by members of the research group. The absorption was measured using the segmented contact method, which is further described in section 3.8. Further details of the modelling process can be found at [6, 7].

3.3 Molecular-Beam Epitaxial Growth

The wafers used in this work were grown by molecular-beam epitaxy (MBE) at UCL. Epitaxy is the process of forming a thin crystal over layer (which can be the same or different to the substrate) which is in registry with the underlying substrate. MBE results in growth that has a high degree of purity and

precision, in both composition and thickness. MBE growth enables growth profile control at nanometer scale [8]. To deposit material, high purity elemental source (effusion) cells, are heated to produce a beam of gaseous atoms which condense on a substrate wafer. This takes place under high vacuum or ultra-high vacuum conditions ($10^{-8} - 10^{-12}$ Torr) to prevent contamination.

Compound materials such as gallium arsenide can be deposited by applying fluxes of gallium and arsenic atoms, which condense on the wafer and react together to form a signal GaAs crystal layer.

Growth is controlled by the substrate temperature, and the deposition rate. The deposition rate is proportional to the temperature of the effusion cell, which changes the rate at which the source undergoes evaporation or sublimation.

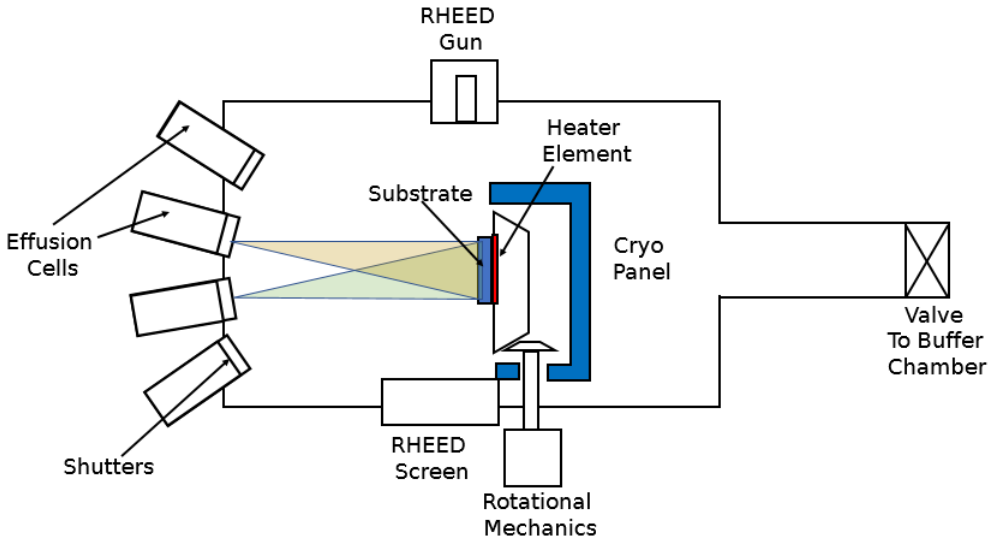

Figure 3.1: Simplified diagram of growth chamber of an MBE system.

Substrate wafers enter the MBE system by a load-lock chamber where the pressure is reduced from atmospheric to 10^{-8} Torr using a scroll pump down to 10^{-2} mbar, with high vacuum by a turbo molecular pump. The chamber is heated to 200 °C to provide preliminary cleaning. By baking the wafers, they are degassed of impurities that have adsorbed to the surface. This reduces contamination in the growth chamber by preventing these species from interfering with the deposition flux or becoming incorporated in the grown crystal.

Samples are then mechanically transferred to a buffer chamber, allowing the growth chamber to be maintained at high vacuum. In the buffer chamber, wafers may be heated to 600 °C for further degassing, and there the pressure is regulated with an ion pump down to pressures of 10^{-10} Torr.

Wafers are then transferred to the growth chamber, a basic diagram is shown in figure 3.1 adapted from [9]. The growth chamber is cooled by liquid nitrogen to facilitate ultra-high vacuum and pressure is reduced to 5×10^{-11} Torr which is generated by a CT-8 cryopump with initial vacuum of 5×10^{-10} Torr generated using turbo pump, ion pump and scroll pump. Within the growth chamber, the wafer is surrounded by cryo-panels which are cooled by a recirculating liquid nitrogen system. This serves to trap gaseous contaminants that are near the wafer, preventing their incorporation in the growth.

The growth is continuously monitored using reflective high energy electron diffraction (RHEED). In this electron scattering methodology, high incident angle electrons graze the growth surface and produce diffraction patterns on a phosphor screen. The resultant patterns offer information about composition and roughness of the growth surface [10]. Furthermore, the change in intensity of the patterns can be calibrated to directly measure the growth rate. Further details of the MBE system used in this work are given in [11].

3.4 Laser Devices

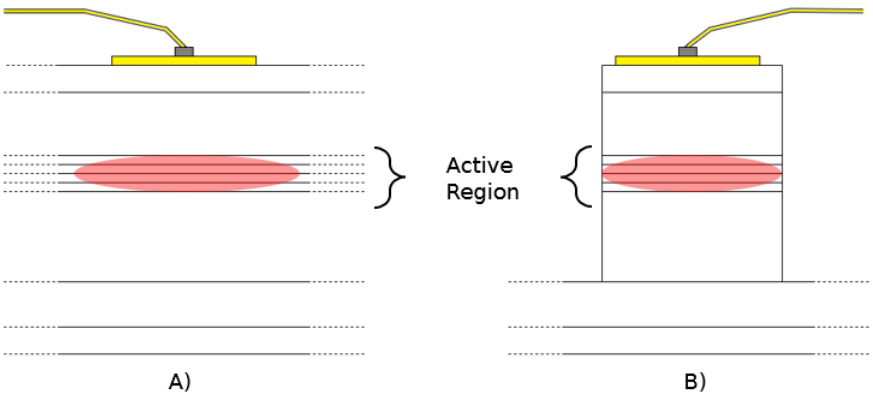

Figure 3.2: Diagram of a) broad area laser and b) ridge laser.

The laser devices examined in this thesis are broad area and ridge devices. The top contact consists of a

gold stripe deposited on top of the chip. The top layer of the structure is highly doped with p-dopant to ensure the forming of a good contact. Current spreads from the top contact, diffusing sideways slightly while moving under the electric field towards the active region. Broad area devices are highly multimodal. Broad area laser devices are often selected for wafer characterization as they do not have additional dependencies such as leakage and recombination in ridge side walls. Ridge lasers reduce the current spreading and increase the localization of the optical mode [3]. A diagram showing both laser structures is given in figure 3.2.

3.5 Laser Device Fabrication

The parent wafer is cleaved into small sections of between 1-4cm^2 for processing and cleaned using a series of solvents, at 80 °C. The contact area is defined by the addition of a top dielectric material, SiO_2, using an electron-beam evaporator. This is then partially removed by photolithography, so the top contact can be applied to a precise area. The first step in the photolithography is to coat the substrate with photoresist with help of a primer to aid surface adhesion. This is deposited as a liquid then spun to distribute a thin layer over the surface and then baked. An opaque metal photomask aligned precisely, and the wafer and the mask are exposed with an ultra-violet (UV) mercury lamp. The wafer is washed in dilute hydrofluoric acid to wash off unexposed photoresist that was under the photomask.

The contacts are then applied using the e-beam evaporator. For the top contact a zinc and gold alloy is used, as it has good adhesion to the p-type GaAs, forming a good ohmic contact. An ohmic contact is important for good change flow between the metal and semiconductor, it is low in resistance and has a linear current–voltage relation. The bottom substrate is lapped to the desired thickness and the bottom contact applied. The n-type GaAs is harder to adhere to, so the contact is comprised of multiple layers. Firstly, a gold and germanium alloy forms the omhic contact, then a layer of nickel is applied to prevent 'balling'. Balling is where the surface stops being continuous, and separate islands form. A final gold layer is applied to help contact with the copper mounting blocks. The wafer is then cleaved to the desired cavity length and mounted on a copper block. The p-contact is connected to a header via gold wire and silver loaded epoxy.

3.6 Measurement Techniques

A low duty cycle is used to prevent self-heating in the device. Unless stated otherwise, this is typically a pulse width of 1000ns with a 5kHz repetition rate, resulting in a duty cycle of 0.005.

3.6.1 Near-field

The near-field of a device refers to the beam profile at the facet. The near-field can tell us a number of things about how a device is operating, for example the degree of current spreading, if lasing is occurring across the full width of the device and how much filamentation is present.

Measuring the width of the near-field allows us to more accurately determine the current density, which is a more useful comparative metric as it is independent of simple geometric factors.

Quantifying the beam width is difficult, as there are a number of ways that this can be done. The ISO standard is to find the maximum value of the beam and find points that at $1/e^2$ the maximum to determine the width [12]. I have elected to use the FWHM to determine the beam diameter as for the beam profiles examined here, as the width from the $1/e^2$ value contains disproportionate contribution from the low intensity tails, which are not representative. This method is used in a number of studies, including [13, 14]. Another common method is to use the contact stripe width or ridge width in the case of ridge lasers [15, 16] to determine the current density or report the threshold current only [17], however this does not take into account current spreading, which is sometime significant.

The measurement is performed using a magnifying lens placed near to the laser and focusing an image of the facet onto an IR camera (Xenics Xeva-163). This is carried out at a current 10% below laser threshold (stated in this thesis as 0.9xi_{th}) to minimise the effect of stimulated emission, which would tend to lead to an underestimate of device width. The line of the nearfield image with the maximal row intensity is found computationally, and the resultant line profile is then used to calculate the full width half maximum. The full width half maximum is measured and then converted from pixels into real units by pumping two lasers simultaneously and as the pitch (space between lasers on a header) is known this can be used as a calibration to convert between pixels and distance.

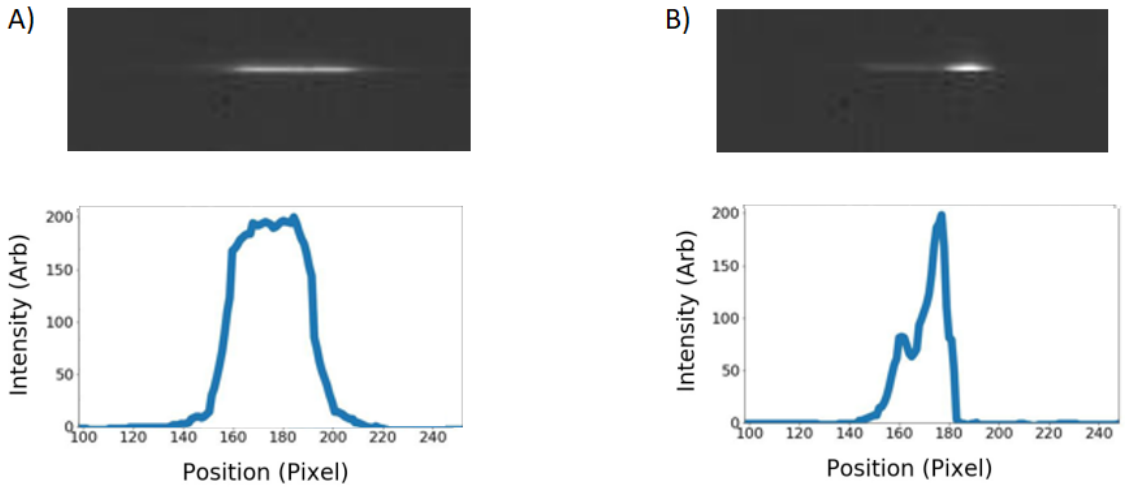

Figure 3.3: Near field IR image (top) and intensity profile (bottom) for a) a good device and b) a device that is not lasing across the full width.

An example of an acceptable profile and a poor near-field, where the device is not lasing across the full width, is shown in figure 3.3. A device is deemed acceptable for further study when emission with a reasonably consistent magnitude is observed across the width of the device. If the device is not lasing on the full width, this could be due to a number of reasons, including poor contact adhesion resulting in uneven pumping of the laser or a crack resulting in a narrower cavity width.

3.6.2 Spectra

Spectra are measured using a Yokogawa AQ6370D spectrum analyzer with a resolution of 0.2nm. The device being tested is either mounted on a temperature controlled stage (ILX Lightwave LDT-5910) or within the microstat discussed in 3.9. The laser beam is focused with a lens onto an input fibre. The spectrum is typically recorded at a current 1.1 times the threshold current (stated in this thesis as 1.1xi_{th}).

3.6.3 IVL

A fundamental measurement of a laser devices are the IVL (current, voltage, light) characteristics. The voltage and light are measured as a function of current and the curves present several key parameters, these include the diode characteristic, the threshold current, and the slope efficiency.

To record these characteristics, a laser mounted on a temperature-controlled stage is pumped using a pulse generator, built in-house at Cardiff University, to step through increasing current and resultant voltage and light outputs are recorded. The light output is measured by an integrating sphere. Both an Ophir 3A-IS and Thorlabs IS145C integrating spheres are used in this work. Current and voltage are measured using an oscilloscope (Tektronix 2024C).

The light-current (LI), also referred to the light-power (PI), curve gives two key figures of merit, threshold current (i_{th}) and external slope efficiency. The threshold current is the point at which the device starts to predominantly emit stimulated photons. The threshold current is found by finding the maxima of the second differential [18]. This can also be found by the first differential, fitting the above and below threshold portions and locating the intercept and taking the second differential of the IV curve [19].

Threshold current is converted into threshold current density (J_{th}), by dividing by the near-field width and stripe length, which is more suited for comparison as it is independent of device geometry.

The slope efficiency $\Delta P/\Delta I$ is found by taking the gradient of the above threshold PI curve and can be converted to external differential efficiency (η_d) using equation 1, which is the ratio of the increase in output photons per second to the increase in number of injected electrons per second. Here h is Planck's constant, ν is the frequency of the laser light and q is the charge of the electron [20]. If the quasi-Fermi levels are pinned [21], equation 2 can be used to find the cavity loss (α_i), and internal quantum efficiency (η_i) which is a measure of the efficiency of a laser device in converting the injected electron hole pairs to emitted photons. Here R is the power reflectivity of the facets (assumed to be equal) and L is the cavity length.

$$\eta_{\mathrm{d}} = \frac{\Delta P/h\nu}{\Delta I/q} \tag{1}$$

$$\frac{1}{\eta_d} = \frac{1}{\eta_i}\left[1 + \frac{\alpha_i}{\ln(1/R)}L\right] \tag{2}$$

3.7 Photoluminese Measurements

Photoluminescence (PL) measurements were taken to investigate the impact of n-doping, discussed in section 5.3. PL uses an external fixed excitation energy, higher than the material's band gap energy, to probe a material's state space. Using a sensor with a variable detection wavelength, from e.g. a monochrometer, we scan through the spectral range of interest to give intensity as a function of wavelength. The FWHM width of this spectrum is a commonly used as a figure of merit to determine the sample inhomogeneity (which is evidenced by the spectral broadening), and is reflective of the size, shape and density of defects. The peak height is also a measure of quality - defects absorb the incoming radiation, and it is emitted non-radiatively, reducing the luminescent intensity. Broader widths are indicative of greater inhomogeneity. The PL measurements were performed at room temperature by Huiwen Deng with a 633-nm laser excitation utilising a Nanometrics RPM 2000 PL Mapper at UCL [22].

3.8 Segmented Contact Method

Material gain was characterised using the segmented contact method [23]. The technique makes use of test structures with equal length segments, shown in figure 3.4 to make comparisons between the measured amplified spontaneous emission.

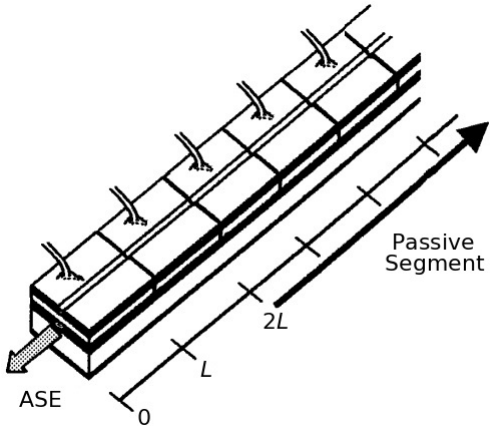

Figure 3.4: Diagram of a segmented contact device, adapted from [2].

This offers a number of advantages over comparable methods. Whilst indirect measurements made from facet measurements do not require separate test structures and the gain can be extracted from laser

measurements [3], known as the 'round trip cavity method' [24], this can only be used if the Fermi level separation clamps above threshold which does not always occur in quantum dot lasers [25]. The Hakki-Poli method is a commonly used method and extracts the ASE by examining interference fringes [26, 27]. To accurately determine this, a high precision spectrometer is essential [3].

True measures of the ASE spectra are very informative in regard to observing the spread of the carriers within the states and can be transformed to give the gain spectra. Test structures are cleaved from the same wafer that is used to make the lasers and the contact is segmented and wired so that the segments can be driven individually, providing representative characterization of the gain material.

The near-field is examined, with both sections one and two biased independently. The near-fields need to be of good quality; showing current is spreading in an even fashion across the width of the device, in a similar manner for both sections. The IV is measured for both sections, both to check for device suitability as good agreement and to provide current compensation using an inline method. Sections with matching IVs indicate that both sections will experience even pumping. The sections experience a leakage current, by fitting the IV below the threshold, the leakage current can be determined above the threshold by extrapolation and added to the desired drive current to achieve the chosen current density within the segment.

The device is mounted on a stage and the gain and absorption are measured for a range of different biasing currents supplied by a pulse generator and measured using a Tektronix TDS 2014C oscilloscope as part of a semi-automated test set up. A computer controlled absorption filter wheel is used to prevent the camera from oversaturation. This is achieved by focusing the incident light onto a monochromator which is then imaged with an IR camera (Xenics XEVA-126), calibrated using a reference. Comparisons between the light emitted by both segments is used to determine the gain and absorption of the material shown in equations 3 and 4, the full derivation is provided in [23].

$$(G - \alpha_i) = \frac{1}{L}\left[\frac{I_{\text{meas}}\,(S12)}{I_{\text{meas}}\,(S1)} - 1\right] \tag{3}$$

$$(A + \alpha_i) = \frac{1}{L}\left[\frac{I_{\text{meas}}\,(S1)}{I_{\text{meas}}\,(S2)}\right] \tag{4}$$

Here, G is the modal gain, A is the modal absorption, α_i is the cavity loss, L is the cavity length and $I_{meas}(S1)$, $I_{meas}(S2)$ and $I_{meas}(S12)$ are the measured ASE intensity spectra with section 1, section 2 and sections 1 and 2 pumped.

3.9 Temperature Dependant Measurements

Below room temperature, temperature dependant measurements were taken using an Oxford instruments MicrostatN cryostat and Oxford Instruments ITC601 temperature controller.

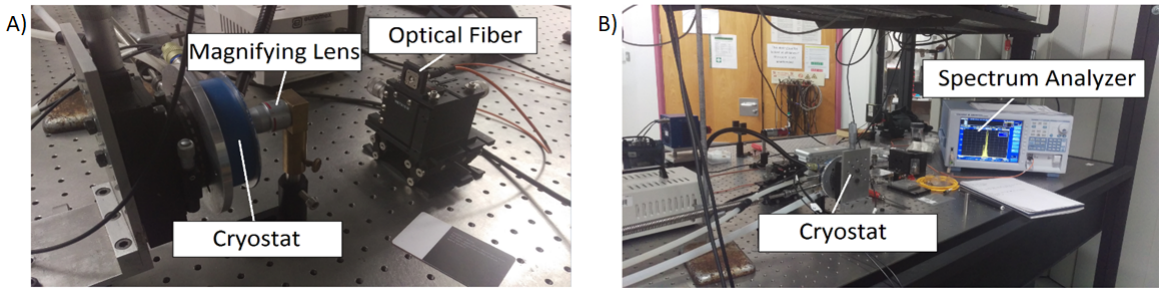

Figure 3.5: Photographs showing the MicrostatN set up for measuring spectra from a) sideview and b) behind.

Devices are mounted in the chamber one or at most two at a time and the chamber is operated at reduced pressure up to 5x10^{-5} mbar. Liquid nitrogen was drawn through the mircostat by a pump, moving LN_2 from a dewar via a transfer tube, though the chamber and out of an outgas line.

3.10 Summary

The methods used to model and characterize semiconductor laser and multi-section devices were described and will be applied in the subsequent chapters to assess the performance of the materials under study.

References

[1] S. Birner, T. Zibold, T. Andlauer, T. Kubis, M. Sabathil, A. Trellakis, and P. Vogl. "nextnano: General Purpose 3-D Simulations". In: *IEEE Transactions on Electron Devices* 54.9 (Sept. 2007).

[2] A. Dikshit and J. Pikal. "Carrier distribution, gain, and lasing in 1.3-/spl mu/m InAs-InGaAs quantum-dot lasers". In: *IEEE Journal of Quantum Electronics* 40.2 (Feb. 2004).

[3] P. Blood. *Quantum Confined Laser Devices: Optical Gain and Recombination in Semiconductors.* Oxford University Press, 2015. 433 pp.

[4] S.-L. Chuang, S. Schmitt-Rink, D. A. B. Miller, and D. S. Chemla. "Exciton Green's-function approach to optical absorption in a quantum well with an applied electric field". In: *Physical Review B* 43.2 (Jan. 15, 1991).

[5] S. L. Chuang. *Physics of Photonic Devices.* John Wiley & Sons, Nov. 7, 2012. 843 pp.

[6] B. Maglio, L. Jarvis, M. Tang, H. Liu, and P. M. Smowton. "Modeling the effects of p-modulation doping in InAs quantum dot devices". In: *2021 International Conference on Numerical Simulation of Optoelectronic Devices (NUSOD).* Sept. 2021.

[7] B. Maglio, L. Jarvis, C. P. Allford, S.-J. Gillgrass, S. Shutts, M. Tang, H. Liu, and P. M. Smowton. "The limits to peak modal gain in p-modulation doped indium arsenide quantum dot laser diodes". In: *2021 IEEE Photonics Conference (IPC).* Oct. 2021.

[8] P. Frigeri, L. Seravalli, G. Trevisi, and S. Franchi. "3.12 - Molecular Beam Epitaxy: An Overview". In: *Comprehensive Semiconductor Science and Technology.* Ed. by P. Bhattacharya, R. Fornari, and H. Kamimura. Amsterdam: Elsevier, Jan. 1, 2011.

[9] H. Adachi and K. Wasa. "1 - Thin Films and Nanomaterials". In: *Handbook of Sputtering Technology (Second Edition).* Ed. by K. Wasa, I. Kanno, and H. Kotera. Oxford: William Andrew Publishing, Jan. 1, 2012.

[10] B. A. Joyce, P. J. Dobson, J. H. Neave, K. Woodbridge, J. Zhang, P. K. Larsen, and B. Bôlger. "RHEED studies of heterojunction and quantum well formation during MBE growth — from multiple scattering to band offsets". In: *Surface Science* 168.1 (Mar. 3, 1986).

[11] M. Tang. "InAs/GaAs Quantum-Dot Light Emitting Sources Monolithically Grown on Silicon Substrates". Doctoral. UCL (University College London), Sept. 28, 2016. 143 pp.

[12] *ISO 11146-1:2021(en), Lasers and laser-related equipment — Test methods for laser beam widths, divergence angles and beam propagation ratios — Part 1: Stigmatic and simple astigmatic beams.* URL: `https://www.iso.org/obp/ui/#iso:std:iso:11146:-1:ed-2:v1:en` (visited on 03/13/2023).

[13] A. Partovi, D. Peale, M. Wuttig, C. A. Murray, G. Zydzik, L. Hopkins, K. Baldwin, W. S. Hobson, J. Wynn, J. Lopata, L. Dhar, R. Chichester, and J. H.-J. Yeh. "High-power laser light source for near-field optics and its application to high-density optical data storage". In: *Applied Physics Letters* 75.11 (Sept. 13, 1999).

[14] P. M. Smowton, E. J. Pearce, and H. C. Schneider. "Filamentation and linewidth enhancement factor in InGaAs quantum dot lasers". In: ().

[15] R. R. Alexander, D. T. D. Childs, H. Agarwal, K. M. Groom, H.-Y. Liu, M. Hopkinson, R. A. Hogg, M. Ishida, T. Yamamoto, M. Sugawara, Y. Arakawa, T. J. Badcock, R. J. Royce, and D. J. Mowbray. "Systematic Study of the Effects of Modulation p-Doping on 1.3-$\mu\hbox m$ Quantum-Dot Lasers". In: *IEEE Journal of Quantum Electronics* 43.12 (Dec. 2007).

[16] Z. Zhang, D. Jung, J. C. Norman, P. Patel, W. W. Chow, and J. E. Bowers. "Effects of modulation p doping in InAs quantum dot lasers on silicon". In: *Applied Physics Letters* 113.6 (Aug. 6, 2018).

[17] Z.-R. Lv, Z.-K. Zhang, X.-G. Yang, and T. Yang. "Improved performance of 1.3- μ m InAs/GaAs quantum dot lasers by direct Si doping". In: *Applied Physics Letters* 113.1 (July 2, 2018).

[18] C. Z. Ning. "What is Laser Threshold?" In: *IEEE Journal of Selected Topics in Quantum Electronics* 19.4 (July 2013).

[19] T. L. Paoli and P. A. Barnes. "Saturation of the junction voltage in stripe-geometry (AlGa)As double-heterostructure junction lasers". In: *Applied Physics Letters* 28.12 (June 15, 1976).

[20] L. A. Coldren, S. W. Corzine, and M. L. Mashanovitch. *Diode Lasers and Photonic Integrated Circuits*. John Wiley & Sons, Mar. 2, 2012. 684 pp.

[21] P. Blood. "Quantum Efficiency of Quantum Dot Lasers". In: *IEEE Journal of Selected Topics in Quantum Electronics* 23.6 (Nov. 2017).

[22] H. Deng, L. Jarvis, Z. Li, Z. Liu, M. Tang, K. Li, J. Yang, B. Maglio, S. Shutts, J. Yu, L. Wang, S. Chen, C. Jin, A. Seeds, H. Liu, and P. M. Smowton. "The role of different types of dopants in 1.3 μm InAs/GaAs quantum-dot lasers". In: *Journal of Physics D: Applied Physics* 55.21 (May 26, 2022).

[23] P. Blood, G. Lewis, P. Smowton, H. Summers, J. Thomson, and J. Lutti. "Characterization of semiconductor laser gain media by the segmented contact method". In: *IEEE Journal of Selected Topics in Quantum Electronics* 9.5 (Sept. 2003).

[24] G. H. B. Thompson, G. D. Henshall, J. E. A. Whiteaway, and P. A. Kirkby. "Narrow-beam five-layer (GaAl)As/GaAs heterostructure lasers with low threshold and high peak power". In: *Journal of Applied Physics* 47.4 (Apr. 1976).

[25] I. P. Marko, A. R. Adams, N. F. Massé, and S. J. Sweeney. "Effect of non-pinned carrier density above threshold in InAs quantum dot and quantum dash lasers". In: *IET Optoelectronics* 8.2 (2014).

[26] B. W. Hakki and T. L. Paoli. "Gain spectra in GaAs double-heterostructure injection lasers". In: *Journal of Applied Physics* 46.3 (Mar. 1975).

[27] D. T. Cassidy. "Technique for measurement of the gain spectra of semiconductor diode lasers". In: *Journal of Applied Physics* 56.11 (Dec. 1984).

4 Increasing Gain in p-type Modulation Doped InAs Quantum Dot Lasers

4.1 Introduction

In chapter 2 Background Theory, it was shown that QD structures grown on silicon can have excellent performance with long lifetimes, to extend this good performance to shorter lasers the optical gain obtainable from the dots should be maximised. This chapter investigates using p-type modulation doping to increase the optical gain. P-type modulation doping is a well established method to improve gain in III-V materials grown on both native [1, 2] and silicon [3, 4] substrates. P-type modulation doping also incurs deleterious effects, causing increases in non-radiative recombination and optical loss [5]. Therefore, p-type modulation doping must be optimised in order to balance the improvement brought about by the extra holes with the penalties incurred [6].

In this chapter, p-type modulation doping is investigated in terms of dopant density and thickness and position of the dopant layer to improve performance, including threshold current density, particularly at higher temperatures and short cavity lengths. This investigation was carried out by utilizing both computational and experimental studies of InAs Quantum Dot lasers on GaAs substrates. For simplicity, the devices examined in this work are grown on native GaAs substrates with a view to future implementation on silicon. Devices containing p-type modulation doping with comparable wafer structures to those discussed in this chapter have been grown on silicon in a collaboration between Cardiff University and UCL [3]. They have demonstrated a device with an excellent lifetime that is competitive with other GaAs lasers grown on silicon, which discussed further in section 2.8.2, demonstrating the suitability of these structures for investigation as light sources for future silicon photonic applications.

Using NextNano [7] software, fellow PhD student Benjamin Maglio performed a study of the position and doping density of beryllium acceptors placed within the active region of multilayer quantum dot lasers. Examples of the modelling process can be found at [8, 9]. Colleagues at UCL grew a number of these designs on GaAs substrates to assess the practical outcomes. Two fabrication runs were utilized, the first

to investigate the doping density and the second to assess the position and thickness of the doping layer. The improved structure achieved high gain structures with ground state lasing at room temperature for an uncoated facet laser with an active region grown with 7 quantum dot layers and cavity length as short as 400μm.

4.2 Investigation of P-Type Modulation Dopant Density

In this section, the level of doping is investigated by characterization of laser devices of various lengths fabricated from four otherwise nominally identical wafers, but with varying levels of P-type modulation doping at the active region: 0, 5, 10 and 15 holes per dot. The resulting effects on the threshold current temperature dependence are non-linear, so to understand them a range of combinations of doping and cavity lengths are examined.

4.2.1 Structures

The wafers used to fabricate the structures examined in this chapter were grown by colleagues at UCL on 3-inch Si-doped GaAs wafers by solid-source molecular beam epitaxy (MBE). Full structure details can be found in figure 4.1. The p-type modulation was applied by the doping of a 10nm GaAs layer, with beryllium, within the 42.5nm undoped GaAs barrier layer, shown on the right in figure 4.1. The dot density was determined by the growth of uncapped test structures that were measured using atomic force microscopy, and it was found that the dot density was 3.6x10^{10}cm^{-2}. Wafers with three different levels doping density and an undoped reference were grown to have a resultant doping density of 0, 5, 10 and 15 holes per dot, referred to hence by the acronym hpd.

Four wafers were grown with 0, 5, 10 and 15hpd respectively. The wafer was fabricated into broad area laser devices at Cardiff by Dr. Zhibo Li and Dr. Samuel Shutts. As-cleaved facets were parallel, flat and reflective to 30% of the light of the lasing wavelength [10]. The pair of cleaved facets formed Fabry–Pérot cavities with lengths (L_c) 1000μm, 2000μm and 3000μm chips to form lasers. The 100μm top stripe gold contact was deposited by E-beam evaporation. These chips were mounted to indium-plated copper heat sinks using silver loaded epoxy and gold-wire-bonded. The details of the fabrication process were

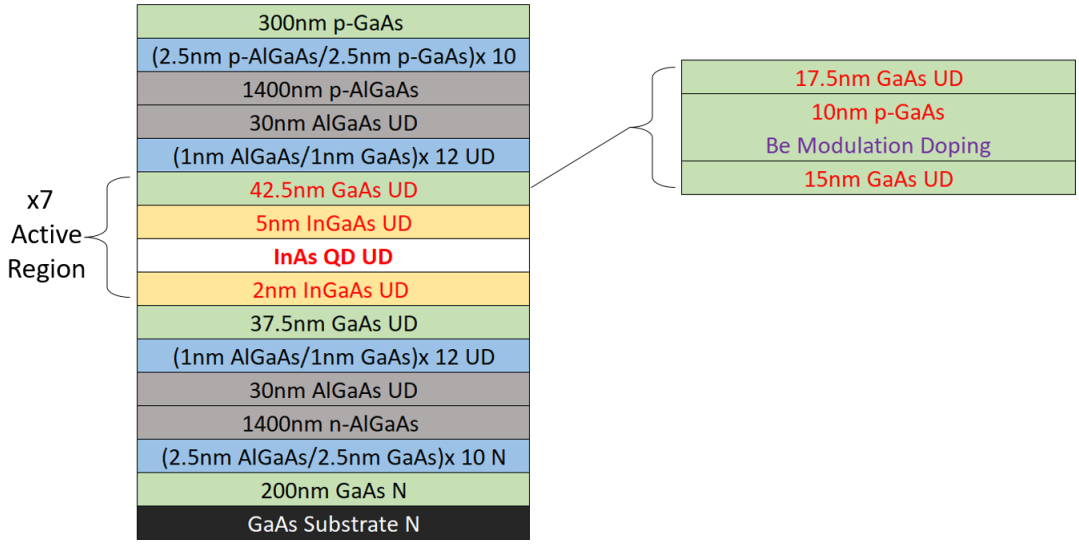

Figure 4.1: Schematic diagram of the wafer (left, not to scale), showing the modified p-type modulation doped GaAs spacer layer (right) for the doped wafers.

communicated to me by discussion and sharing of the clean room process flow sheets for the devices.

Four lasers were fabricated for each permutation of doping and cavity length. All devices were measured at room temperature, and temperature dependant measurements of the two best performing were taken to ensure the result is reproachable. The best performing devices are presented.

4.2.2 Near-Field as a Function Of Temperature

The near-field profile was measured as a function of temperature to assess the current spreading, both to find an indication of the charge carrier distribution behaviour and as a way of determining the effective area of the device to calculate the threshold current density. Devices were placed in the microstat and the near-field width was measured as a function of temperature over the range $-75\,^{\circ}\mathrm{C}$ - $125\,^{\circ}\mathrm{C}$ (200 - 400K).

The trend of all 4 sets of devices showed a narrowing of the nearfield with increasing temperature. In figure 4.2, this is plotted for an undoped device and a device with 15hpd in the active region only, as the graph becomes very difficult to read with all four devices shown on one plot. The room temperature nearfield widths are: undoped: $(103.4 \pm 5.8)\mu$m, 5hpd: $(101.9 \pm 4.2)\mu$m, 10hpd $(97.8 \pm 6.2)\mu$m and 15hpd $(93.7 \pm$

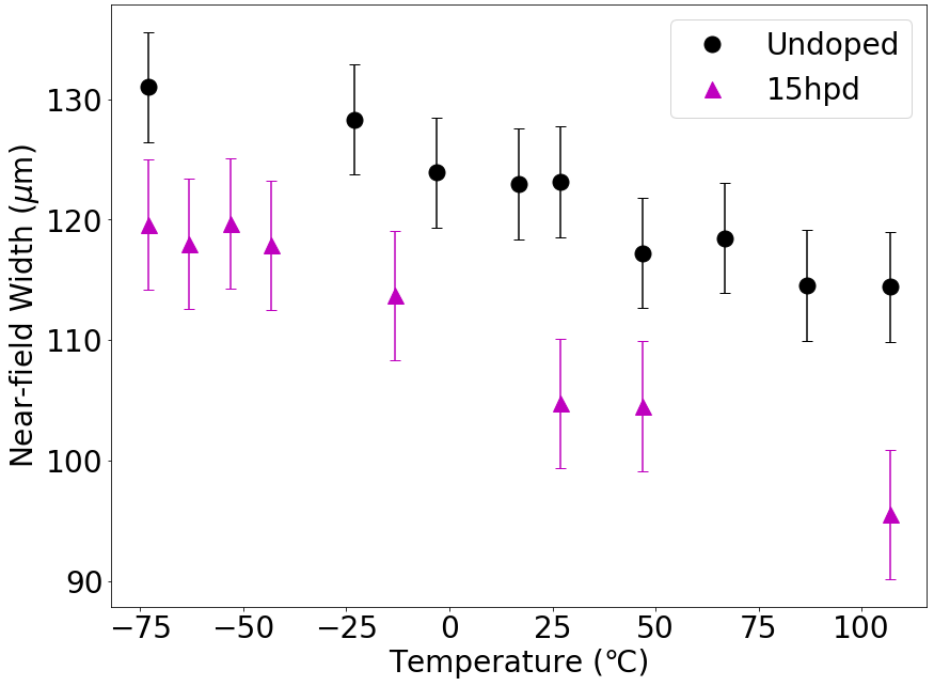

Figure 4.2: Near-field width as a function of temperature for a device with cavity length, 2000μm and a p-type modulation doping density of 15hpd at 0.9xi_{th}.

5.1)μm.

The nearfield width narrowed with increasing doping, and this narrowing effect was independent of cavity length. The gradient of the change in nearfield width with temperature is (-0.10 $\pm$ 0.08)μm/K for the undoped device is (-0.14 $\pm$ 0.09)μm/K for the device with 15hpd.

The process of estimating the error came from the combination of the experimental error and the variation between nominally identical devices. The experimental error was found by re-measuring the same device and was 3.1μm. The error from device variation was the larger source of error and varied from wafer to wafer. There was no correlation with doping density, and the range was 7.3μm-10.7μm.

The narrowing of the nearfield could be due to the increasing mobility of the charge carriers, allowing them to become increasingly optimally distributed, narrowing the nearfield. However, as evidenced in section 4.2.3, the undoped device is thermally distributed across the full temperature range. It could also arise as a result of a greater degree of gain guiding from an increase in the charge carrier density, or as a result of changes to the α_H alpha (Henry) parameter. Another potential explanation for the narrowing could be due

to a decrease in the carrier lifetime, which would result in decreases in the mobility and carrier diffusion and hence the current spreading. One study that examined the carrier lifetimes in InAs/GaAs lasers found that doping with 10hpd reduced the carrier lifetime from 1200 to 700ps retaliative to an identical undoped device [11].

The temperature dependant narrowing of this is shown for the 15hpd in figure 4.3 for 200K, 260K, 320K and 380K. A reduced number of measurements is plotted to aid comprehension. The small peak to the left is most likely a result of uneven application of the top contact due to ongoing modification to the fabrication process to increase speed of device fabrication. The majority of devices fabricated exhibited this issue to a greater or lesser degree. The devices with the lowest threshold, providing they had a good nearfield were selected for this study. A device was excluded on the bases of nearfield if a dip or a spike in the contact stripe region of the nearfield profile was greater than 10 pixels. An example of an appropriate and inappropriate nearfield are shown in figure 3.3.

The FWHM of the nearfield is given by the width of the profile that is half of the maximum intensity value. The nearfield intensity is normalised by dividing the intensity values by the peak intensity value.

4.2.3 Threshold Current Density as a Function Of Temperature

The threshold current density as a function of temperature shows a pattern, which we explain by considering a model of charge carrier distribution with two regimes, random/non-thermal and thermal. The charge carrier distribution model is explained in further detail in 2.6.3 Charge Carrier Distribution Model. The case for the charge carrier distribution model is supported with further evidence from how the spectral width varies with temperature.

Non-thermal regimes are considered beneficial for applications such as mode-locking as they broaden the lasing emission spectrum, enabling shorter pulse duration [12] and could also lead to reductions in degradation since thermalisation is achieved by a significant population of the quantum well or wetting layer states. These non-thermal distributions are commonly found at low temperatures [13], up to 200K [14], in undoped devices. Here, we discuss devices with p-type doping that show evidence of non-thermal populations at temperatures well above 300K. The increasingly thermally distributed carriers result in a

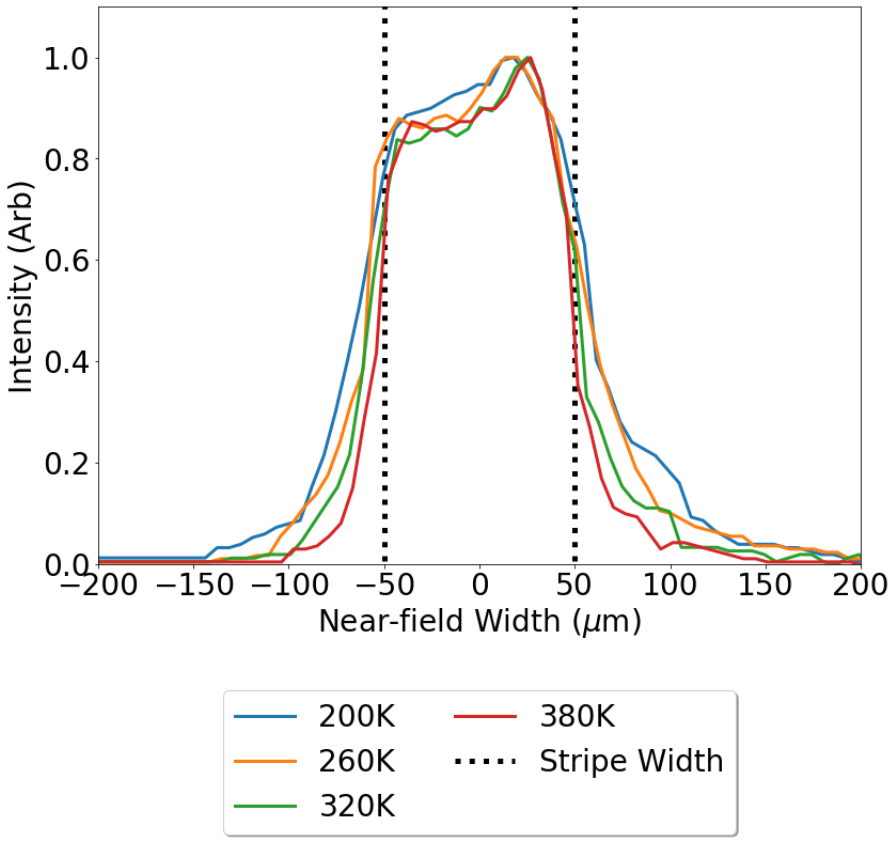

Figure 4.3: Temperature dependant nearfield plot for a device with a dopant density of 15hpd and a 2000μm cavity at 0.9xi_{th} at 200K , 260K, 320K and 380K. The location of the top stripe contact in relation to the nearfield is marked 'stripe width'.

local minima in threshold current density [14], prior to this the distribution is at least partly non-thermal. This minima occurs at higher temperatures for higher doping and longer cavities, so non-thermal operation becomes possible at room temperature.

The threshold current density was measured for devices of 1000μm, 2000μm and 3000μm and is shown in figures 4.4, 4.5 and 4.6.

For devices with 5 and 10hpd in the active region, the minima occur at 27 °C for 5hpd and 57 °C for 10hpd in the 1000μm device showing in 4.4, at 47 °C for 5hpd and 67 °C for 10hpd in the 2000μm device 4.5 and 37 °C for 5hpd and 77 °C for 10hpd in the 3000μm device 4.6. These results are in keeping with the charge carrier model outlined previously in section 2.6.3.

Higher levels of p-type modulation doping cause excited electron energy states to be relatively depopulated

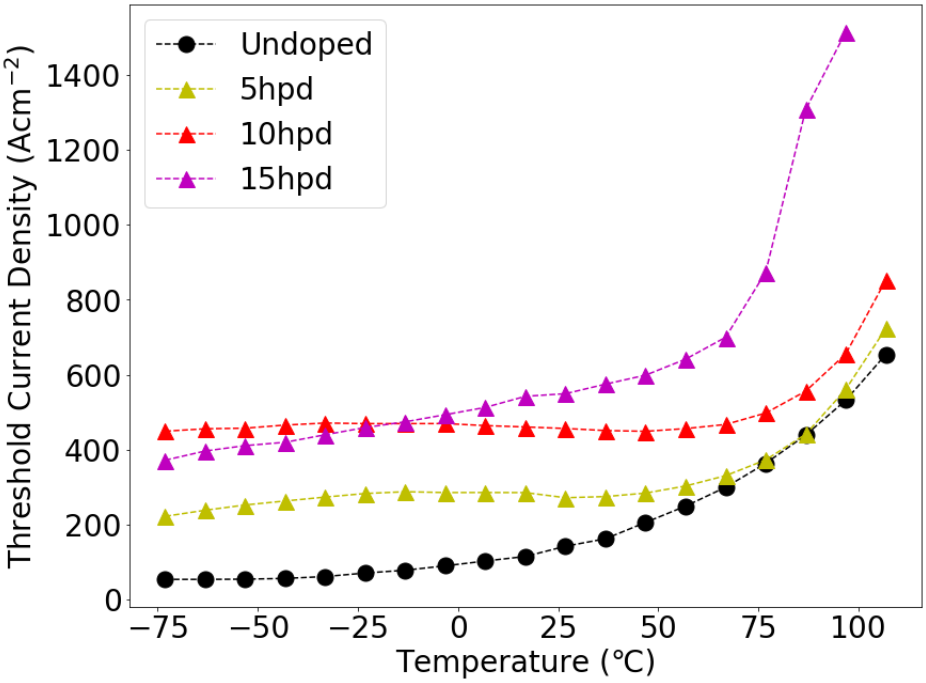

Figure 4.4: Threshold current density as a function of temperature between −75 °C - 125 °C, with 0, 5, 10 and 15hpd at the active region for devices with a cavity length of 1000μm.

as the quasi-Fermi levels are shifted towards the valence states, accommodating more charge carriers before thermalization takes place. Longer cavities require lower threshold current densities to lase, the reduction in current extends the non-thermal regime to higher temperatures. These benefits increase with 5 to 10hpd. Devices doped with the higher doping density of 15hpd did not show such a clear minima as the additional doping increased the non-radiative recombination by a greater factor than the reduction from moving to a thermal distribution, masking the effect of the charge carrier distribution. This resulted in the beneficial outcome extended regions of temperature invariant threshold between −17 °C - 67 °C for devices with cavity lengths of 2000μm and above.

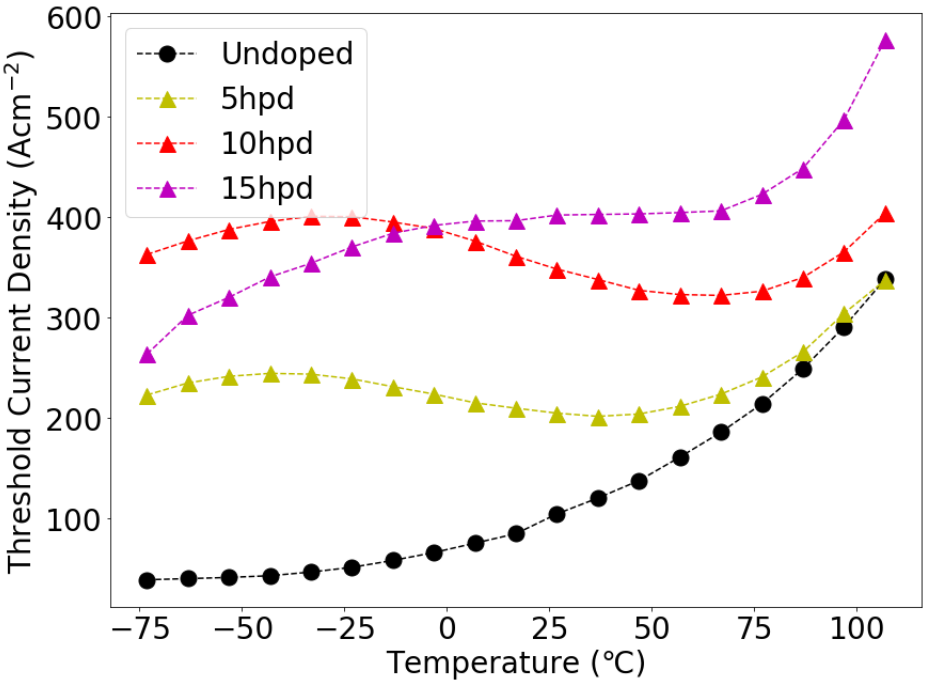

Figure 4.5: Threshold current density as a function of temperature between −75 °C - 125 °C, with 0, 5, 10 and 15hpd at the active region for devices with a cavity length of 2000μm.

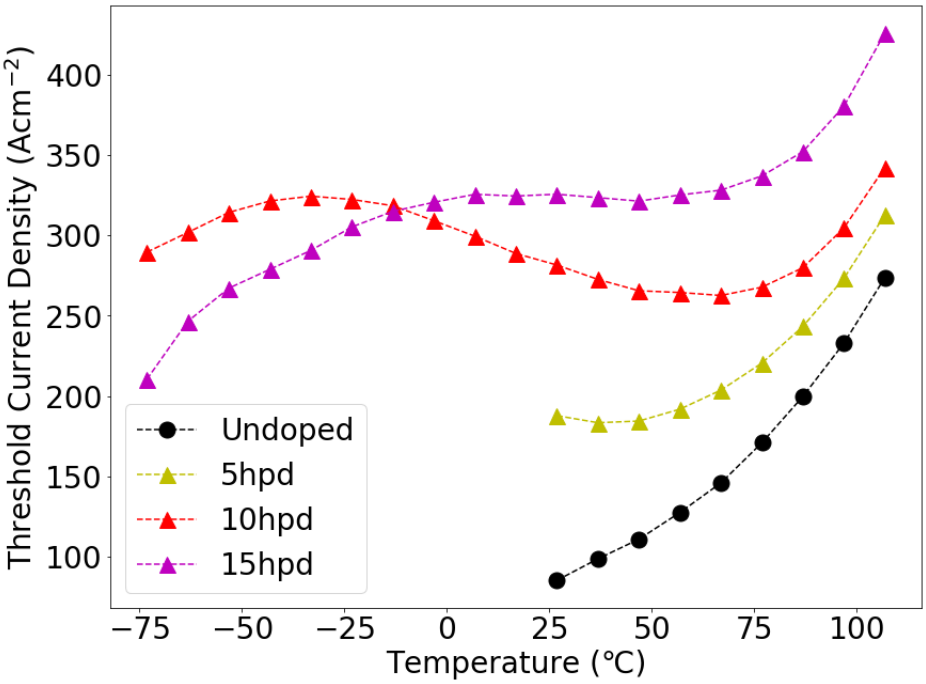

Figure 4.6: Threshold current density as a function of temperature between −75 °C - 125 °C, with 0, 5, 10 and 15hpd at the active region for devices with a cavity length of 3000μm. Temperatures below 25 °C were not recorded for the undoped and 5hpd device due to time constraints.

4.2.4 Wavelength

The wavelength was measured as a function of temperature between to assess the impact of doping on performance. All devices measured lased on the ground state across the full temperature range for the devices with 1000 - 3000μm.

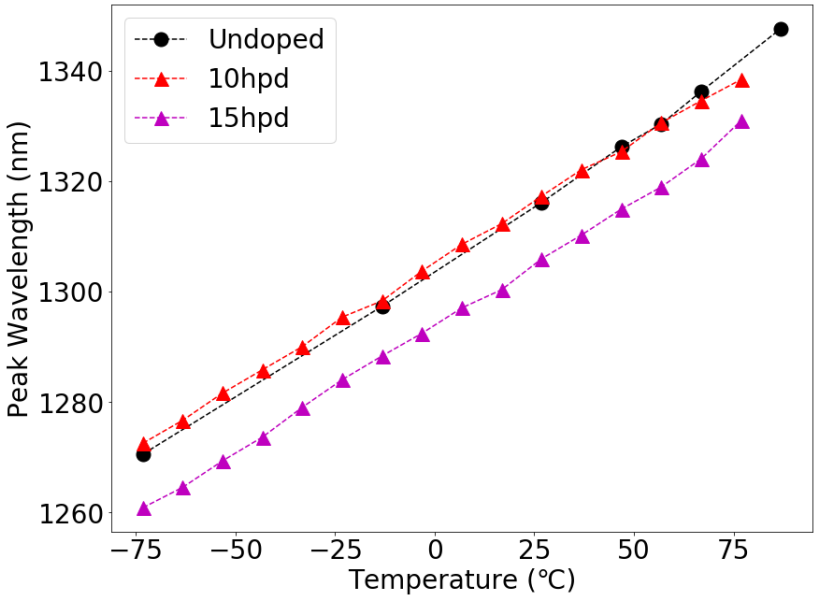

Figure 4.7: Peak wavelength as a function of temperature between −75 °C - 125 °C, with 0, 10 and 15hpd at the active region for devices with a cavity length of 1000μm at 1.1xi_{th}.

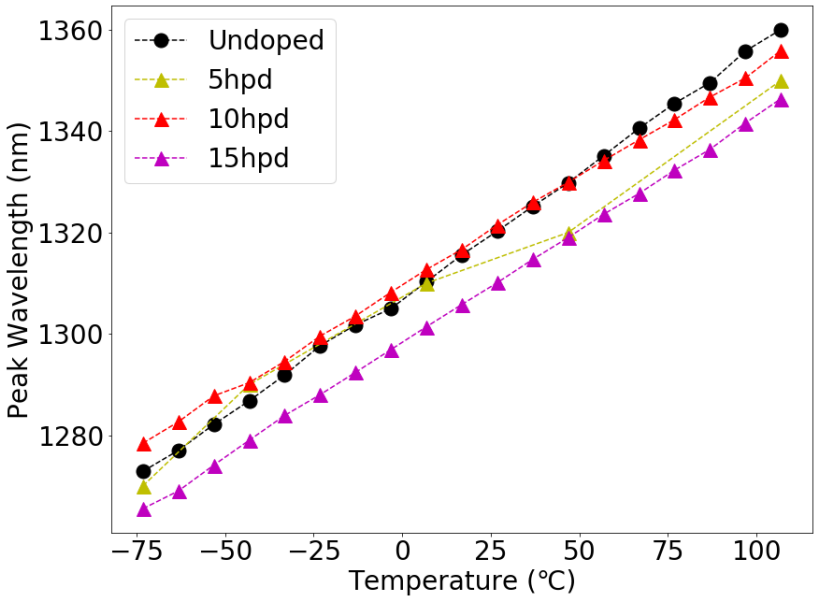

Figure 4.8: Peak wavelength as a function of temperature between −75 °C - 125 °C, with 0, 5, 10 and 15hpd at the active region for devices with a cavity length of 2000μm at 1.1xi_{th}.

5 and 10hpd had negligible impact on the peak lasing wavelength. There was a blue shift in the 15hpd p-type modulation doping, which could be due to higher optical loss due to too high a level of p-doping.

4.2.5 Results as a Function of Doping

It is complex to state the impact of doping on device performance, as the cavity length and measurement temperature both have significant effects. The combination of doping, cavity length and temperature have many permutations. Like many studies, p-type modulation doping did not improve threshold current density, as summarized for 1000μm laser devices in figure 4.9.

P-type modulation doping did increase the temperature at which non-thermal carrier distributions can be found. This is summed up in table 4.1, which gives the temperature of beginning of full thermalization for 5hpd and 10hpd laser devices. The benefits of non-thermal carrier distributions are discussed in section 4.2.3. The point at this occurred for the undoped lasers was less than the minimum temperature used, $-73\,^{\circ}$C. For devices with 15hpd, a potential increase in non-radiative recombination counters the negative temperature dependence of threshold current seen for 5hpd and 10hpd, making the value unobtainable with current data alone. However, this did result in large region performance that was insensitive to temperature between $-17\,^{\circ}$C and $67\,^{\circ}$C for devices with cavity lengths of 2000μm and above. Temperature insensitive outputs can be desirable, however this came at the cost of a bigger increase in threshold current density.

	1000μm	2000μm	3000μm
5hpd	$27\,^{\circ}$C	$37\,^{\circ}$C	$47\,^{\circ}$C
10hpd	$47\,^{\circ}$C	$57\,^{\circ}$C	$56\,^{\circ}$C

Table 4.1: Summary of temperature of beginning of full thermalization for 5hpd and 10hpd laser devices with cavities 1000μm, 2000μm and 3000μm long.

The threshold current density results as a function of doping are presented for devices of cavity length 1000μm in figure 4.9 1000μm is selected as the shorter cavity lengths are more desirable for integration due to their reduced footprint and increased switching speeds. It is shown at $27\,^{\circ}$C and $97\,^{\circ}$C as room

temperature operation and high temperature performance are two of the greater areas of interest.

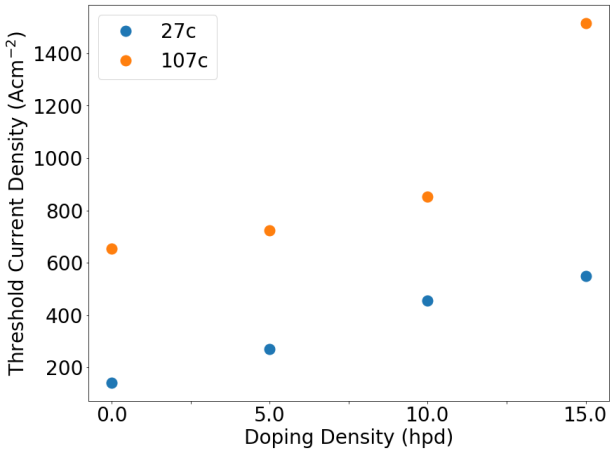

Figure 4.9: Threshold current density as a function of doping level for 27 °C and 97 °C for devices of cavity length 1000μm.

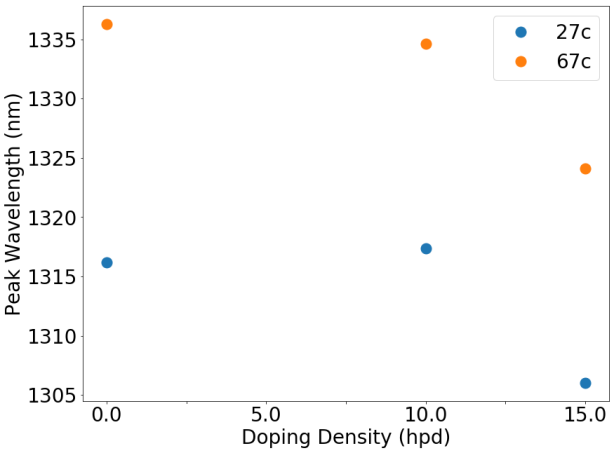

Figure 4.10: Peak wavelength at 1.1xi_{th} as a function of doping level for devices of cavity length 1000μm.

In figure 4.10 the peak wavelength as a function of doping is shown. 67 °C is used as the higher temperature, as it is the maximum temperature recorded for some devices due to time constraints. The data for 5hpd was also not taken due to time constraints. Whilst the wavelength increases with temperature, it shows the devices remain lasing from the ground state across the full temperature range. For most applications, ground state lasing is desirable as it is more efficient and requires a lower detection bandwidth availability.

4.2.6 Spectral Width

To further test the charge carrier model outlined in section 2.6.3, the spectral width as a function of temperature is examined. The spectral width reflects the distribution in carrier density, and the spectral width as a function of temperature would follow the form of the threshold current density as a function of temperature if the charge carrier mechanism is the dominate factor in the temperature dependence.

Whereas, the spectral width as a function of temperature would be independent of threshold current density as a function of temperature if a temperature dependent non-radiative process was causing the effect.

Light from the devices was focused onto a fibre connected to a spectrum analyser. Spectral data was gathered across the temperature range, and the spectra was fitted with a Gaussian to determine the FWHM of the emissions. Here, the spectral width is calculated as the full width half maximum of the spectrum. The results from one device, displayed in figure 4.11, are in perfect agreement with this model. However, other devices showed a more random distribution.

Close examination of the data pertaining to measured devices highlighted that the device shown in figure 4.11 had a nearfield that exhibited less filamentation than most other devices. Filamentation is the tendency for light to self-focus in regions of the device, creating uneven nearfield profiles. Furthermore, it was noted that not all the light was able to be focused onto the fibre meaning that different regions of the laser were examined at different fibre positions. This was investigated further using the monochromator to measure the spectra as light enters the equipment through a narrow slit that captures more of the beam than the fibre for the spectrum analyser.

This method found the spectral width to be in agreement with the threshold for a second 1000μm device doped with 10hpd, shown in figure 4.12.

Beyond the minimum point, indicated by the purple arrow in figure 4.11 top and at 57 °C in 4.12, thermal effects dominate, in the mechanism outlined in section 2.6.3. However, other additional thermally dependent effects may begin to act, which can have an opposing effect and reduce the spectral width. These could include an increase in the homogeneous broadening of the gain with increasing temperature

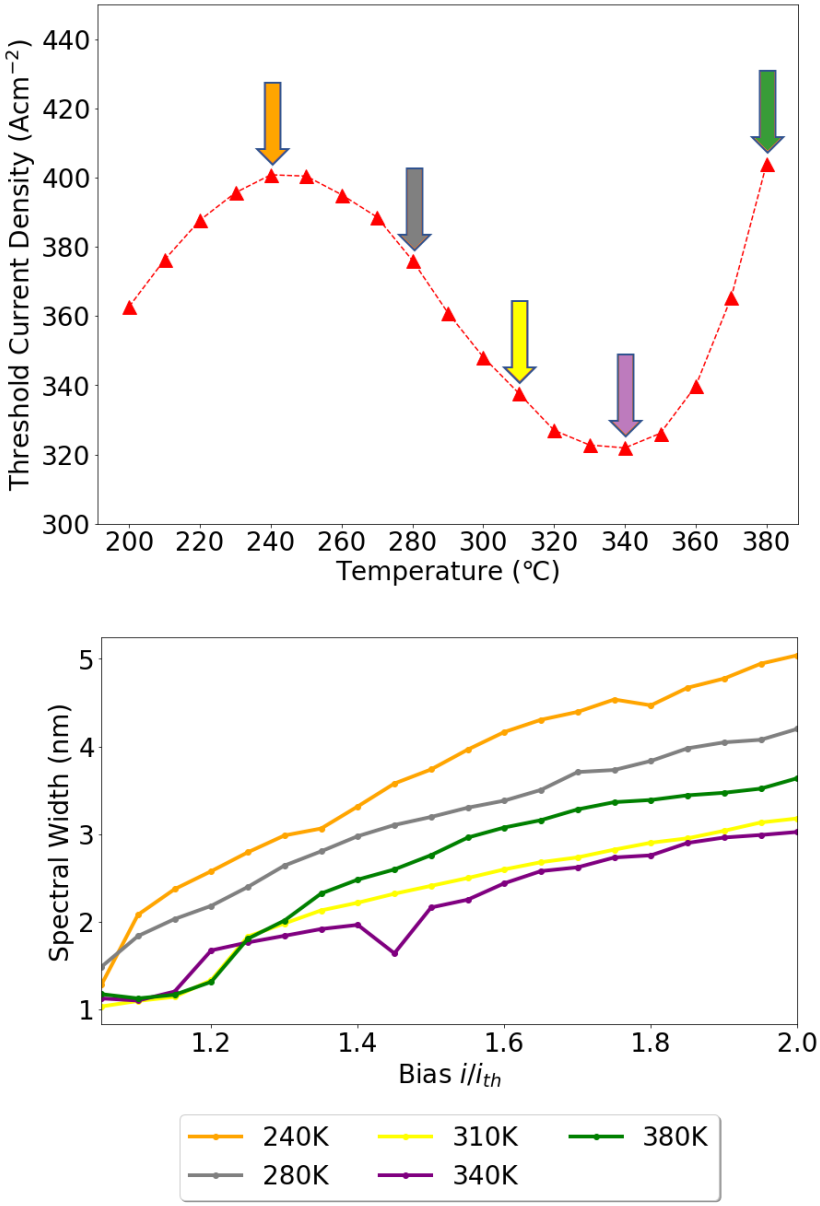

Figure 4.11: Upper: threshold current density as a function of temperature, lower: Spectral width as a function of i/i_{th} for temperatures 240K (orange), 280K (grey), 320K (yellow), 340K (purple) and 380k (green). These temperatures on the threshold current density plot are indicated by arrows of the corresponding colours. The measured device was of cavity length, 2000μm and a p-type modulation doping density of 10hpd.

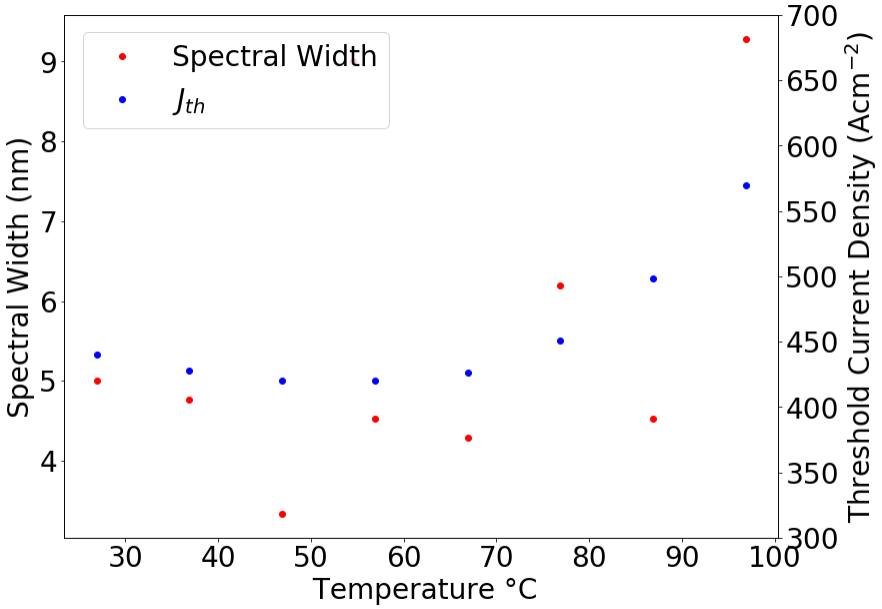

Figure 4.12: Spectral width as a function of temperature at 1.1xi_{th} (red, left axis) and threshold current density as a function of temperature (blue, right axis) for a device with 10hpd p-type modulation doping and a cavity length of 1000μm.

[15] as the broadening means that the range of dots that contribute to the gain peak lasing increases, reducing the lasing linewidth. In addition, a decrease in population inversion over the entire gain spectrum due to thermal coupling to the wetting layer, could contribute to reducing the number of modes that reach threshold, also narrowing the lasing spectrum [16] [17]. Therefore, it may not be correct to conclude correspondence between spectral width and threshold current density at temperatures beyond the thermal minima supports the charge carrier model.

4.2.7 Doping Density Selection

In the devices measured, p-type modulation doping did not provide a reduction in threshold current density. Although this could be the case for shorter devices or at higher temperatures than are measured in this study. 10hpd provided the greatest benefit in terms of clearly increasing the temperatures where non-thermal charge carrier distributions were present. It did not alter the peak wavelength compared to the undoped device. For these reasons, this doping density was selected for further investigation.

4.3 Investigation of Modulation Doping Layer Position

Following from the investigation of the doping in section 4.2 a second set of wafers was grown to experimentally examine the position and thickness of the p-type modulation doping layer with an aim to improve performance. Four different doping designs were grown along with an undoped reference wafer on the basis of computational modelling, two investigating the position and two investigating the thickness. Lasing performance of devices fabricated from wafers grown to the four designs and an undoped reference sample were characterized to compare performance to establish the best design for the investigated wafer structure.

4.3.1 Structures

The wafers used to fabricated the structures examined were grown by colleagues at UCL on 3-inch Si-doped GaAs wafers by MBE. The structure of the wafer is nominally identical to the structures described in section 4.2.1 with the exception of the thickness of lower GaAs confinement layer being increased from 37.5nm to 42.5nm and the doping layer within the GaAs barrier layer in the active region. The dot density was increased from the previous growth series and was found to be 5x10^{-10}cm^{-2} as measured by AFM and the resultant doping density in each doped wafer was 10hpd.

Four designs with varying dopant position and layer thickness within the 42.5nm undoped GaAs barrier layer, and a nominally identical undoped reference design were investigated. Design A and B both had a 10nm thickness p-type modulation doping layer, that was located 15nm and 7nm above the quantum well. Design A is identical to the doping layer used in section 4.2. Design C and D both had a 6nm thickness p-type modulation doping layer, that was located 19nm and 8nm above the quantum well. The spacing above the quantum well was similar for designs A and C and for B and D to investigate the impact by varying one parameter at a time.

Designs were fabricated using the same method as outlined in section 4.2.1. 4 lasers of 3000μm, 2000μm, 1000μm, 500μm, 400μm and 300μm were fabricated. All devices were measured at room temperature, and temperature dependant measurements of the two best performing were taken to ensure the result is reproachable. The best performing device is presented. The fabrication was carried out by Dr. Zhibo Li

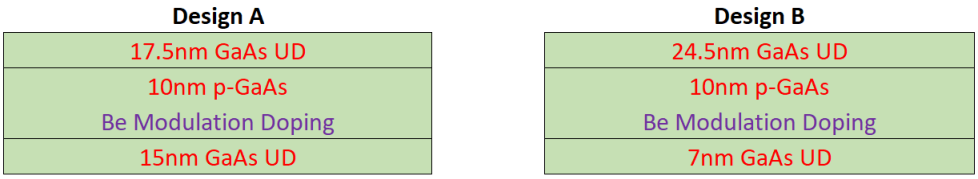

Figure 4.13: Schematic diagram showing designs A and B with 10nm thickness p-type modulation doping layer at different locations within the GaAs spacer layer.

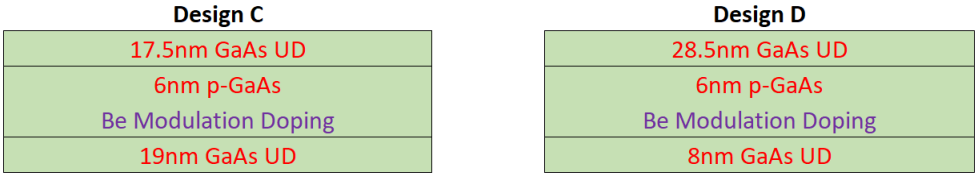

Figure 4.14: Schematic diagram showing designs C and D with 10nm thickness p-type modulation doping layer at different locations within the GaAs spacer layer.

and the wire bonding by Dr. Richard Forest and Josie Nabialek.

4.3.2 Room Temperature Performance

The threshold current density at room temperature (27 °C) was measured for devices with a range of cavity lengths from 3000 - 300μm, by Josie Nabialek. The results plotted against inverse cavity length are shown in figure 4.15. The undoped laser has the lowest threshold current density for device lengths where the device is lasing on the ground state.

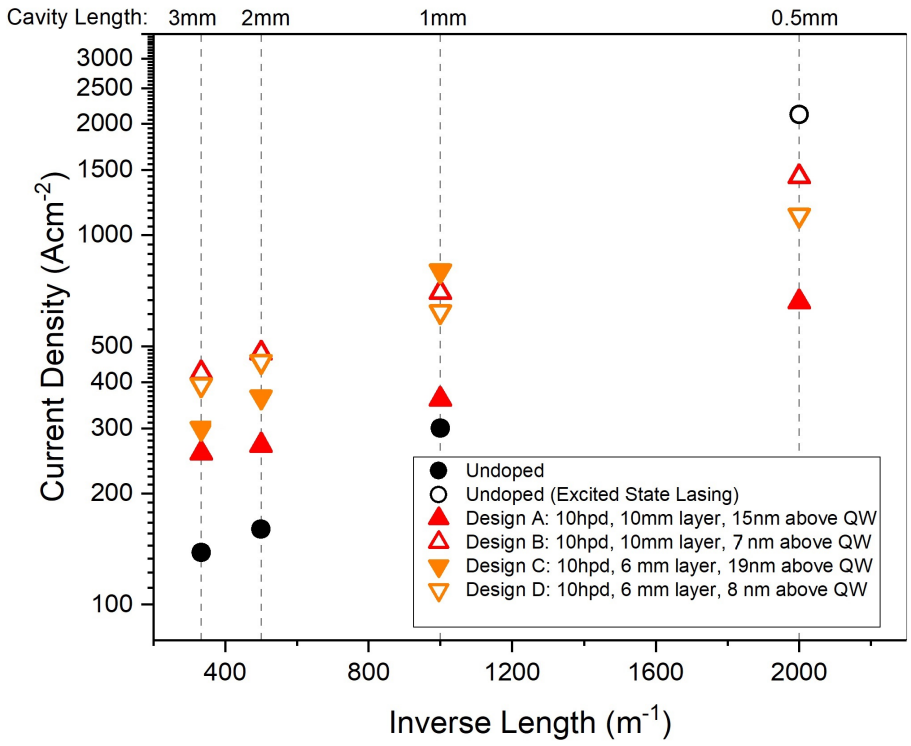

Figure 4.15: Threshold current density (logarithmic scale) as a function of inverse cavity lengths for the five different wafer designs measured by Josie Nabialek, data analysis by Dr. Craig Alford.

At 27 °C, design B has the highest threshold of the devices operating with ground state lasing, with the exception of design C for 1000μm cavity. As this device is operating close to the point where it switches to excited state lasing, this relative increase in threshold current density could be due to gain saturation.

The high threshold current density designs B and D both have doping layers that are 6nm above the quantum well layers. This may be too close, and result in a modification of the dot potential, decreasing

electron confinement and increasing hole confinement. Which could result in reduced probability of recombination by increasing the range of confined hole states, worsening the reduction in available ground state gain due to an increase in thermal carrier spread of holes from the additional confined states.

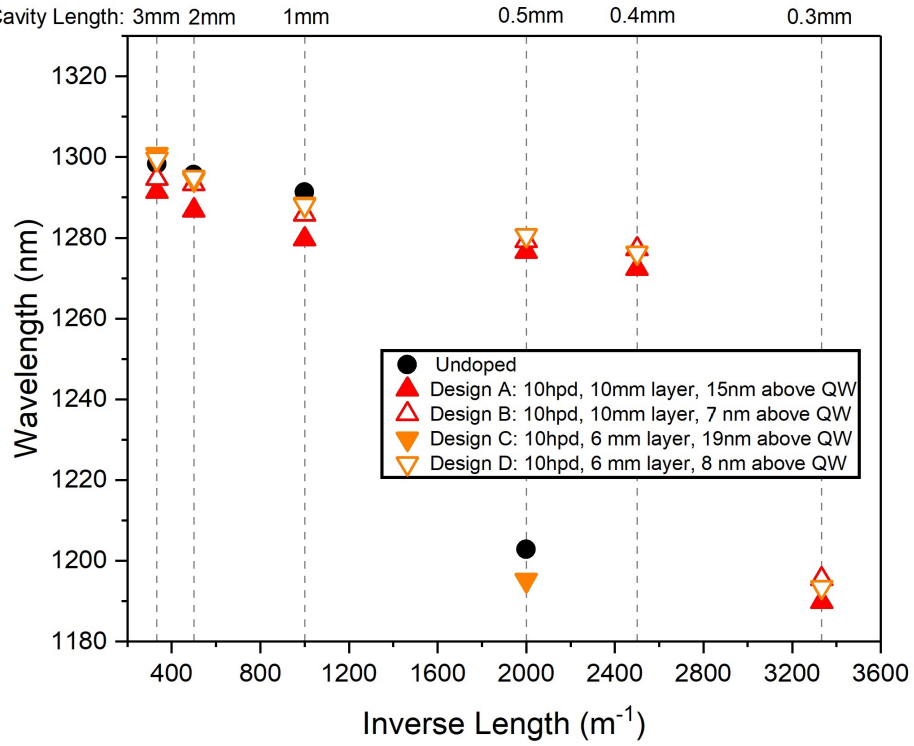

Figure 4.16: Peak lasing wavelength at 1.1xi_{th}, as a function of inverse cavity lengths for the five different wafer designs measured by Josie Nabialek, data analysis by Dr. Craig Alford.

Peak lasing wavelength is plotted as a function of inverse cavity length and is shown in figure 4.16. P-type modulation doping prevents transition to the excited state in designs A, B and D, where ground state lasing at 27 °C was achieved in devices with cavity lengths of 400μm, compared to 1000μm for design C and the undoped device.

Device C has the farthest distance between the doping layer and the quantum well layer. This may be too far a distance for sufficient holes to move to the active region and increase the available ground state gain, which could explain why this design switches to excited state lasing at a longer cavity length compared to the other three p-doped designs.

4.3.3 PIVT

The temperature dependence of the threshold current density is measured over the range −75 °C - 125 °C. For devices with cavity lengths of 1000μm, shown in figure 4.17 design A reduced the threshold current density relative to the undoped device above temperatures of 37 °C in 1000μm long lasers and above 77 °C in 2000μm long lasers shown in figure 4.18. Design B had a significantly higher threshold at room temperature, so was excluded.

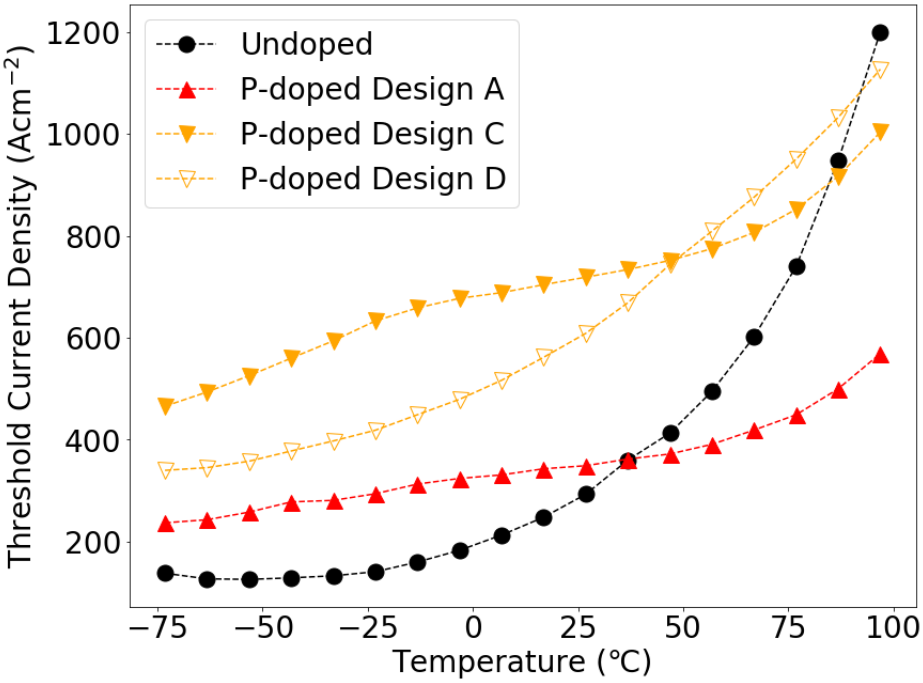

Figure 4.17: Threshold current density as a function of temperature between −75 °C - 125 °C for 1000μm long devices with 10hpd p-type modulation doping for designs A, C and D and an undoped device.

Doping designs A and C show a reduced temperature dependence however do not show a local minima, indicating that here increased non-radiative recombination is countering the reduction that would be seen from moving towards a thermal distribution. The threshold current density is greater in design C than design A. Which may be due to the greater distance to the quantum well layers from the doping layer. This distance is 15nm in design A and 19nm in design C.

Design D shows an exponential increase across the full temperature range, indicating that the 1000μm device is operating in the fully thermal regime at all points. This difference in designs A and C give further evidence that the closeness of the doping layer to the quantum well layer (8nm), may be altering the dot

potential.

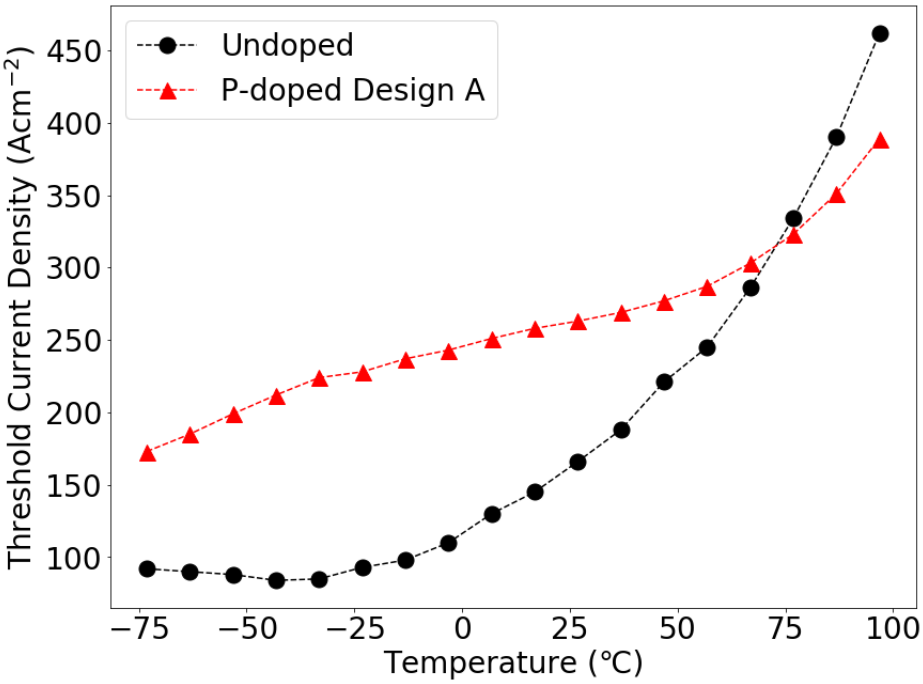

Figure 4.18: Threshold current density as a function of temperature between −75 °C - 125 °C for 2000μm long devices fabricated from design A with 10hpd p-type modulation doping and an undoped device.

Based on the notably lower threshold current density, design A is selected as the best dopant position and is used as the p-type modulation doped design.

4.3.4 Wavelength

Peak wavelength as a function of temperature was measured for the temperature range −75 °C - 125 °C, the results for design A and an undoped device of cavity length 1000μm is plotted in figure 4.19 alongside modelled results using the Varshni equation. The peak wavelength is very similar for both devices, with addition of p-type modulation resulting in a slight in a blue-shift as was seen for the higher doing density in section 4.2.4 which could be attributed to increased optical loss.

The temperature dependance of the wavelength was modelled using the Varshni equation [18]. The equation models temperature dependent energy gaps successfully for many semiconducting bulk and

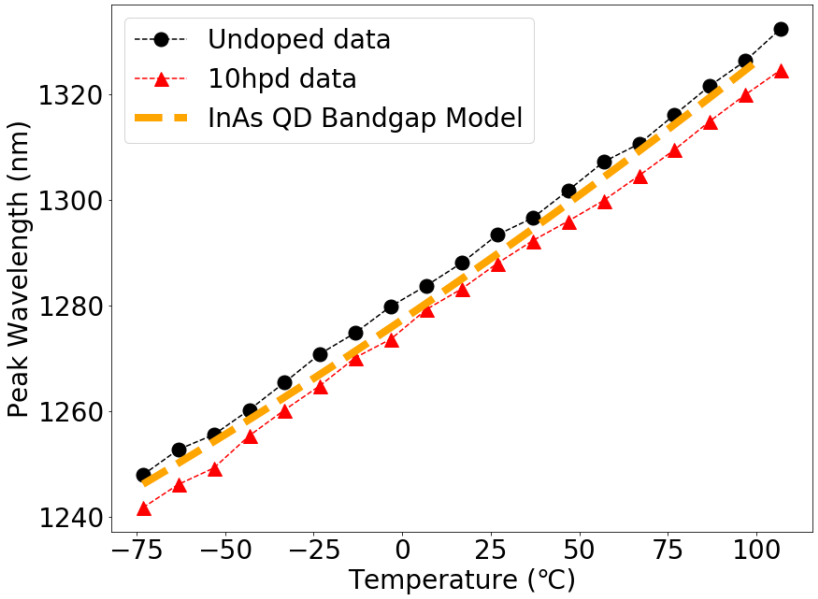

Figure 4.19: Peak wavelength as a function of temperature at 1.1xi_{th}, over the range −75 °C - 125 °C for lasers with a cavity length of 1000μm for a device with p-type modulation doping and an undoped device alongside modelled results using the Varshni equation.

nanostructures [19].

$$E_g(T) = E_g(0) - \frac{\alpha T^2}{T + \beta} \tag{1}$$

Where T is temperature in kelvin, E_g is the energy gap, $E_g(0)$ is the energy gap at 0K and α and β are experimentally derived contests that ensure the smoothness of the dependence. For the model, the values of α and β were reported in [20].

The gradient of the modelled InAs dot 0.462nm/K, for the undoped it is 0.463nm/K and for the doped 0.457nm/K. As the modelled dependence matches the results for the doped and undoped device, it can be said that the change in wavelength with temperature is due to the temperature dependence of the energy gap.

4.3.5 Nearfield Width

The nearfield width was reduced in devices with p-type modulation doping relative to the undoped device, and both the undoped and p-type modulation doped devices' nearfield widths narrowed with increasing temperature, as was observed in section 4.2.2.

At 27 °C, the average nearfield width for undoped devices was (109.7±4.9)μm and (98.4±5.2)μm for p-type modulation doped devices with 10hpd (design A).

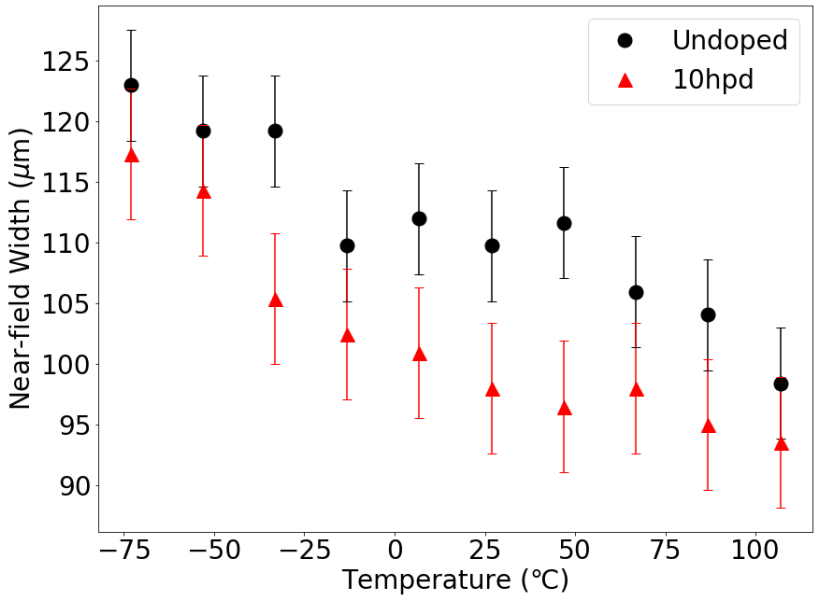

Figure 4.20: Nearfield width at 0.9xi_{th}, as a function of temperature over the range −75 °C - 125 °C for devices of 1000μm with no doping and p-type modulation doping with 10hpd (design A).

A discussion of the potential causes of the narrowing effect was given in section 4.2.2.

4.3.6 Absorption

Dot density was determined by AFM using dot layers grown on comparable uncapped samples, and did not find that p-type modulation doping affected the dot distribution. However, local variations in dot density and sampling issues can lead to a result that is not representative. To establish that the change in device performance is due to the doping and not as a result of changes to the dot distribution, the absorption spectra is measured using the segmented contact method outlined in chapter 3. The measurements were taken by Joe Mahoney.

The segmented contact devices were fabricated by Dr. Zhibo Li. The gold top contact was 100μm wide and the segments were 278μm. 14μm breaks were etched to a depth of 700nm to ensure the contacts were isolated electrically.

The absorption spectra of a semiconductor material is key to identifying the energy transitions present. Absorption spectra shows the energy transitions unlike other data such as Pl spectra, which are influenced by the charge carrier distribution within the material and interactions between charge carriers. [21]

Previous work from Cardiff showed that with the application of reverse bias to the unpumped sections during segmented contact measurements, no difference was present in the absorption spectra between a device with and a device without p-type modulation doping [22].

Without reverse bias, the absorption magnitude in the p-type modulation doped device was reduced. Here, the excesses of holes in the valence band blocks some of the potential absorption, referred to as carrier blocking.

However, other work reports that there is a reduction in the magnitude of the absorption, suggesting that p-type modulation doping effects the inter-diffusion of the dots and surrounding material, therefore account for the decrease in absorption [23].

Benjamin Maglio examined the effect of the p-type modulation doping on the absorption spectra of a device with p-type modulation doping, fabricated using wafer design A, and an undoped device shown in figure 4.21. The effect was examined by fitting the absorption spectra. As the dots had a bimodal distribution [24], as discussed in section 2.3, the ground and excited states were fitted with two Gaussians. It was found that the device with p-type doping had a greater level of broadening. The absorption coefficient was then calculated assuming constant inhomogeneous broadening in both samples, based on similarities observed by AFM measurements of uncapped samples [8].

The reduction in absorption magnitude was investigated comparing with a second calculation of the absorption coefficient without the occupational probabilities, by setting f_v - f_c to 1. This is because the p-type modulation doping shifts both electron and hole quasi-Fermi levels towards the valence band and there is an insufficient energy difference between the energy state and quasi-Fermi level to allow for

maximum absorption, resulting in carrier blocking [25].

The calculated absorption coefficients are the same for the undoped device but show a difference of 11cm^{-1} for the doped device, which is the reduction from state blocking. The remainder of the reduction in intensity was attributed to an increase in the homogeneous broadening term, which is related to carrier scattering [9].

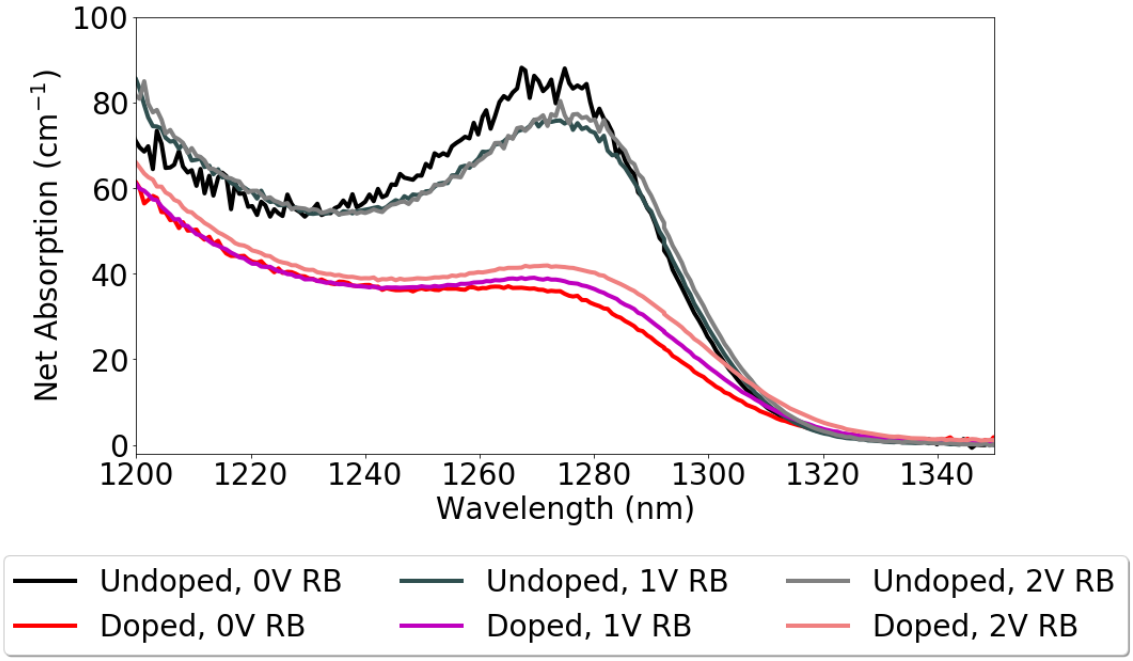

Figure 4.21: Reverse bias absorption spectra for a device with no doping and design A 10hpd p-type modulation doping, taken by Joe Mahoney.

State blocking is seen experimentally by the increase of the magnitude of the absorption spectrum with increasing reverse bias as excess holes are removed. However, in the case of the undoped device it lowers due to the increased electric field across the active region, reducing the electron and hole overlap [25].

4.4 Comparison with State of the Art

In this section, the performance of the devices is compared with state of the art devices from the literature. This is a complex process, as many of the figures of merit are influenced by factors other than the doping, such as device geometry [26] and number of layers in the active region [27]. Longer lasers will have lower threshold current densities, but shorter lasers are more desirable for integration purposes as they have

faster switching speeds. Some measurements are taken using pulsed operation to prevent self heating, and others are reported under continuous wave (cw) operation. Furthermore, the performance will be impacted by the quality and precision of the growth, which may not be consistent between studies.

A key parameter is the threshold current density, performance across a wide temperature range is desirable and particular focus is given to high temperature operation. The lowest threshold current density achieved by devices reported in this chapter was for a 1000μm p-doped laser fabricated from design A had a threshold current density of 263A/cm^2 at 27 °C and 389A/cm^2 at 97 °C. The device was a broad area device with 7 DWELL layers that was measured using pulsed operation.

The lowest reported threshold current density achieved by p-type modulation doping is 33A/cm^2 and 108A/cm^2 at room temperature and, 100 °C respectively [28]. This was achieved by an uncoated laser in pulsed operation with 7 DWELL layers and a 3000μm cavity.

A shorter 700μm long laser was reported with a threshold current density of 127A/cm^2 with both pulsed and CW operation at 300K [1]. This device had 3 DWELL layers.

The shortest length cavity that can obtain ground state lasing is a factor in improving the range of temperatures a device can operate over. Devices grown with p-type modulation doping have been shown to lase at the ground at shorter cavities than their undoped counterparts. Design A managed to achieve ground state lasing with pulsed operation in an uncoated 400μm cavity at 27 °C. 400μm ground state lasing was recently achieved under CW operation with an 8 DWELL laser [29] at room temperature. A 10 DWELL layer using pulsed operation achieved this for a 300μm cavity at room temperature [30]. Ground state lasing at 300μm has been achieved under CW conditions at room temperature by the additional use of highly reflective coatings on the facets [31]. The same design achieved CW ground state lasing at 400μm.

P-type modulation doping can also result in ranges of invariant threshold, in section 4.2.3 doping levels of 15hpd extended regions of temperature invariant threshold to between −17 °C and 67 °C for devices with cavity lengths of 2000μm and above. The highest reported range of temperature invariance is −70 °C and 25 °C in [32].

In the literature, devices with p-type modulation doping are grown with the doping layer in different positions and with different widths. This is the only work to date that examines the position and the width of the doping layer in nominally identical devices.

4.5 Chapter Summary

The level of p-type modulation doping was investigated by means of a joint computational and experimental study. For the wafer design examined, the best dopant density for high temperature performance in this study was found to be 10hpd, which resulted in non-thermal distributions at high temperatures and was evidenced by the temperature dependence of both threshold current density and the spectral width. Increased doping levels of 15hpd extended regions of temperature invariant threshold between $-17\,^{\circ}\mathrm{C}$ and $67\,^{\circ}\mathrm{C}$ for devices with cavity lengths of 2000μm and above, but substantially increased threshold current densities relative to lasers with a nominally identical structure without p-type doping. The nearfield width narrows with the addition of doping and increasing temperatures in both doped and undoped devices. This could be due to decreases in the carrier lifetime or changes in the α_H alpha (Henry) parameter.

The thickness and position of the doping layer was investigated, and the best performance was and found to be from devices with a 10nm layer, 15nm above the quantum well layer. Placement of the doping layer closer to the quantum well layer, a spacing of 8nm, increased the threshold current density by $103\mathrm{A/cm}^2$ at $-73\,^{\circ}\mathrm{C}$ and $604\mathrm{A/cm}^2$ at $106\,^{\circ}\mathrm{C}$. This structure achieved high gain, $30.95\mathrm{cm}_{-1}$ for a 400μm cavity laser and reduced threshold current density relative to the undoped device above temperatures of $37\,^{\circ}\mathrm{C}$ in 1000μm long lasers and above $77\,^{\circ}\mathrm{C}$ in 2000μm long lasers.

The absorption was measured by the segmented contact method and was found to be reduced for devices with p-type modulation doping.

References

[1] O. Shchekin and D. Deppe. "Low-threshold high-T0 1.3-μm InAs quantum-dot lasers due to p-type modulation doping of the active region". In: *IEEE Photonics Technology Letters* 14.9 (Sept. 2002).

[2] P. M. Smowton, I. C. Sandall, H. Y. Liu, and M. Hopkinson. "Gain in p-doped quantum dot lasers". In: *Journal of Applied Physics* 101.1 (Jan. 2007).

[3] S. Chen, W. Li, J. Wu, Q. Jiang, M. Tang, S. Shutts, S. N. Elliott, A. Sobiesierski, A. J. Seeds, I. Ross, P. M. Smowton, and H. Liu. "Electrically pumped continuous-wave III–V quantum dot lasers on silicon". In: *Nature Photonics* 10.5 (May 2016).

[4] J. C. Norman, Z. Zhang, D. Jung, C. Shang, M. Kennedy, M. Dumont, R. W. Herrick, A. C. Gossard, and J. E. Bowers. "The Importance of p-Doping for Quantum Dot Laser on Silicon Performance". In: *IEEE Journal of Quantum Electronics* 55.6 (Dec. 2019).

[5] Y. Cao, T. Yang, H. Ji, W. Ma, Q. Cao, and L. Chen. "Temperature Sensitivity Dependence on Cavity Length in p-Type Doped and Undoped 1.3-μ m InAs–GaAs Quantum-Dot Lasers". In: *IEEE Photonics Technology Letters* 20.22 (Nov. 2008).

[6] Z. Zhang, D. Jung, J. C. Norman, P. Patel, W. W. Chow, and J. E. Bowers. "Effects of modulation p doping in InAs quantum dot lasers on silicon". In: *Applied Physics Letters* 113.6 (Aug. 6, 2018).

[7] S. Birner, T. Zibold, T. Andlauer, T. Kubis, M. Sabathil, A. Trellakis, and P. Vogl. "nextnano: General Purpose 3-D Simulations". In: *IEEE Transactions on Electron Devices* 54.9 (Sept. 2007).

[8] B. Maglio, L. Jarvis, M. Tang, H. Liu, and P. M. Smowton. "Modeling the effects of p-modulation doping in InAs quantum dot devices". In: *2021 International Conference on Numerical Simulation of Optoelectronic Devices (NUSOD)*. Sept. 2021.

[9] B. Maglio, L. Jarvis, C. P. Allford, S.-J. Gillgrass, S. Shutts, M. Tang, H. Liu, and P. M. Smowton. "The limits to peak modal gain in p-modulation doped indium arsenide quantum dot laser diodes". In: *2021 IEEE Photonics Conference (IPC)*. Oct. 2021.

[10] H. R. Philipp and H. Ehrenreich. "Optical Properties of Semiconductors". In: *Physical Review* 129.4 (Feb. 15, 1963).

[11] E. Harbord, P. Spencer, E. Clarke, and R. Murray. "Radiative lifetimes in undoped and p-doped InAs/GaAs quantum dots". In: *Physical Review B* 80.19 (Nov. 13, 2009).

[12] P. Finch, P. Blood, P. M. Smowton, A. Sobiesierski, R. M. Gwilliam, and I. O'Driscoll. "Femtosecond pulse generation in passively mode locked InAs quantum dot lasers". In: *Applied Physics Letters* 103.13 (Sept. 23, 2013).

[13] M. Grundmann and D. Bimberg. "Theory of random population for quantum dots". In: *Physical Review B* 55.15 (Apr. 15, 1997).

[14] M. Hutchings, I. O'Driscoll, P. M. Smowton, and P. Blood. "Fermi-dirac and random carrier distributions in quantum dot lasers". In: *Applied Physics Letters* 104.3 (Jan. 20, 2014).

[15] A. Sakamoto and M. Sugawara. "Theoretical calculation of lasing spectra of quantum-dot lasers: effect of homogeneous broadening of optical gain". In: *IEEE Photonics Technology Letters* 12.2 (Feb. 2000).

[16] A. Patanè, A. Polimeni, M. Henini, L. Eaves, P. C. Main, and G. Hill. "Thermal effects in quantum dot lasers". In: *Journal of Applied Physics* 85.1 (Jan. 1999).

[17] H. Huang and D. Deppe. "Rate equation model for nonequilibrium operating conditions in a self-organized quantum-dot laser". In: *IEEE Journal of Quantum Electronics* 37.5 (May 2001).

[18] Y. P. Varshni. "Temperature dependence of the energy gap in semiconductors". In: *Physica* 34.1 (Jan. 1, 1967).

[19] C.-C. Li, M. Gong, X.-D. Chen, S. Li, B.-W. Zhao, Y. Dong, G.-C. Guo, and F.-W. Sun. "Temperature dependent energy gap shifts of single color center in diamond based on modified Varshni equation". In: *Diamond and Related Materials* 74 (Apr. 1, 2017).

[20] I. Yeo, J. Dong Song, and J. Lee. "Temperature-dependent energy band gap variation in self-organized InAs quantum dots". In: *Applied Physics Letters* 99.15 (Oct. 10, 2011).

[21] I. O'Driscoll, P. M. Smowton, and P. Blood. "Low-Temperature Nonthermal Population of InAs–GaAs Quantum Dots". In: *IEEE Journal of Quantum Electronics* 45.4 (Apr. 2009).

[22] I. C. Sandall, P. M. Smowton, C. L. Walker, T. Badcock, D. J. Mowbray, H. Y. Liu, and M. Hopkinson. "The effect of p doping in InAs quantum dot lasers". In: *Applied Physics Letters* 88.11 (Mar. 13, 2006).

[23] O. B. Shchekin, D. G. Deppe, and D. Lu. "Fermi-level effect on the interdiffusion of InAs and InGaAs quantum dots". In: *Applied Physics Letters* 78.20 (May 14, 2001).

[24] H. Kissel, U. Müller, C. Walther, W. T. Masselink, Y. I. Mazur, G. G. Tarasov, and M. P. Lisitsa. "Size distribution in self-assembled InAs quantum dots on GaAs (001) for intermediate InAs coverage". In: *Physical Review B* 62.11 (Sept. 15, 2000).

[25] J. Mahoney, M. Tang, H. Liu, and N. Abadía. "Measurement of the quantum-confined Stark effect in $InAs/In(Ga)As$ quantum dots with p-doped quantum dot barriers". In: *Optics Express* 30.11 (May 23, 2022). arXiv: `2205.09427[cond-mat,physics:physics]`.

[26] P. Blood. *Quantum Confined Laser Devices: Optical Gain and Recombination in Semiconductors.* Oxford University Press, 2015. 433 pp.

[27] S. Alaei, M. Seifouri, S. Olyaee, and G. Babaabbasi. "Effect of the Number of Quantum-Dot Layers on the Performance of the 1.3 μm InAs/GaAs VCSELs". In: *2021 29th Iranian Conference on Electrical Engineering (ICEE)*. May 2021.

[28] H. Y. Liu, S. L. Liew, T. Badcock, D. J. Mowbray, M. S. Skolnick, S. K. Ray, T. L. Choi, K. M. Groom, B. Stevens, F. Hasbullah, C. Y. Jin, M. Hopkinson, and R. A. Hogg. "p-doped 1.3μm InAsGaAs quantum-dot laser with a low threshold current density and high differential efficiency". In: *Applied Physics Letters* 89.7 (Aug. 14, 2006).

[29] Q. Li, X. Wang, Z. Zhang, H. Chen, Y. Huang, C. Hou, J. Wang, R. Zhang, J. Ning, J. Min, and C. Zheng. "Development of Modulation p-Doped 1310 nm InAs/GaAs Quantum Dot Laser Materials and Ultrashort Cavity Fabry–Perot and Distributed-Feedback Laser Diodes". In: *ACS Photonics* 5.3 (Mar. 21, 2018).

[30] M. V. Maximov, Y. M. Shernyakov, F. I. Zubov, A. E. Zhukov, N. Y. Gordeev, V. V. Korenev, A. V. Savelyev, and D. A. Livshits. "The influence of p-doping on two-state lasing in InAs/InGaAs quantum dot lasers". In: *Semiconductor Science and Technology* 28.10 (Aug. 2013).

[31] Y. Zhonghui, C. H. W. Tuo, and J. C. Z. Ziyang. "P-Modulation Doped 1.3mu m InAs/GaAs Quantum Dot Lasers". In: *Chinese Journal of Lasers* 48.16 (2021).

[32] R. R. Alexander, D. T. D. Childs, H. Agarwal, K. M. Groom, H.-Y. Liu, M. Hopkinson, R. A. Hogg, M. Ishida, T. Yamamoto, M. Sugawara, Y. Arakawa, T. J. Badcock, R. J. Royce, and D. J. Mowbray. "Systematic Study of the Effects of Modulation p-Doping on 1.3-$\mu\hbox m$ Quantum-Dot Lasers". In: *IEEE Journal of Quantum Electronics* 43.12 (Dec. 2007).

5 Direct N-Type Doping

5.1 Introduction

A second method of improving the gain in InAs QD lasers, direct n-type doping, is investigated. Direct n-type doping has recently been shown to improve the gain in InAs quantum dot lasers grown on GaAs substrates [1, 2]. Structures are grown to examine impact on device performance and were compared with devices with p-type modulation doping and without any deliberate active region doping.

As part of a separate PhD project, Benjamin Maglio used NextNano, a self-consistent Schrödinger-Poisson-Current continuity solver to simulate a range of structural configurations for devices [3, 4]. Simulations describing the dot confining potentials for a structure with an undoped active region, and for direct n-type doping (at a level of one dopant atom per dot) were prepared. N-doped structures showed changes to the depth of confining potential and energy level spacing that are commensurate with increased likelihood of an electron and hole being in a ground energy state in the same dot. Such changes could result in improved device performance through increased recombination efficiency.

To investigate the impact of both methods, three different wafers were grown: one with direct n-type doping, one with p-type modulation doping and an undoped wafer to provide a reference. To determine the best n-doping level, test structures were evaluated using photoluminescence (PL) measurements. This direct comparison of the different doping strategies was published in the Journal of Physics D [5].

The p-type modulation doping level was selected using the previously-determined most efficacious doping level, used in a comparable previous design, which was examined in detail in Chapter 4: Increasing Gain in p-type Modulation Doped InAs Quantum Dot Lasers. The wafers were fabricated into ridge lasers with a 1000μm, 1500μm and 2000μm lengths and 25μm and 50μm mesa widths. To compare their temperature dependant performance, measurements of the threshold current, near-field and lasing spectra were then performed over a temperature range of 17 °C - 97 °C. In this work, direct n-type doping was observed to significantly reduce the threshold current but, due to a reduced lasing spot size, only result in a reduction in threshold current density in low gain areas of operation. It was also shown to decrease the temperature at which ground state lasing switched to excited state lasing compared with an undoped device.

Optimisation of the level of n-type dopant was then investigated experimentally by the growth of a second set of wafers with differing levels of n-type dopant and an undoped reference wafer for comparison. The wafers were fabricated into ridge lasers with a range of cavity lengths. Measurements of the threshold current, near-field and lasing spectra were then performed over a temperature range of 17 °C - 97 °C. Here, the narrowing of the lasing spectrum is not observed and this is discussed. Higher levels of direct n-type dopant are demonstrated to reduce the threshold current density across the full temperature range compared to nominally undoped structures.

5.2 N-Doping Theory

Direct n-doping is considered to be a viable strategy to improve recombination efficiency in III-V devices. Both p-type modulation doping and direct n-doping strategies improve the chance of direct recombination of holes and electrons from i.e. the E_1 to H_1 transition, but the electrical changes to the dot system that lead to in this improvement are different.

Unbiased semiconductors exist in a state of charge neutrality. Otherwise, potential fields would be established and charges would move to counter it (the principle of reciprocity). Consequently, the trend in each infinitesimal volume element of a material must resolve to equilibrium, where they presumably remain in a neutral state. In the undoped case, within a single dot, charge neutrality may be attained rapidly due to the probable presence of both an electron and a hole. Due to differences in how the electron and hole states populate, (known as valence band asymmetry, discussed in 2.4) reduced radiative recombination is observed in undoped III-V materials. Holes in this situation possess a much wider range of accessible states due to more closely spaced energy states (i.e. a large density of states). This results in a wider range of states available (and hence to occupy) at low energies for holes than for electrons. This property arises from the larger valence effective mass of the dot and barrier material. Similarly, in thermal equilibrium, the electron, with its larger energy spacing, is more likely to be in the ground state due to a larger separation between it and the next highest energy state. The probability of the electron and hole being in different allowed states can be quite high, reducing the electron hole overlap and reducing the radiative efficiency and gain of the dot material. In addition to this, whilst overall charge neutrality may be established, this

can be maintained via electron and hole being in different dots, also reducing the radiative processes.

Quantum dot effective masses serve as an excellent description for charge carrier behaviour in combined bulk / quantum well material. However, quantum dots do not have effective masses. The material that dots are made from have electron and hole effective masses - this leads to the energy level separation when Schrodinger's equation is solved, and this difference in separation is partly responsible for the different movement of the quasi-Fermi levels (when using a quasi-equilibrium model). The other factor is the effective electron and hole mass of the wetting layer material, which does lead to an unequal density of states and provides an additional contribution to the unequal movement of electron and hole quasi-Fermi levels, reducing the available gain.

In direct n-type doping, ions formed by dopants in the active region directly modify the dot's electric potential. This can have the effect of favourably altering the energy separation and position of the allowed states. Dopants are applied as a flux during dot formation, and it is observed that dopants can be preferentially incorporated into the dots with a minimal impact on dot distribution [6]. Within resultant dots, the negative donor ionizes, and the consequent positive charge deepens the electron (conduction) potential well and reduces the depth of the hole (valence) potential well. This increases the confinement for electrons while reducing electron leakage, and decreasing the number of confined hole states, raising the probability that an electron and hole are in the same energy state and can recombine radiatively. The shift in the band structure is shown by modelling of the band structure, shown in figure 5.1. Direct n-type doping has been shown to have benefits in solar cell efficiency by increasing the open circuit voltage, that maximum amount of voltage that a solar cell [7] can provide due to the passivation of defect states [8]. Improvements to the threshold and slope efficiency of quantum dot lasers on native substrates [1, 2] have also been demonstrated.

In contrast, p-type modulation doping adds a thin layer of acceptors (hole donors) close to the DWELL layers at such a distance as to not impact the dot potential. These mobile holes then diffuse into the active region and increase the probability of an electron and hole being in corresponding states. The position of the doping is optimised to allow maximal diffusion of holes into the dot without altering the shape of the

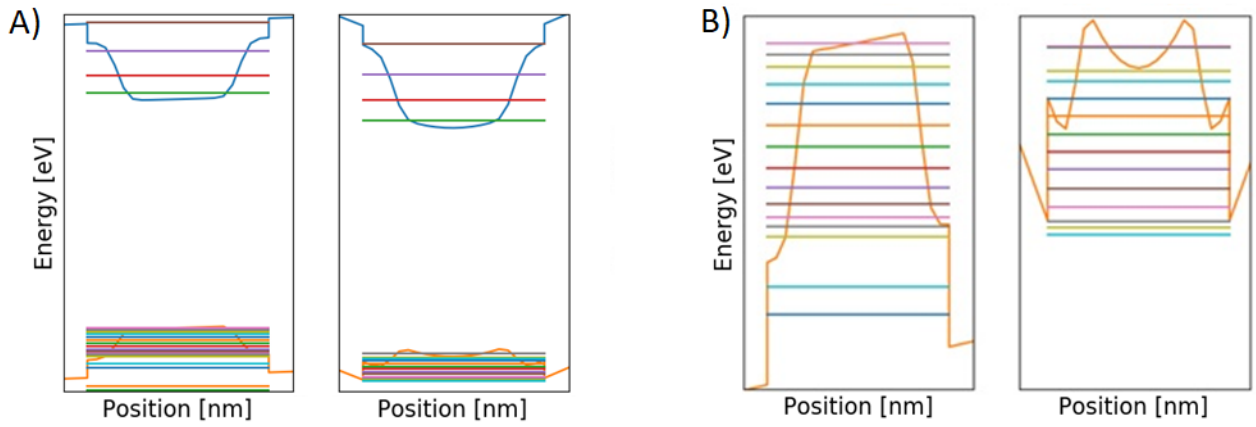

Figure 5.1: A) Calculated conduction and valence band structure left: undoped, right: direct n-type doping, and B) calculated valence band structure only left: undoped, right: direct n-type doping, produced by Benjamin Maglio using NextNano.

potential. However, the dopants can introduce deleterious effects, increasing optical loss and non-radiative recombination rates [9]. p-type modulation doping has been shown to increase the gain for a given quasi-Fermi level separation, and hence to reduce the temperature sensitivity of the threshold current [10, 11]. Further, increased temperatures at which ground state lasing occur [12] can be obtained. p-type modulation doping has shown promising results when grown on silicon, with increased operational lifetimes over that of undoped devices [13].

Figure 5.2 shows a schematic band diagram for both the undoped structure, direct n-type doping, p-type modulation doping to visually aid the different ways the two doping strategies achieve increased ground state hole population. A wafer schematic is provided in figure 5.3 showing the different locations within the semiconductor of the two doping types.

Initial studies into direct n-type doping showed apparent degradation of optical properties [14]. When a Si flux was applied during the growth, PL peaks were blue shifted, and displayed decreased intensity with increasing doping [15]. The direct n-type process was subsequently optimised by Inoue et al. in 2010 [6], examining the impact of when in the growth the Si flux is applied.

The dots investigated were formed via Stranski–Krastanov growth, which consists of four steps: nucleation, assembling, self-limiting, and dissolving. It was found that dopants applied during the assembling steps can be preferentially incorporated into the dots [6] compared to when the dopants were applied during other

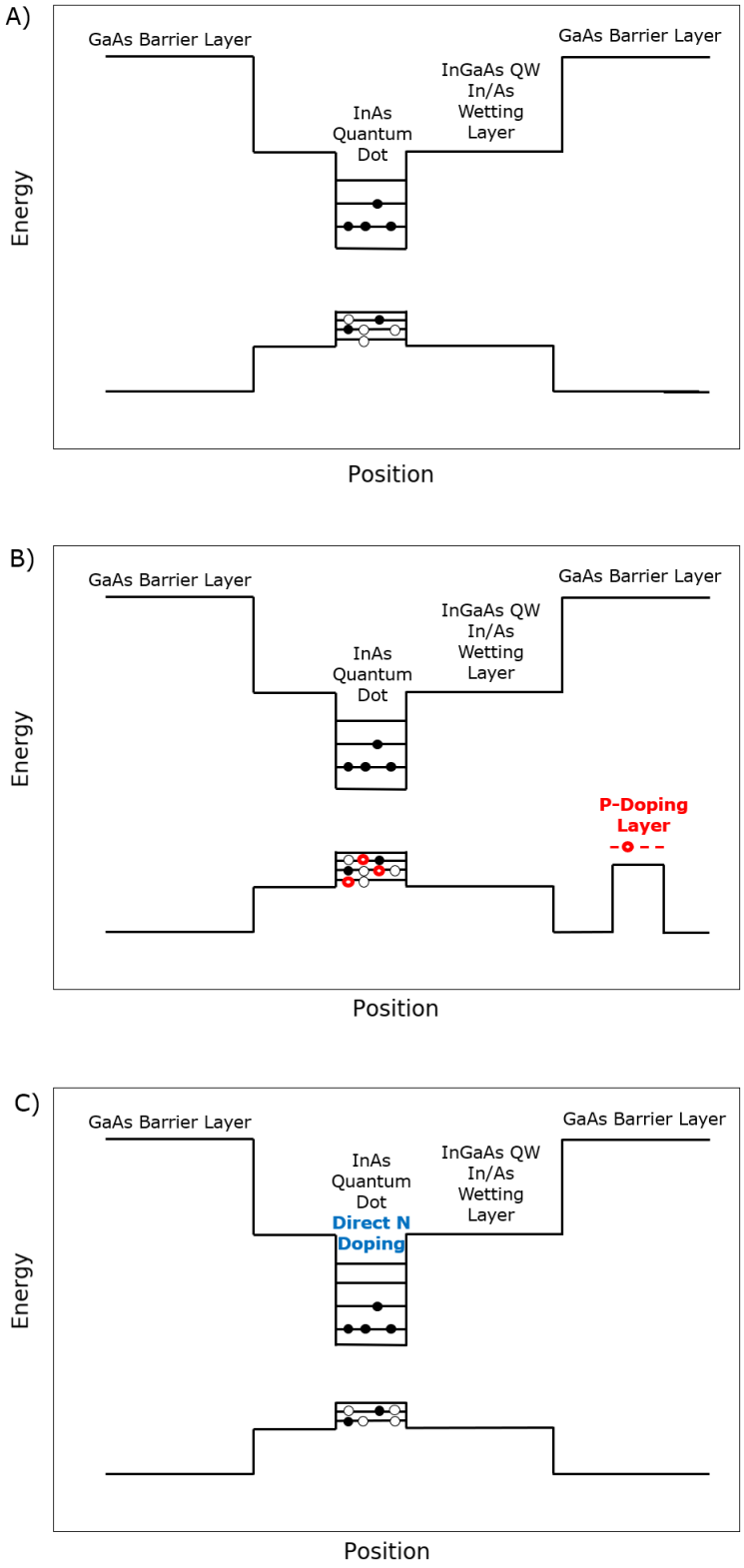

Figure 5.2: Schematic band diagrams for a single DWELL layer for the a) undoped structure, b) direct n-type doping and c) p-type modulation doping.

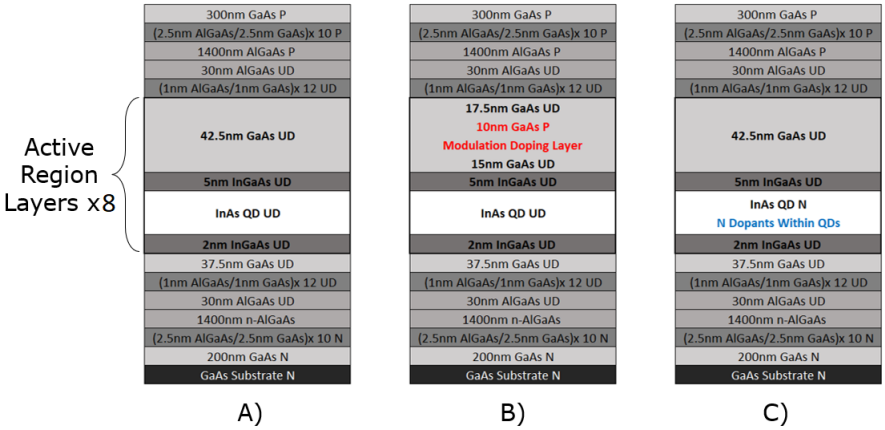

Figure 5.3: Wafer schematic diagram showing a) undoped, b) p-type modulation doped and c) direct n-type doped wafers.

stages. This optimisation was carried out by capturing high spatial resolution images of QDs at multiple growth stages using multiple forms of scanning probe microscopy: conductive and tapping atomic force microscopy (AFM). These methods utilize a scanning probe consisting of an extremely sharp probe tip mounted on a cantilever, which raster scans across the surface. Conductive AFM measures variation in a sample's conductivity at nanoscale resolution, by cantilever deflections detected with a photodiode. Tapping AFM is used to make morphology measurements. A cantilever is oscillated close to its resonance frequency, so it is in intermittent contact with the surface, reducing the pressure on the surface enabling the measurement of more delicate materials. This combination of techniques verified that the increase in conductivity measured using conductive scanning probe microscopy was congruent with the positions of the QDs identified by AFM.

The observed conductivity was notably higher in the n-doping applied at the assembly stage. N-doping can raise the quasi-Fermi levels, so the relative barrier height is reduced there, hence the increase in conductivity.

A further advantage of n-doping is that it is easier to control the number of dopants per dot. Whilst the dopant density and thickness can be accurately controlled to grow the p-type modulation doping layer, it is not certain that all dopants will ionise or that all carriers will move to the active region, leading to an uncertain number of effective dopants per dot. The lack of precision in dopants per dot is a drawback of

p-type modulation doping, one well observed in the literature [6] and leads to uncertainty when comparing modelled and experimental data. Comparatively, direct localization of the n-type dopants in the corresponding approach allow for comparative certainty in dopants per dot, and hence involvement in the active region.

5.3 Doping level Optimisation

To optimise the direct n-doping level, test structures were grown to investigate the optimal level of direct n-doping, by measuring their PL spectra and dot density using AFM. A description of PL measurements can be found in section 3.7. Wafers were grown by colleagues at UCL, who also performed the PL and AFM characterization. Four different wafers were grown on 3-inch Si-doped GaAs substrates by solid-source molecular beam epitaxy (MBE) with 0, 0.6, 1.2 and 2.4 donor electrons per dot. Silicon was used as the donor and was applied as a flux during the assembling step of the quantum dot growth. The structure used for testing is simpler than the final laser structure, with a simplified cladding layer and a final quantum dot layer grown on top to facilitate AFM measurements of the dot density. Full layer details given in a schematic diagram in figure 5.4. Adjacent DWELL layers were separated by a 4.5 nm low-temperature (510 °C) GaAs spacer layer and a 32.5 nm high-temperature (590 °C) GaAs spacer layer. The deliberate inclusion of high growth temperature spacer layers has been shown to reduce the number of threading dislocation defects, which would otherwise worsen optical and electrical characteristics [16].

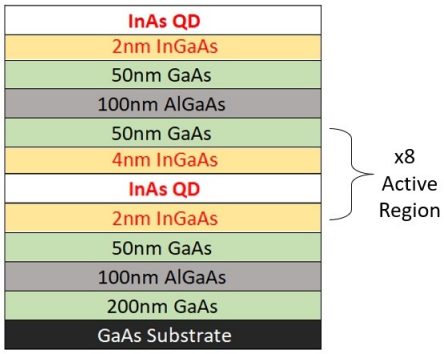

Figure 5.4: Schematic diagram of the wafer grown by UCL (not to scale), for the test structure to facilitate AFM And PL measurements.

AFM morphology measurements showed that doping level had a negligible effect on dot size and ratio of

the bi-modal distribution. The dot density was found to be $4.47 \times 10^{10}\,\mathrm{cm}^{-2}$, with a variation of $\pm 2.5\%$ that did not correlate with doping level.

The PL spectra is plotted in figure 5.5 and the results of the characterization performed at UCL is shown in table 5.1.

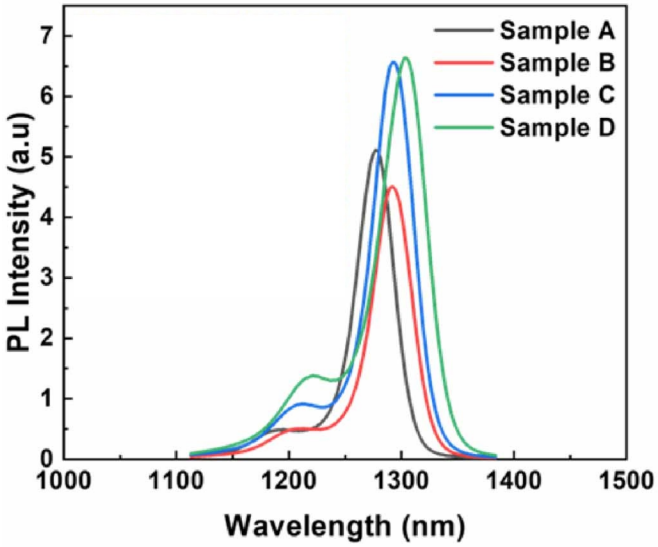

Figure 5.5: Room temperature PL spectra for test structures with 0, 0.6, 1.2 and 2.4epd, taken by Huiwen Deng at UCL.

Sample	**Doping density**	**QD density (10^{10} cm^{-2})**	**PL peak intensity (a.u.)**	**Peak wavelength (nm)**	**FWHM (meV)**
A	0	4.50	5.12	1277	29.76
B	0.6	4.33	4.54	1288	31.43
C	1.2	4.49	6.56	1292	31.97
D	2.4	4.57	6.66	1303	35.70

Table 5.1: Room Temperature PL Results for test structures doped with 0, 0.6, 1.2 and 2.4epd, taken by Huiwen Deng at UCL.

The peak red-shifts with increasing doping, the electron potential deepens, but the hole potential is more shallow, as seen in figure 5.1. The bandgap of the material itself doesn't change, but the separation of allowed energy states within this potential reduces and causes a lengthening of the emission wavelength. The PL peak broadens as in addition to the longer emitted wavelengths due to the mechanism outlined, there would also be some dots without dopant that would have the original transition energy, increasing the range of transition energies leading to a broader PL peak [5]. Alternatively, the broader PL peak may be due to increased homogeneity in the quantum dot size.

Ideally, n-doping would increase the PL peak intensity without broadening the PL spectra. The PL intensity is proportional to the number of transitions available and the probability of the transition. If the signal increases, it provides an indication that the doping may be beneficial, as increased available transitions would increase the gain. However, this measurement does not take into consideration potential increases in detrimental effects like non-radiative recombination, which would be present in a laser device. Test structures for PL measurements are quicker to grow and do not require fabrication steps, so provide a faster way of examining the effects of doping, but do not guarantee improvements within devices. A minimum of broadening of the PL spectrum allows states at the gain peak to be populated most efficiently, as the carriers spread over fewer states, resulting in better device performance. A doping density of 1.2 electrons per dot (epd) was selected, as it provided comparable PL intensity increase to 2.4epd without as significant PL spectral broadening (FWHM).

The p-type modulation doping level was optimised in a previous chapter for a comparable previous design and is found to be 10hpd for this structure, a full description of which can be found in Chapter 4. Here there are a 8, rather than 7, DWELL layers in the active region to try to increase gain in the p-type modulation doped lasers. There are also small changes to the barrier thickness and doping position and thickness, and a small change to the cladding layer thickness.

5.4 Structure Details and Laser Device Geometry

The structure was grown by researchers at UCL on 3-inch Si-doped GaAs wafers by solid-source molecular beam epitaxy (MBE) as shown in figure 5.6. First, a 200-nm GaAs n-doped buffer layer was grown, followed by a 10-repeat n-doped $Al_{0.4}Ga_{0.6}As$/GaAs layers of 2.5 nm thickness. A 1.4 μm $Al_{0.4}Ga_{0.6}As$ n-doped cladding layer was then grown, followed by a 30-nm undoped $Al_{0.4}Ga_{0.6}As$ guiding layer. Over this was grown 12-repeat 1nm thick $Al_{0.4}Ga_{0.6}As$/GaAs layers to form strained layer superlattices, the function of which is discussed in Chapter 3: Experimental Methodology. An additional 42.5nm buffer layer is grown, and then the 8 DWELL layers that form the active region are deposited. These layers are separated by a 42.5nm buffer layer where the p-type modulation doping layer is inserted. This structure, minus an additional buffer layer, is then repeated in reverse order above the active region, with the final

GaAs layer being 300nm, rather than 200nm and containing p, rather than n doping.

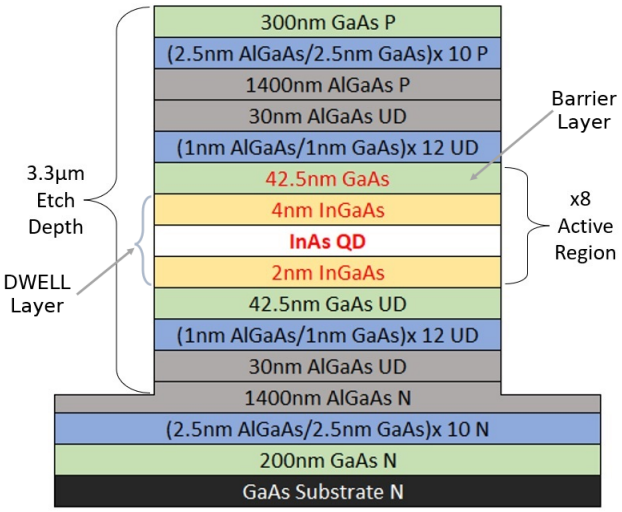

Figure 5.6: Schematic diagram of wafer structure for laser devices grown by UCL (not to scale).

5.4.1 Active Region Doping

The DWELL layers are formed by depositing 2.85 nm of InAs to self-organise into the dots over a 2 nm InGaAs layer and is capped with a 4 nm InGaAs layer. The two InGaAs layers around this, form a single QW in which the dots and wetting layer states sit. A GaAs spacer layer of 42.5 nm is grown on top of it, for the first repeat there is an initial spacer layer below the active region.

For the p-type modulation doping, a 10nm GaAs layer within the buffer layer is doped with beryllium atoms with a density of $4.5 \times 10^{17}\,\mathrm{cm}^{-3}$, leading to a dopant density of 10 holes per dot. The doped layer is grown 14.5nm above the quantum well. The beryllium dopants, show strong temperature dependence in growth - interstitial defects and enhanced dopant diffusion takes place at higher temperatures[17]. The lower 15nm undoped GaAs buffer layer is grown at a comparatively low temperature of 510 °C, then the 10nm p-type modulation doping layer is grown at 510 °C and then the 18nm undoped GaAs is grown at as a high temperature spacer layer at 590 °C.

In the n-doped case, a flux of silicon dopants were applied during the assembling process in QD formation to give a density of 1.2 electrons per dot.

5.4.2 Laser Fabrication

The wafer was then fabricated, by colleagues at UCL, into mesas of 50 µm and 25 µm width using photolithography and wet chemical etching to a depth of 3.3μm, which goes through the active region and into the 1400nm AlGaAs n-cladding layer. P-contact metallization on the mesa ridge was formed by 4.0 nm Ti and 300 nm Au deposited by E-beam evaporator to make contact stripes with widths of (45.1 $\pm$ 0.1)µm and (20.2 $\pm$ 1.2)µm. To form the bottom contact, the substrate was lapped to a thickness of 100µm and AuGe/Ni/Au metallization was deposited. The wafer was cleaved to cavities with lengths (L_c) 0.25, 0.3, 0,5 1, 1.5 and 2mm chips to form lasers. These chips were mounted to indium-plated copper heat sinks using indium paste and gold-wire-bonded. A photo of the bonded laser and a magnified photo of the gold stripe top contacts are shown in figure 5.7.

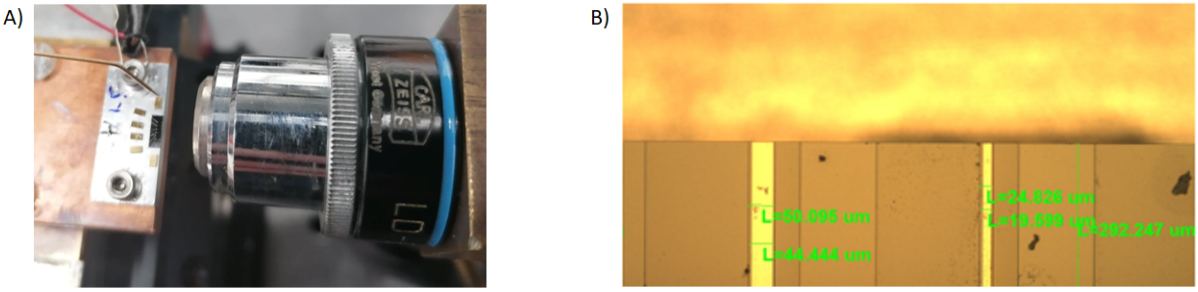

Figure 5.7: Photos of a) the bonded lasers and b) magnified top contacts for the 50μm and 25μm ridges (right). Photo b) was taken by Dr Zhibo Li.

5.5 Results

The fabricated devices were measured using the techniques outlined in Chapter 3: Experimental Methodology. Unless otherwise stated, all measurements are performed in pulsed operation to limit self heating, using a pulse width of 1000ns with a 5kHz repetition rate, a duty cycle of 0.005.

5.5.1 Threshold Current

The threshold current for the n-doped lasers is consistently lower across the temperature range 27 °C - 97 °C for both mesa widths at cavity lengths of 1000μm, 1500μm and 2000μm, with the exception of 1000μm cavity 50μm mesa where the p-type modulation doped device outperforms at 67 °C and above. However, it was found that the near-field width of the n-doped lasers was considerably narrower than the undoped and p-type modulation doped lasers. This has a significant effect on the threshold current density, which translates into direct n-type doping offering a minor improvement in the 2000μm cavity devices. The impact of this is demonstrated in figure 5.8.

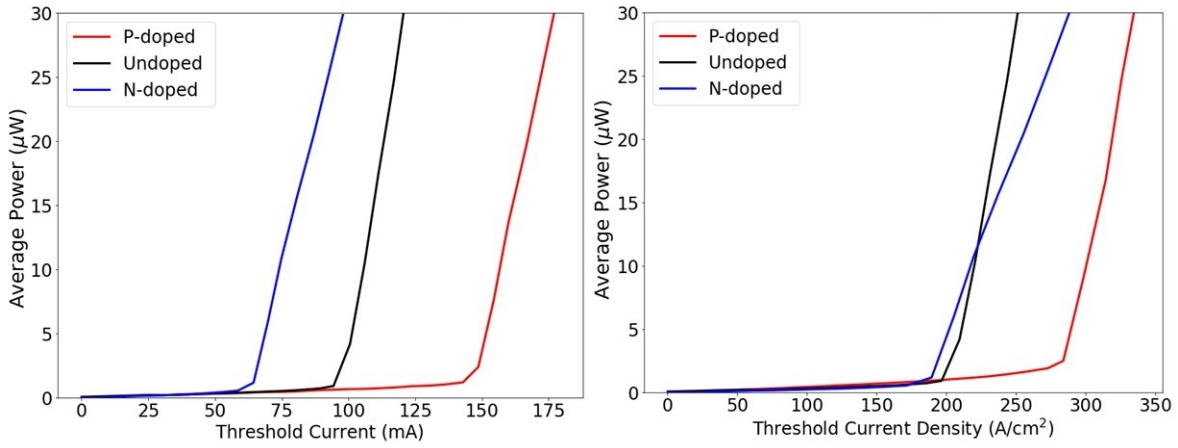

Figure 5.8: Threshold current and threshold current density for single facet average power output for a device with cavity length 2000μm and mesa width 25μm at 27 °C.

5.5.2 Threshold Current Density as a Function of Temperature

The threshold current densities are measured as a function of temperature for all three doping strategies for lasers of cavity lengths 1000μm, 1500μm and 2000μm, with mesas of widths 25μm and 50μm are shown in figure 5.9.

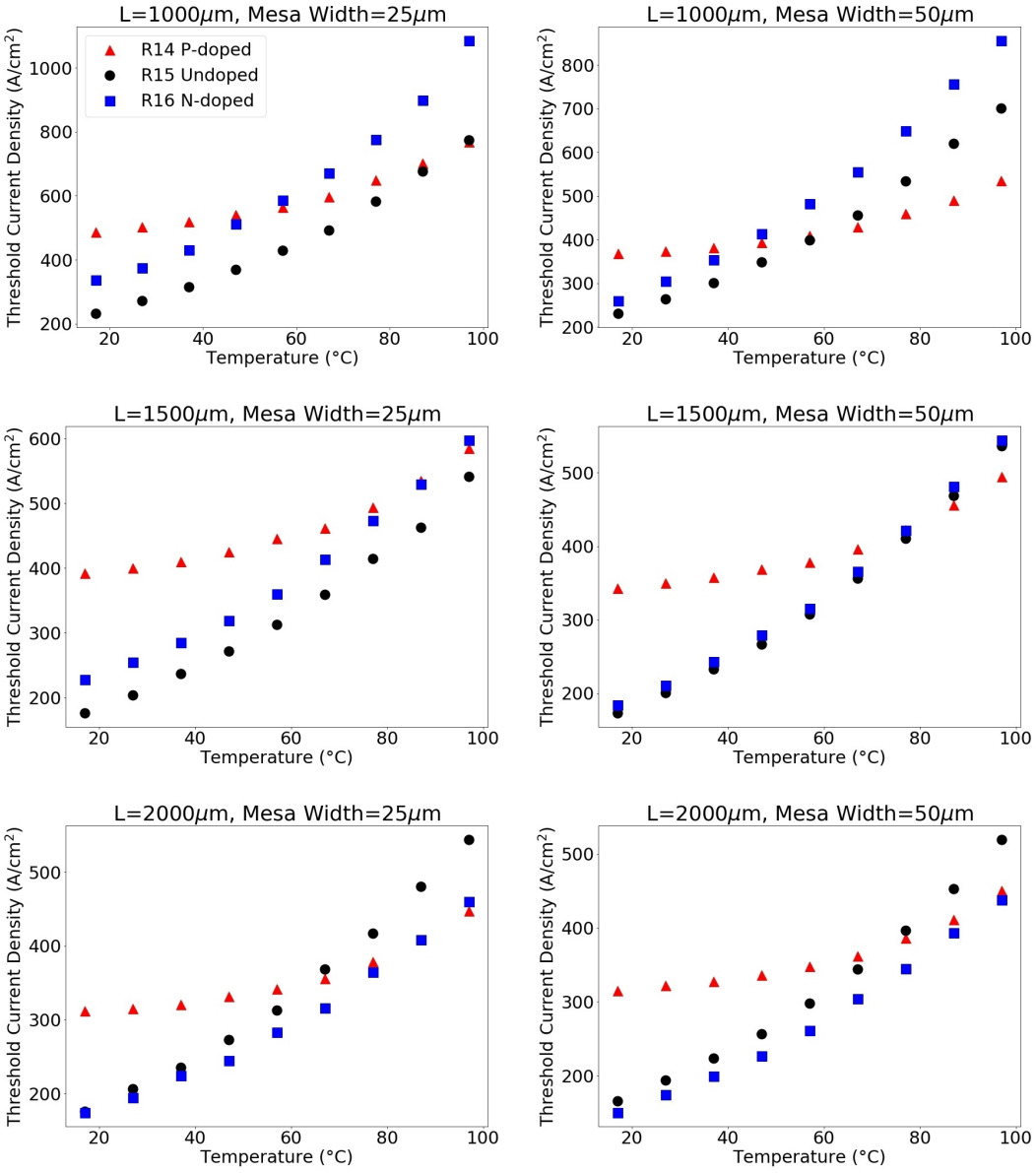

Figure 5.9: Threshold current density as a function of temperature for laser devices that are: p-type modulation doped (red triangles), direct n-type doped (blue squares) and undoped (black circles), for cavity lengths:1000μm (top), 1500μm (middle), 2000μm (bottom), with mesas of widths 25μm (left) and 50μm (right).

Direct n-type doping offering a minor improvement in the 2000μm cavity devices, which have lower gain

requirements. As is seen figure 5.9 and the literature [18], lower gain operation does not benefit from p-type modulation doping in terms of reduction in threshold current density. P-type modulation doped devices operating here do not benefit from the higher available gain and incur additional non-radiative recombination and cavity loss, raising the threshold density significantly at lower temperatures.

As commonly reported in the literature, p-type modulation doped material shows a reduced temperature dependence with threshold current density ($J_{th}(T)$), compared to undoped material [10, 11, 12]. One way of qualifying the degree of temperature dependence is the characteristic temperature (T_0) which can be found using the following equation [19]:

$$J_{th}(T) = \mathrm{J}_{th}\,(\ \mathrm{T}_1)\exp\frac{T - T_1}{T_0} \tag{1}$$

T_0 is calculated over the range of a threshold current with temperature that is exponential. T_1 and $J_{th}(T_1)$ are the initial temperature and threshold current examined, and T and $J_{th}(T)$ is the final temperature and corresponding threshold current of the range of currents being examined.

A high value of T_0 indicates a low rate of change in threshold current with temperature. An infinite T_0 means the threshold current is invariant, and a negative T_0 means the threshold current decreases with increasing temperature.

Characteristic temperature is limited by only applying to exponential sections, which is not always descriptive of the full range of device performance. The threshold current density temperature dependence of both undoped and n-doped devices of all device geometries are can be described by a single exponential across the measured temperature range, meaning the characteristic temperature is calculated for the examined temperature range. However, devices with p-type modulation doping two distinct regimes in $J_{th}(T)$. For a cavity length of 2000μm and a mesa width of 25μm, undoped and n-doped lasers' characteristic temperatures were determined to be as 70.2 K and 74.0 K respectively across the whole temperature range. Comparatively, the p-type modulation-doped laser's two distinct regimes produced two characteristic temperatures in different temperature ranges, at 414.9 K from 17 °C to 57 °C and 155.5 K

from 57 °C to 97 °C respectively. An explanation of why the resultant carrier distribution in p-type modulation doped devices results in this behaviour can be found in section 2.6.3 Charge Carrier Distribution Model.

5.5.3 Threshold Current Density at 27 °C

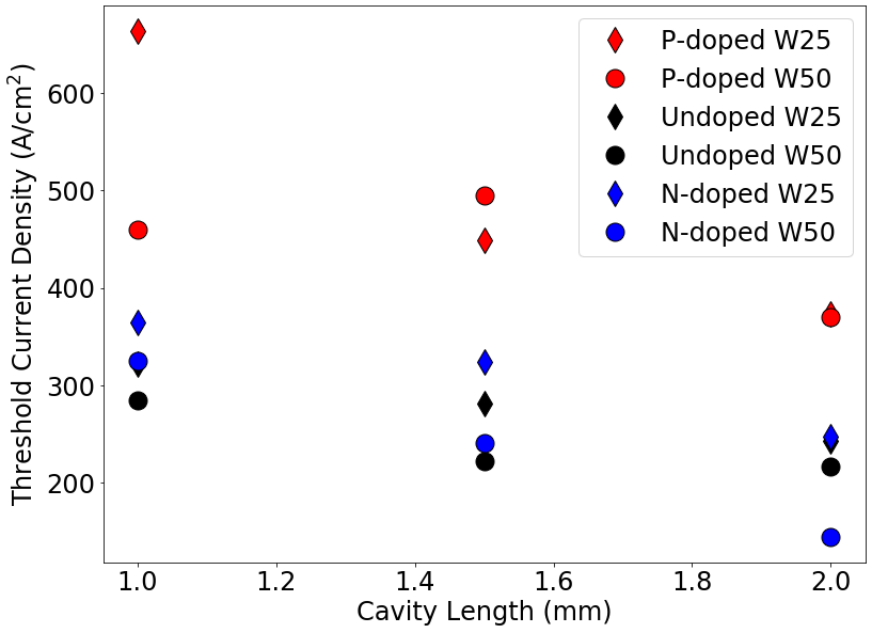

Figure 5.10: Threshold current density as a function of cavity length at 27 °C for lasers with direct n-type doped (blue), p-type modulation doped (red) and undoped (black) active regions.

The threshold current density for a given cavity length should be independent of mesa width, however, figure 5.10 shows significant divergence for the 1mm case for both doping strategies. Numerous repeat measurements were attempted for these devices, and devices exhibited uniform and repeatable performance, from this the error was found to be (463±11)A/cm^2 for the 50μm mesa and (679±11)A/cm^2 for the 25μm mesa. Viable reasons for this deviation could stem from fabrication issues such as poor facet quality or perhaps because there is a small loss associated with the mesa sidewall, which has a greater overlap with the optical mode for the narrow width. Shorter cavities are more sensitive to this, due to the greater impact of distributed mirror loss.

5.5.4 Near-field

Threshold current was converted to threshold current density by inferring the current spreading, achieved by focusing the below threshold light near the facet onto an infrared camera, and calibrating the resultant images to measure the effective area. The near-field width was found by taking the FWHM of the line scan of the maximal intensity region.

It was found that the nearfield width was consistently narrower for devices with direct n-type doping. As shown in the nearfield profile plotted in figure 5.11 for devices with cavity lengths of 2000μm and mesa widths 25μm at 27 °C. The nearfield width is plotted against cavity length for both mesa widths for devices 1000μm, 1500μm and 2000μm at 27 °C in figure 5.12 alongside with reference lines to the contact stripe and mesa widths.

The narrowing indicates that significant gain/loss guiding may be occurring in the structure, causing a reduced lasing spot. This could be caused by significant self focusing within the structure, perhaps due to n-doping changing the material α_H alpha (Henry) parameter, by changes to the charge carrier lifetime or sidewall loss.

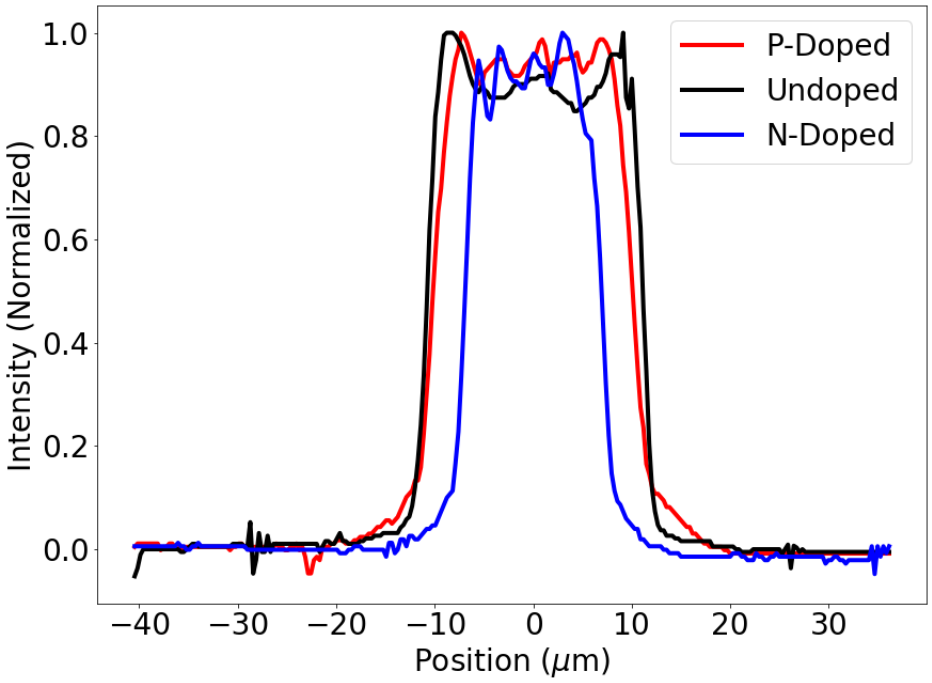

Figure 5.11: Near-field profile at 0.9xi_{th}, of devices with cavity length of 2000μm and mesa width 25μm at 27 °C.

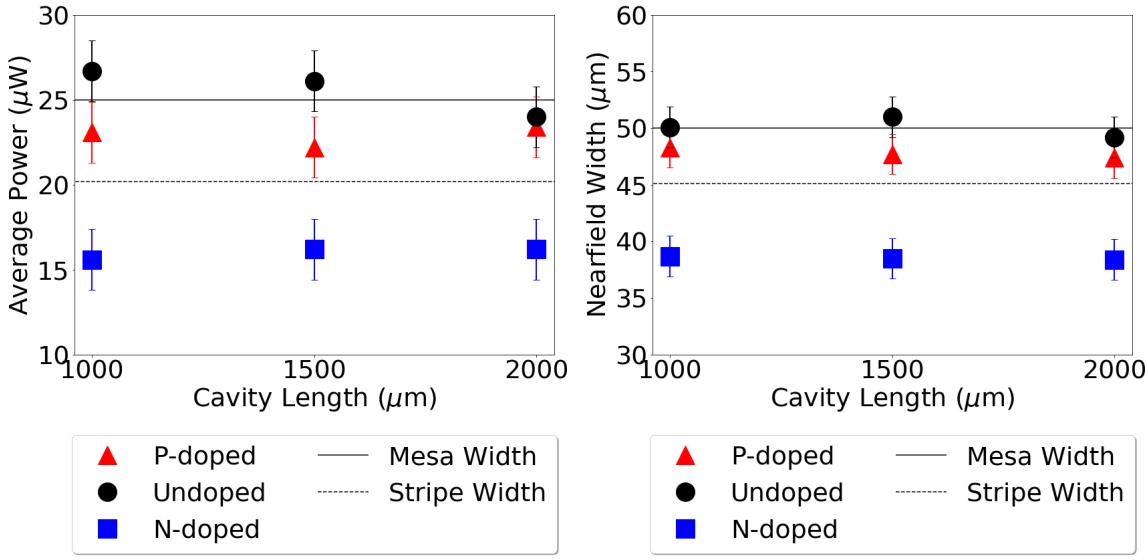

Figure 5.12: Near-field width as a function of cavity length at 0.9xi_{th}, for 1000μm, 1500μm and 2000μm at 27 °C for 25μm (left) and 50μm (right).

5.5.5 Near-field Temperature Dependence

In previous laser devices explored in Chapter 4, the near-field width for both the p-type modulation doped and undoped devices consistently narrowed with increasing temperature. This was thought to be as a result of decreasing charge carrier lifetime. However, no temperature dependence was observed and nearfield width remained consistent for all three doping strategies. For the undoped and p-type modulation doped devices, the near-field widths are similar to the mesa width, so no further inference about the carrier density spreading can be made other than it is greater than the distance from the edge of the gold contact to the edge of the mesa width across the full temperature range.

However, for the n-doped device, the near-field width is significantly lower than the top contact stripe. If the narrowing was related to changes in gain / loss guiding due to reduced carrier spreading in the n-type doped dot material, this might be expected to be reduced at elevated temperatures as electrons can better escape the deeper dot potential - this was not observed here, indicating that the changes in near-field is likely to be caused by changes in the alpha (Henry) parameter or sidewall optical loss.

5.5.6 Experimental Repeatability

I note that for repeat measurements of a single device that the near-field width was found to be reproducible within a tolerance of $\pm 0.96\mu$m. To simulate experimental error, devices were remounted, lens position moved and re-find alignment to simulate changes in the laboratory between measurement sessions.

To assess the variation that arise from variation within a wafer and from fabrication defects, nominally identical devices, in terms of length, mesa width and wafer, of good quality were compared. These also showed a high degree of consistency, with multiple readings showing an experimental error of $\pm 0.83\mu$m, which is lower than the potential experimental error.

5.5.7 Wavelength

Peak wavelength at ith +10% is measured as a function of temperature using the spectral measurements methods outlined in Chapter 3. Readings are taken at 10 degree intervals between 27 °C - 97 °C, for the best performing laser of each device geometry.

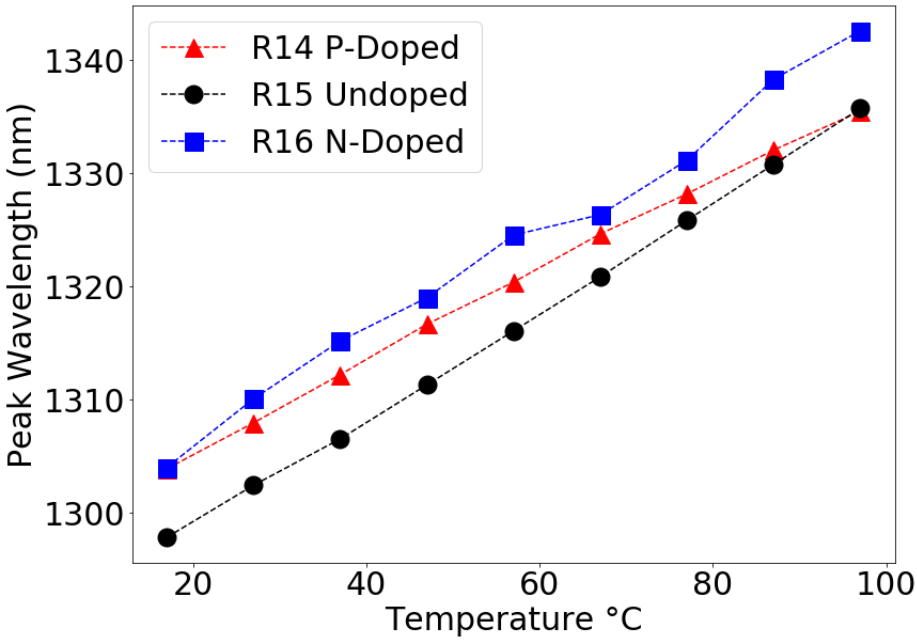

Figure 5.13: Peak wavelength as a function of temperature at 1.1xi_{th}, between 27 °C - 97 °C for devices with cavity length 2000μm and mesa width w25μm, with direct n-type doped (blue squares), p-type modulation doped(red triangles) and undoped (black circles) active regions.

The peak wavelength with temperature, shown in figure 5.13. The direct n-type doped samples experienced a constant red shift, the main mechanism here is the separation of allowed energy states within this potential reduces and causes a lengthening of the emission wavelength. The p-type modulation doped device showed a slight decrease in the temperature dependence of the peak lasing wavelength. These trends were consistent for 1000, 1500 and 2000μm cavity length devices for both mesa widths. The slight decrease in the temperature dependence of the peak lasing wavelength compared to undoped devices was found to be the case for both sets of wafers examined in Chapter 2.6 but not in Chapter 6 indicating that it may be more to do with the growth than the doping.

5.5.8 Lasing State Switch

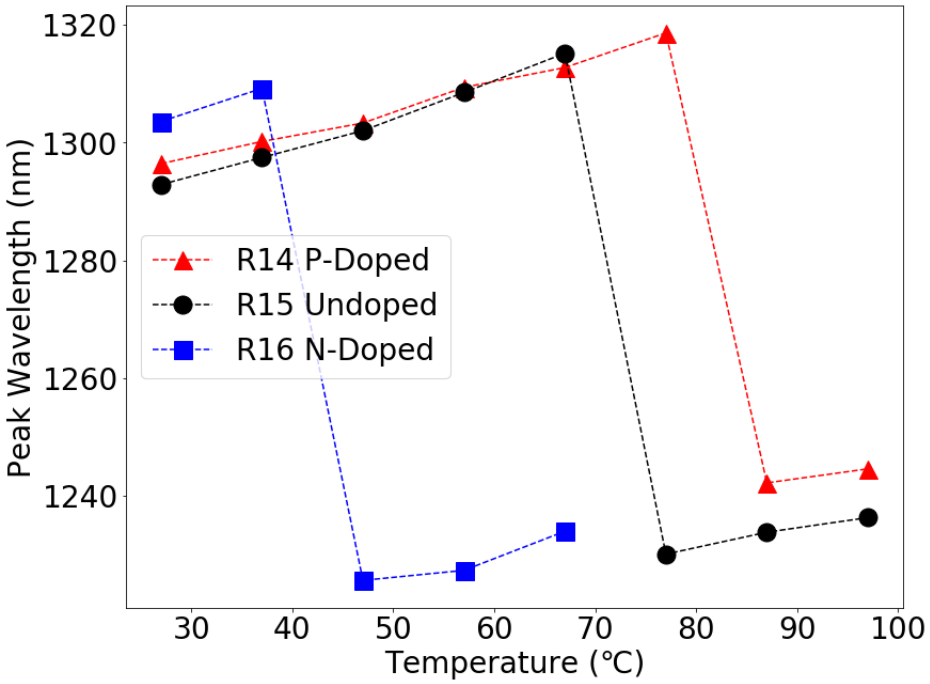

Figure 5.14: Peak wavelength as a function of temperature at at 1.1xi_{th} for laser devices with cavity length 500μm, w50μm, for lasers that are p-type modulation doped (red triangle), undoped (black circle) and direct n-type doped (blue square).

A reduction of cavity length gives rise to a relative increase of mirror loss, so ground-state gain is not enough to overcome the loss for cavities below a certain length and therefore lasing occurs from the excited state [20]. Mirror loss increases with decreasing cavity lengths as the higher gain requirements leads to higher carrier concentrations which cause the absorption to increase [21]. Lasing state switching can also

arise from increasing temperatures causing an increase in carrier spreading, reducing the gain obtained from the ground state. State switching can reduce the suitability of a laser, as many applications are wavelength sensitive and operate over a narrow range of wavelengths. P-type modulation doping causes the excited electron energy states to be relatively depopulated due to the surplus of holes in the valence states [22], so the quasi-Fermi levels are shifted towards the valence states, meaning more charge carriers can be accommodated before needing to fill the excited state. P-type modulation doping delays the switch to excited state lasing both by lowing the quasi Fermi-levels and increasing the available ground state gain, preventing issues with ground state gain saturation. The inverse effect occurs to the quasi-Fermi levels in direct n-type doped devices. For a 500μm cavity, it was observed that the direct n-type doped laser switched from ground to excited state lasing at an operating temperature of 47 °C while the undoped and p-type modulation-doped lasers switched to excited state lasing at 77 °C and 87 °C respectively.

5.6 Experimental Optimisation of N Doping

The previous level of n dopants was selected based on the PL performance of n doped test structures with 0, 0.6, 1.2 and 2.4epd. It was found that the increased in peak in PL emission over the undoped was similar for the 1.2 and 2.4epd doping, with the 1.2epd producing notably less broadening of the PL spectra. However, modelling in Nextnano performed by Benjamin Maglio suggests that the positive effects of increased recombination and gain increase with increasing n type doping.

Three wafers were grown that are nominally identical except for the amount of n doping, which is present at 1.2, 2.4 and 4.8epd. Undoped reference samples are available for comparison. The doping is implemented by applying a flux of silicon atoms during the assembly stage of the Stranski–Krastanov quantum dot growth, to maximize their inclusion within the dots and reduce their impact on dot morphology. Silicon is a group IV element and acts as an amphoteric dopant in III-V compounds, meaning it behaves as a donor or acceptor depending on if it replaces the group III or the group V element. Dopants preferentially occupy the site in the sub-lattice which has the biggest covalent radius [23], which in InAs is Indium. As it replaces the group III element, silicon acts as a donor.

5.6.1 Devices

The structures were grown in the same way as the structures in 5.4 with a number of minor differences. 7 DWELL layers were grown instead of 8 and the GaAs barrier width was increased by 0.5nm. Full wafer details are shown in the left of figure 6.1.

The ridge lasers used 50μm width mesas, produced by conventional photolithography and wet chemical etching. The ridge depth was chosen as 3.3 μm , a depth greater than the device's active region layers. Wafers were fabricated into ridge stripe lasers by Dr. Sara Gillgrass. The stripe P-contact was applied on top of the mesa, of width (40.6 $\pm$ 0.04) μm, formed from 40 nm Ti and 300 nm Au deposited by E-beam evaporator. After lapping to around 100 µm substrate thickness, the AuGe/Ni/Au N-contact was deposited on the bottom of the sample. The as-cleaved facets were clean and mirror-like, which GaAs substrates are well suited to produce. Laser bars were cleaved with cavity lengths, of 1000μm and 2000μm, and then mounted on indium-plated copper heat sinks using a silver loaded epoxy and the top contact wire-bonded to facilitate subsequent measurements. The fabrication details were conveyed to me by discussion and sharing of the process flow record sheets for the devices.

5.6.2 Experimental Results

5.6.3 Near-field

Unlike the direct n-type doped devices investigated previously in section 5.5, we do not observe the narrowing of the lasing spot. There are two reasons why this could be. The first this that the observed narrowing of the near-field could due to over etching of the ridge in the active region, instead of a difference in charge carrier distribution, resulting in a much narrower width in the active region than at the top. However, this narrowing effect was observed to a similar degree for both mesa widths and the measured width was smaller than the applied gold stripe contract width, making this explanation an unlikely occurrence. Alternatively the devices fabricated here could contribute a reduced sidewall optical loss, or it may be that minor changes in growth can yield significant differences between device behaviour, the current could be spreading very different between the devices. To properly examine the impact of current spreading, it would be pertinent to examine some broad area devices where the current could spread

freely.

5.6.4 Threshold Current Density

As the nearfield for all devices is equal to the mesa width across the temperature range, the form of the threshold current is identical to the form of the threshold current density. IVL measurements were performed as a function of temperature from 27 °C - 27 °C by Abigail Enderson, myself and Dr. Pawan Mishra. In contrast to the first direct n-type doped wafer, which had a dopant density of 1.2epd, examined in section 5.5.3, the threshold current density was much higher across the temperature range for devices with both 1000μm and 2000μm cavity lengths and 1.2epd, shown in figures 5.15 and 5.16. Peak power against peak current density at a temperature of 27 °C for both 1000μm and 2000μm cavity lengths are shown in figure 5.17, where it can be seen that the slope efficiency for the 1.2epd is much lower than that of the other three devices, which have similar slope efficiencies. This remains the case over the temperature range investigated. This is indicative that there could be a higher optical loss in the 1.2epd devices. Therefore, the results may not be representative of the effects of direct n-type doping with 1.2epd.

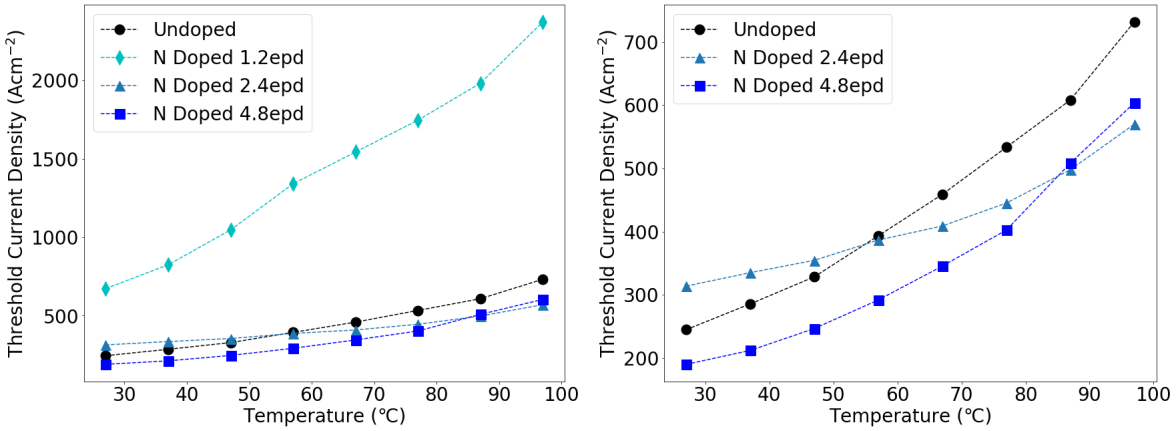

Figure 5.15: Threshold current density as a function of temperature between 27 °C - 97 °C for lasers with cavities of 1000μm, w50μm, for lasers with 0, 1.2, 2.4 and 4.8epd direct n-type doping density (left) and 0, 2.4 and 4.8epd direct n-type doping (right).

The effect of direct n-type doping on the temperature dependence of the threshold current density varies with doping level. With the intermediate n-type doping level of 2.4epd, there is a reduced threshold current density temperature dependence, as can be clearly seen in the right-hand side plot in figure 5.15. The threshold current density is reduced, compared to the undoped and 4.8epd n-doping at higher

temperatures in devices with 1000μm cavity lengths.

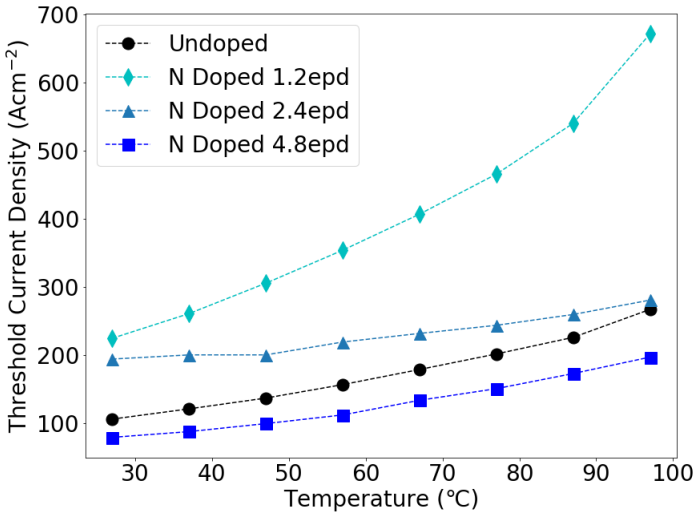

Figure 5.16: Threshold current density as a function of temperature between 27 °C - 97 °C for lasers with cavities of length 2000μm and ridge width 50μm, for lasers with 0, 1.2, 2.4 and 4.8epd direct n-type doping density.

However, there is not a significant difference in the temperature dependence of threshold current density for the 2000μm cavity lasers. Here, the 2.4epd device shows a higher threshold current density across the whole temperature range, though the relative increase reduces at higher temperatures.

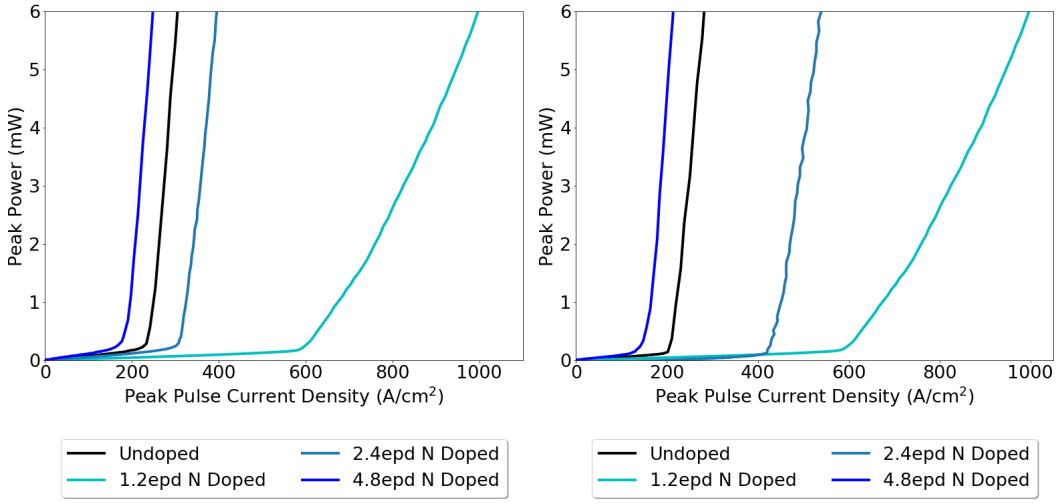

Figure 5.17: Peak pulse current density vs peak pulse power for lasers with 0, 1.2, 2.4 and 4.8epd doping density for lasers with cavities of 1000μm (left) and 2000μm (right) at 27 °C.

5.6.5 Wavelength

A red-shift on operating is brought about as a result of the direct n-type doping. However, this shift is similar for all three levels of n doping at both of the cavity lengths measured. This increase in peak wavelength is brought about primarily as a shift in the structure of the electronic bands, the shorter energy gap results in a longer emission wavelength.

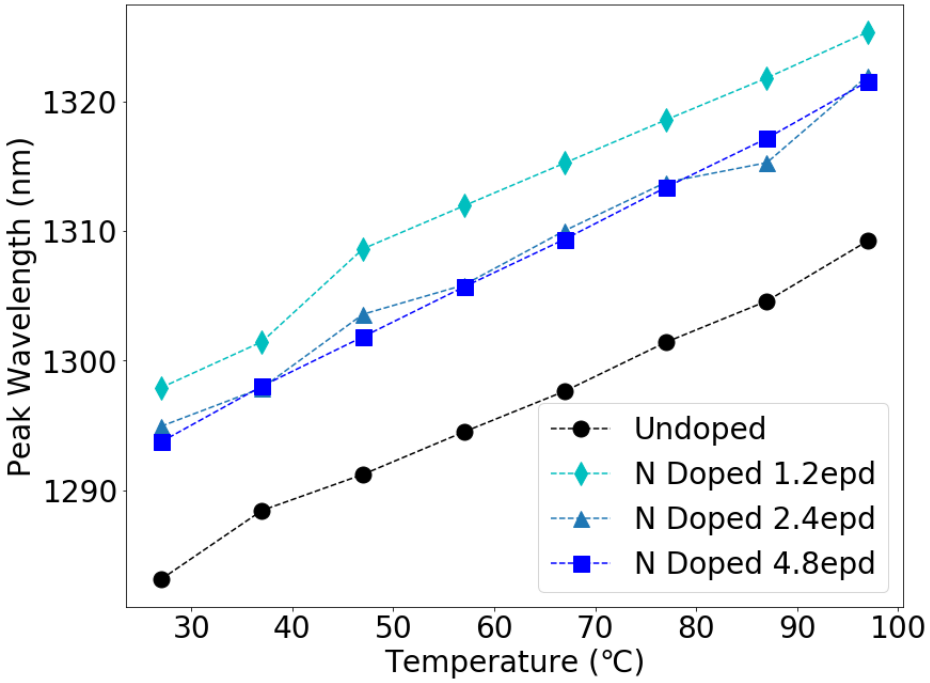

Figure 5.18: Peak wavelength at 1.1x threshold, as a function of temperature for laser devices with 2000μm cavities and 50μm mesa, with direct n-type doped (blue squares), p-type modulation doped (red triangles) and undoped (black circles) active regions.

5.7 Comparison with Current Literature

This work presents the first study of direct experimental examination of normally identical laser devices with p-type modulation doping and direct n-type doping, which has also been published in Journal of Physics D [5].

To date, two other papers have been published on n-type doping of InAs quantum dot lasers [1] [2]. A minimum threshold current is achieved in CW operation, 71.6A/cm^2 for a 2500μm cavity with 5 DWELL layers at 20 °C [1]. A doping density of 1.4epd is used.

This is very close to the 79.7^2 measured at 27 °C for a 2000μm long laser reported in section 5.6. This device had a higher doping level of 4.8epd and 7DWELL layers. However, the device was measured in pulsed operation which can report a lower current due to less self heating effects, meaning a direct comparison is not possible.

Within the literature, investigations into the effects of different levels of direct n-type doping focus solely on PL performance, in section 5.6, results are presented looking at the effect of different amounts of doping on laser devices of multiple lengths.

Furthermore, neither paper considers the effect of n doping on the device's ability to maintain ground state lasing, making the data shown in figure 5.14 of particular use.

5.8 Chapter Summary

A study was presented comparing InAs/GaAs QD laser performance for devices fabricated from wafers with direct n-type doped, p-type modulation-doped and unintentionally doped active regions by measuring threshold current, nearfield width and peak wavelength across the temperature range 17 °C – 97 °C.

The n doping level was optimised by examining the PL characteristics of test structures with 0, 0.6, 1.2 and 2.4 epd. A doping density of 1.2epd was selected, as it provided comparable PL intensity increase to 2.4epd without as significant PL spectral broadening (FWHM).

Direct n-type doping reduced the threshold current significantly compared to the undoped samples for all measured device geometries for devices with cavity lengths 1000, 1500 and 2000μm across 17 °C – 97 °C. However, direct n-type doping only had modest impact on reducing the threshold current density due to relative narrowing of the near field lasing spot. This narrowing effect is likely to be caused by changes in the alpha (Henry) parameter or reduced side wall recombination loss. N-type doping results in the negative effect of the lasing state switching from ground to excited state occurring at longer cavities and at lower operating temperatures compared to the undoped and p-type modulation doped devices. The greatest improvement to the threshold current density took place in the longer 2000μm cavities, which have lower gain requirements.

In contrast, the p-type modulation-doped lasers were found to have a better performance in regimes of higher gain requirements: shorter cavity lengths and higher temperatures. This came at the expense of significantly increasing the threshold current density in lower temperature ranges 17 °C – 57 °C. As seen in previous chapters and the literature, P-modulation doping improved the characteristic temperature (T_0), which was observed to more than 400 K up to 60 °C, compared to 70 K and 74k for undoped and direct n-doped lasers respectively for devices with a 2000μm cavity length and a 25μm mesa. P-type modulation doping also delayed switching of lasing from the ground to excited state compared with the undoped device. A 500μm cavity laser with p-type modulation doping achieved ground state lasing up to 77 °C compared to 67 °C for an undoped device, the direct n-type doped device switched at lower threshold current densities - maintaining ground state lasing at 37 °C and below.

Direct n type doping was found to reduce the threshold current density compared to undoped devices for 4.8epd between 27 °C – 97 °C for devices with cavity lengths 1000μm and 2000μm. A further reduction was achieved by 2.4epd for the shorter 1000μm cavity at higher temperatures.

References

[1] Z.-R. Lv, Z.-K. Zhang, X.-G. Yang, and T. Yang. "Improved performance of 1.3- μ m InAs/GaAs quantum dot lasers by direct Si doping". In: *Applied Physics Letters* 113.1 (July 2, 2018).

[2] Y.-Q. Qiu, Z.-R. Lv, H. Wang, H.-M. Wang, X.-G. Yang, and T. Yang. "Improved linewidth enhancement factor of 1.3- μ m InAs/GaAs quantum dot lasers by direct Si doping". In: *AIP Advances* 11.5 (May 1, 2021).

[3] B. Maglio, L. Jarvis, C. P. Allford, S.-J. Gillgrass, S. Shutts, M. Tang, H. Liu, and P. M. Smowton. "The limits to peak modal gain in p-modulation doped indium arsenide quantum dot laser diodes". In: *2021 IEEE Photonics Conference (IPC)*. Oct. 2021.

[4] B. Maglio, L. Jarvis, M. Tang, H. Liu, and P. M. Smowton. "Modeling the effects of p-modulation doping in InAs quantum dot devices". In: *2021 International Conference on Numerical Simulation of Optoelectronic Devices (NUSOD)*. Sept. 2021.

[5] H. Deng, L. Jarvis, Z. Li, Z. Liu, M. Tang, K. Li, J. Yang, B. Maglio, S. Shutts, J. Yu, L. Wang, S. Chen, C. Jin, A. Seeds, H. Liu, and P. M. Smowton. "The role of different types of dopants in 1.3 μm InAs/GaAs quantum-dot lasers". In: *Journal of Physics D: Applied Physics* 55.21 (May 26, 2022).

[6] T. Inoue, S. Kido, K. Sasayama, T. Kita, and O. Wada. "Impurity doping in self-assembled InAs/GaAs quantum dots by selection of growth steps". In: *Journal of Applied Physics* 108.6 (Sept. 15, 2010).

[7] X. Yang, K. Wang, Y. Gu, H. Ni, X. Wang, T. Yang, and Z. Wang. "Improved efficiency of InAs/GaAs quantum dots solar cells by Si-doping". In: *Solar Energy Materials and Solar Cells* 113 (June 1, 2013).

[8] T. Kita, R. Hasagawa, and T. Inoue. "Suppression of nonradiative recombination process in directly Si-doped InAs/GaAs quantum dots". In: *Journal of Applied Physics* 110.10 (Nov. 15, 2011).

[9] P. M. Smowton, I. C. Sandall, H. Y. Liu, and M. Hopkinson. "Gain in p-doped quantum dot lasers". In: *Journal of Applied Physics* 101.1 (Jan. 2007).

[10] L. V. Asryan and S. Luryi. "Temperature-insensitive semiconductor quantum dot laser". In: *Solid-State Electronics* 47.2 (Feb. 2003).

[11] T. J. Badcock, R. J. Royce, D. J. Mowbray, M. S. Skolnick, H. Y. Liu, M. Hopkinson, K. M. Groom, and Q. Jiang. "Low threshold current density and negative characteristic temperature 1.3μm InAs self-assembled quantum dot lasers". In: *Applied Physics Letters* 90.11 (Mar. 12, 2007).

[12] O. Shchekin and D. Deppe. "Low-threshold high-T0 1.3-μm InAs quantum-dot lasers due to p-type modulation doping of the active region". In: *IEEE Photonics Technology Letters* 14.9 (Sept. 2002).

[13] D. Jung, R. Herrick, J. Norman, K. Turnlund, C. Jan, K. Feng, A. C. Gossard, and J. E. Bowers. "Impact of threading dislocation density on the lifetime of InAs quantum dot lasers on Si". In: *Applied Physics Letters* 112.15 (Apr. 9, 2018).

[14] J. S. Kim, P. W. Yu, J.-Y. Leem, J. I. Lee, S. K. Noh, J. S. Kim, G. H. Kim, S.-K. Kang, S. I. Ban, S. G. Kim, Y. D. Jang, U. H. Lee, J. S. Yim, and D. Lee. "Growth of Si-doped InAs quantum dots and annealing effects on size distribution". In: *Journal of Crystal Growth* 234.1 (Jan. 2002).

[15] J. Phillips, K. Kamath, X. Zhou, N. Chervela, and P. Bhattacharya. "Photoluminescence and far-infrared absorption in Si-doped self-organized InAs quantum dots". In: *Applied Physics Letters* 71.15 (Oct. 13, 1997).

[16] H. Y. Liu, I. R. Sellers, T. J. Badcock, D. J. Mowbray, M. S. Skolnick, K. M. Groom, M. Gutiérrez, M. Hopkinson, J. S. Ng, J. P. R. David, and R. Beanland. "Improved performance of 1.3μm multilayer InAs quantum-dot lasers using a high-growth-temperature GaAs spacer layer". In: *Applied Physics Letters* 85.5 (Aug. 2, 2004).

[17] S. Tiku and D. Biswas. *III-V Integrated Circuit Fabrication Technology*. CRC Press, Apr. 27, 2016. 706 pp.

[18] Y. Cao, T. Yang, H. Ji, W. Ma, Q. Cao, and L. Chen. "Temperature Sensitivity Dependence on Cavity Length in p-Type Doped and Undoped 1.3-μ m InAs–GaAs Quantum-Dot Lasers". In: *IEEE Photonics Technology Letters* 20.22 (Nov. 2008).

[19] L. A. Coldren, S. W. Corzine, and M. L. Mashanovitch. *Diode Lasers and Photonic Integrated Circuits*. John Wiley & Sons, Mar. 2, 2012. 684 pp.

[20] K. Sears, M. Buda, H. H. Tan, and C. Jagadish. "Modeling and characterization of InAsGaAs quantum dot lasers grown using metal organic chemical vapor deposition". In: *Journal of Applied Physics* 101.1 (Jan. 2007).

[21] J. Piprek. "Chapter 7 - Edge-Emitting Laser". In: *Semiconductor Optoelectronic Devices*. Ed. by J. Piprek. Boston: Academic Press, Jan. 1, 2003.

[22] M. Saldutti, A. Tibaldi, F. Cappelluti, and M. Gioannini. "Impact of carrier transport on the performance of QD lasers on silicon: a drift-diffusion approach". In: *Photonics Research* 8.8 (Aug. 1, 2020).

[23] R. Venkatasubramanian, D. L. Dorsey, and K. Mahalingam. "Heuristic rules for group IV dopant site selection in III–V compounds". In: *Journal of Crystal Growth* 175-176 (May 1997).

6 Co-doping Approach

6.1 Introduction

A novel method to improve gain is investigated, where the active region of laser devices were doped with both p-type modulation doping and direct n-type doping simultaneously, referred to hence as co-doping. Four different wafers were grown: with p-type modulation doping, direct n-type doping, co-doping and with no doping present in the DWELL layers. Devices were fabricated into lasers of different lengths to investigate the impact of co-doping and compare the effects to both individual approaches and to devices with no doping. Threshold current, near-field with and peak wavelength were measured as a function of temperature.

Co-doping with 10 holes per dot (hpd) and 1.2 electrons per dot (epd) produced excellent improvements in device performance, when contrasted with undoped, p-type modulation doped and direct n-type doped samples. Co-doped had a far lower threshold current density across the temperature range 27 °C - 97 °C for both 1000μm and 2000μm cavity lengths. The 1000μm showed a reduction in threshold current density from 245Acm^{-2} to 132Acm^{-2} at 27 °C and 731Acm^{-2} to 312Acm^{-2} at 97 °C. Co-doping retains the benefit of reduced threshold temperature dependence and for a given cavity length maintains ground state emission at higher temperatures.

6.2 Co-doping Mechanism

To explain the impact of the doping combination, figure 6.1 shows a band diagram of a single DWELL layer for a doped and undoped structure. Both mechanisms improve the gain by increasing the population of the H_1 state. The p-type modulation doping layer is to the right, and dopant holes (red circles) diffuse into the active region. These dopant holes are distributed over valence band states, increasing the population of holes in the H_1 state. In direct n-type doping, the dopant is directly incorporated into the dot. The dopant ionizes, creating a positive potential within the quantum dot. The positive ion within the quantum dot alters the dot's potential, reducing the number of confined hole states, which increases the probability of an electron being found in the H_1 state.

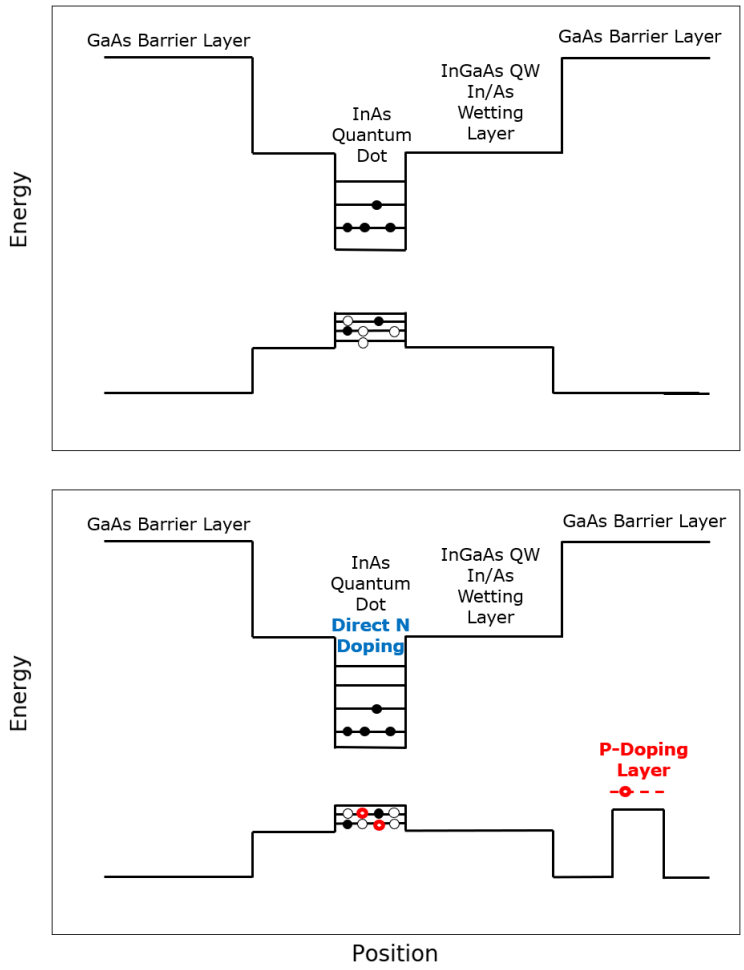

Figure 6.1: Schematic diagram showing energy levels and for singular DWELL layer for top: an undoped wafer and bottom: a wafer co-doped with p-type modulation doping and direct n-type doping. Black circles are electrons, white circles are holes and red circles are dopant holes.

6.3 Structure

The p-type modulation doping was implemented with a resultant doping density of 10hpd, as was found to be the optimal doping density in Chapter 4. The n doped wafer in this chapter refers to a doping of 4.8epd, as this was found experimentally to be the best performing N-doped structure, out of the set examined section in 5.6. The level of n doping in the co-doped wafer was 1.2epd and was selected on the bases of the PL optimisation in section 5.3, as the co-doped wafer was grown at the same time as the wafers for the direct n-type optimisation study. The direct n-type doping was applied by the addition of a flux of silicon atoms during the assembly stage of dot growth [1].

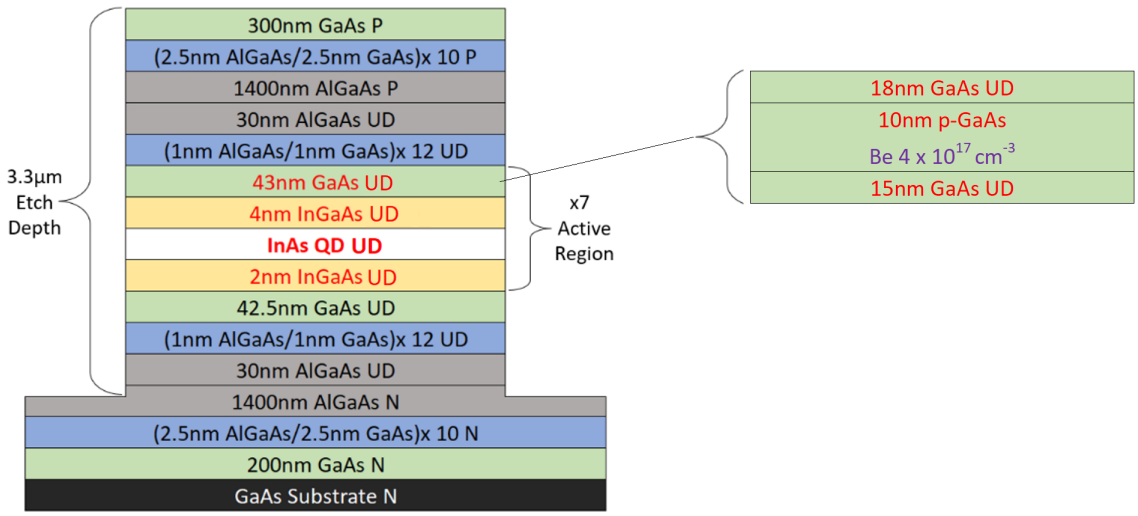

Figure 6.2: Left: schematic diagram of the wafer (not to scale), right: schematic diagram of the modified GaAs barrier layer for wafers containing p-type modulation doping.

The structures were grown in the same way as the structures in 5.4 with a number of minor differences. 7 DWELL layers were grown instead of 8 and the GaAs barrier width was increased by 0.5nm. Full wafer details are given in figure 6.1.

The ridge lasers used 50μm width mesas, produced by conventional photolithography and wet chemical etching. The ridge depth was chosen as 3.3 μm, a depth greater than the device's active region layers. Wafers were fabricated into ridge stripe lasers by Dr. Sara Gillgrass. The stripe P-contact was applied on top of the mesa, of width (40.6 $\pm$ 0.04) μm, formed from 40 nm Ti and 300 nm Au deposited by E-beam evaporator. After lapping to around 100 µm substrate thickness, the AuGe/Ni/Au N-contact was deposited on the bottom of the sample. The as-cleaved facets were clean and mirror-like, which GaAs substrates are well suited to produce. Laser bars were cleaved with cavity lengths, of 1000μm and 2000μm, and then mounted on copper heat sinks using a silver loaded epoxy and the top contact wire-bonded to facilitate subsequent measurements.

6.4 Measurement Results

The fabricated devices were measured using the techniques outlined in Chapter 3: Experimental Methodology. All measurements are performed in pulsed operation to limit self heating, using a pulse

width of 1000ns with a 5kHz repetition rate, a duty cycle of 0.005.

6.4.1 Near-field

Using the method outlined in 3.6.1 the near-field width for the lasers was measured. The width of all four devices for both 1000μm and 2000μm cavity lengths was found to be the same as the mesa width (50 $\pm$ 1.0)μm across the temperature range 27 °C - 97 °C.

6.4.2 Threshold Current Density

As there is minimal difference in effective near-field between the doping types, the behaviour of threshold current and the threshold current density is identical. Across the temperature range, the co-doped sample shows a significant reduction in threshold current density for both 1000μm and 2000μm cavity lengths.

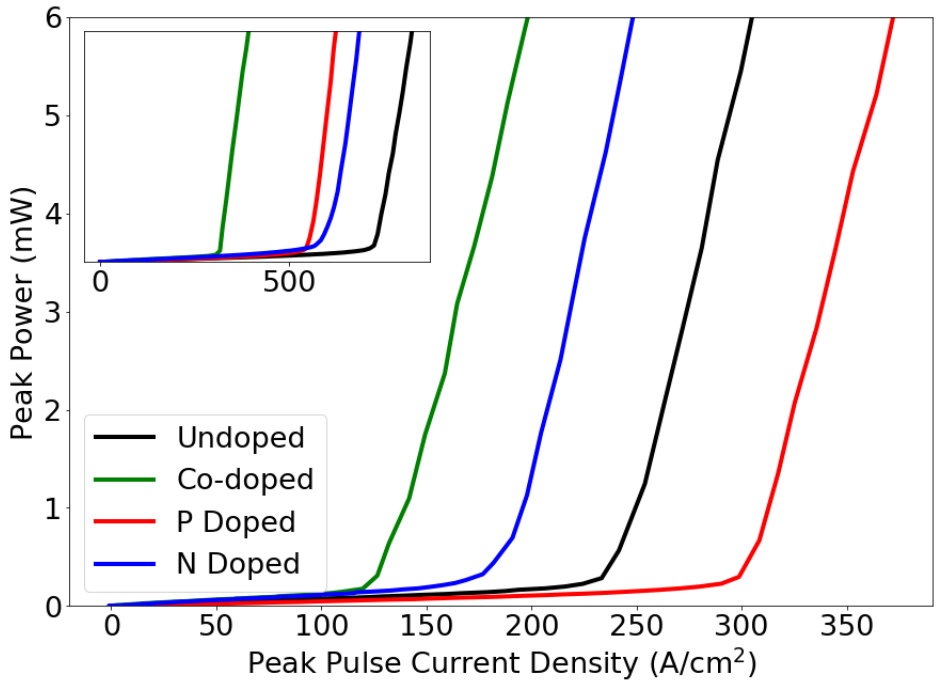

Figure 6.3: Single facet peak power vs peak current density for devices with cavity length 1000μm at 27 °C (main) and at 97 °C (insert).

The pulse peak power output versus peak current density characteristic, figure 6.3 shows a similar slope efficiency for all four structure types with the co-doped structure exhibiting the lowest threshold current

density at both 27 °C and 97 °C. The similarity of the differential efficiency for all four device types in these 1000μm long lasers indicates that the doping is not having a significant effect on the optical loss and that the changes in threshold current density most likely arise from differences in the amount non-radiative recombination.

The threshold current density for 1000μm cavity lasers is plotted as a function of temperature in figure 6.4. The direct n-type doping approach results in a reduction of threshold current density relative to the undoped device across the full range, however, these two methods produce a similar temperature dependence for the threshold current density. P-type modulation doping provides reductions over the undoped from 50 °C and the direct n-type doped device from 80 °C. As is previously observed in chapters 4, 5 and in the literature [2, 3, 4] p-type modulation doping offers a reduction in the temperature dependence of threshold current density. For a description of the mechanism that governs this effect, see section 2.6.3. This improvement in reduced temperature dependence is retained with the addition of direct n-type doping in the co-doped device, alongside a significant improvement in threshold current density across the whole temperature range. This is reflected in the characteristic temperature (T_0), which for 1000μm long lasers is 64.0K for the undoped device, 60.6K for 4.8epd direct n-type doping, 115K for p-type modulation doping with 10hpd and 81.3K for a device co-doped with 1.2epd direct n doping and 10hpd p-type modulation doping.

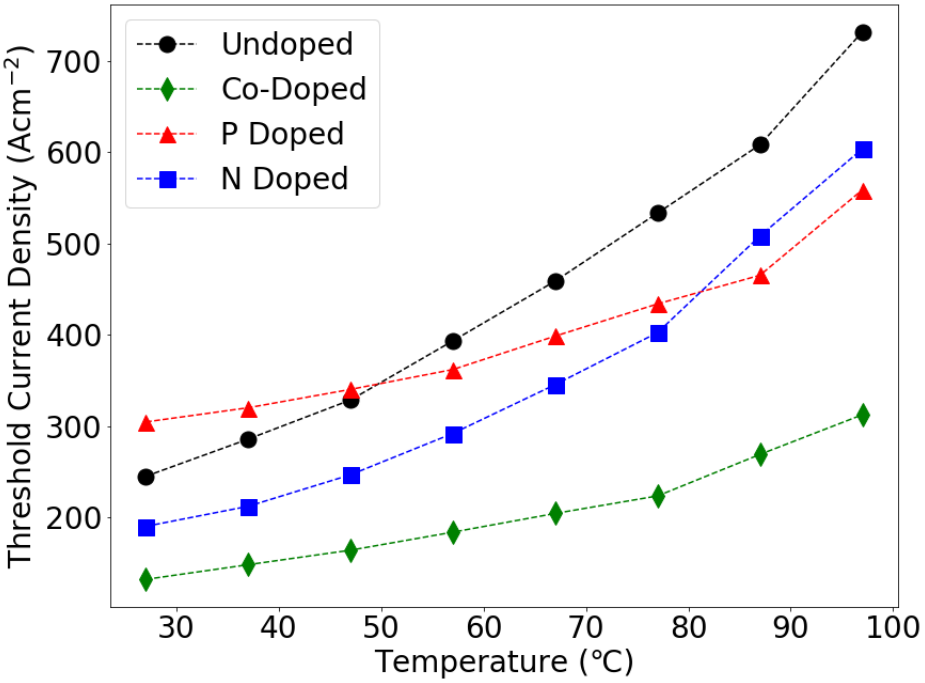

Figure 6.4: Threshold current density as a function of temperature for devices with a cavity length of 1000μm.

The 2000μm device with p-type modulation doping has the highest threshold current density across the temperature range, shown in figure 6.5, as for longer lasers the loss, and hence gain requirement, is reduced [5]. Here, the p-type modulation doped device does not benefit from the higher gain available [6] (sometimes at lower currents compared with the undoped) but still experiences the deleterious effects of increased non-radiative recombination. However, co-doping still produces the lowest threshold current over the whole temperature range. As with the 1000μm device, the temperature dependence is reduced for both the p-type modulation doped and co-doped devices compared to undoped and direct n-type doped devices.

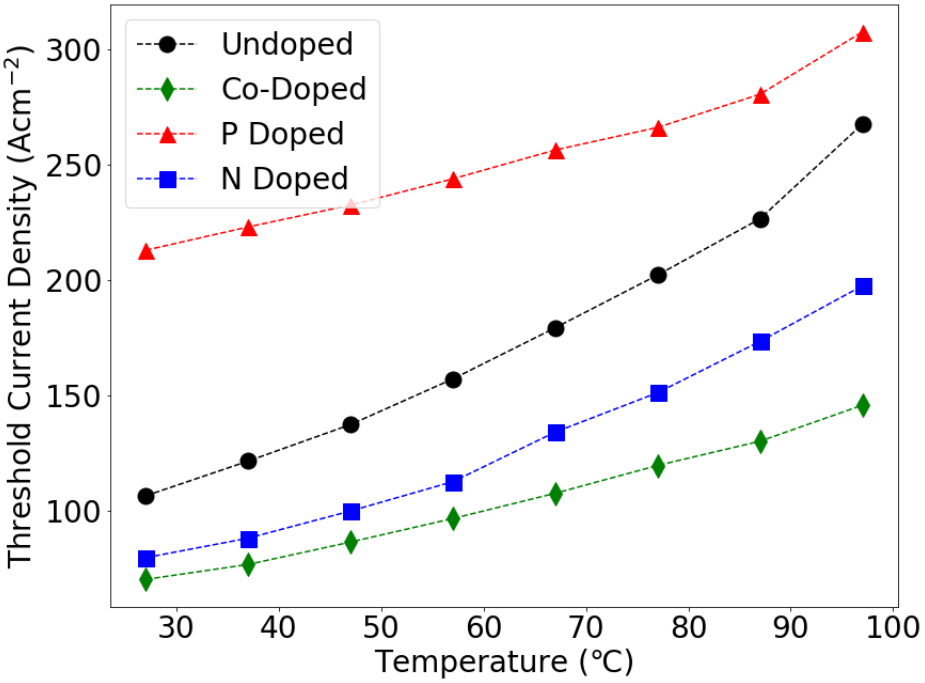

Figure 6.5: Threshold current density as a function of temperature for devices with a cavity length of 2000μm.

6.5 Wavelength

The peak wavelength as a function of temperature was measured across the temperature range and was found to be similar for all four approaches, with a small red-shift compared to the undoped case.

6.5.1 Lasing State Switch

As in Chapter 5 section 5.5.8, the peak wavelength as a function of temperature was measured for cavities of reduced lengths to determine the relative conditions for switching from ground to excited state lasing. However, despite cleaving cavities 125μm apart, there was not one single length that captured the lasing state transition for all devices. For a cavity length of 500μm, all four devices lased on the excited state from 27 °C.

In figure 6.7, the peak lasing wavelength as a function of temperature is plotted for both a co-doped and p-type modulation doped device with cavity length of 625μm. For this cavity length, both undoped and direct n-type doped devices lased on the excited state from 17 °C.

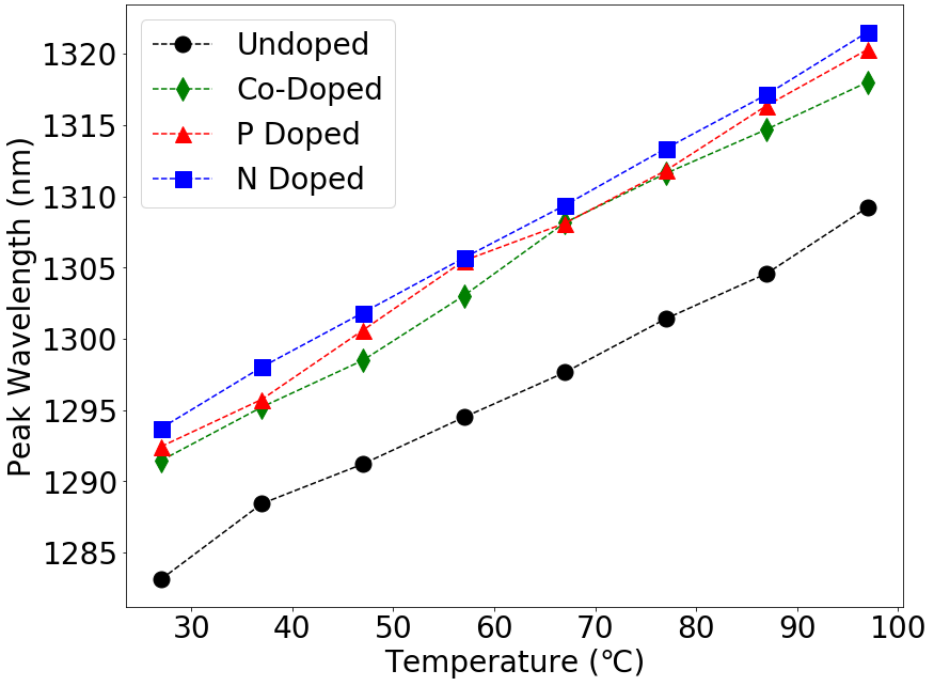

Figure 6.6: Peak wavelength at 1.1xi_{th}, as a function of temperature for devices with a cavity length of 2000μm.

In undoped devices, gain is achieved via excited state lasing before the ground state fully populates, due to the increased spread of the hole carriers leading to incomplete state filling [7]. This is countered by the excess holes provided by p-type modulation doping [8]. Furthermore, p-type modulation doping increases the ground state saturation gain [9, 10], also contributing to the extension of ground state lasing conditions to shorter cavities and at increased temperatures. The relative position of the quasi Fermi levels also controls whether if a device is lasing from the ground or excited state. The impact of direct n-type doping and p-type modulation doping on the quasi Fermi levels is discussed in section 5.5.8.

In the co-doped device, the higher amount of p-type dopant (10hpd) compared with n-type dopant (1.2epd) results in a net lowering of the quasi Fermi levels, contributing to the delaying of the transition from ground to excited state lasing relative to the undoped device, achieving ground state lasing at 27 °C and below for lasers of cavity length 625μm. P-type modulation doping alone extended ground state lasing up to 67 °C.

For a cavity length of 750μm, the p-type modulation doped, co-doped and undoped device lased from the ground state across the temperature range 27 °C - 97 °C. The direct n-type doped device transitioned to

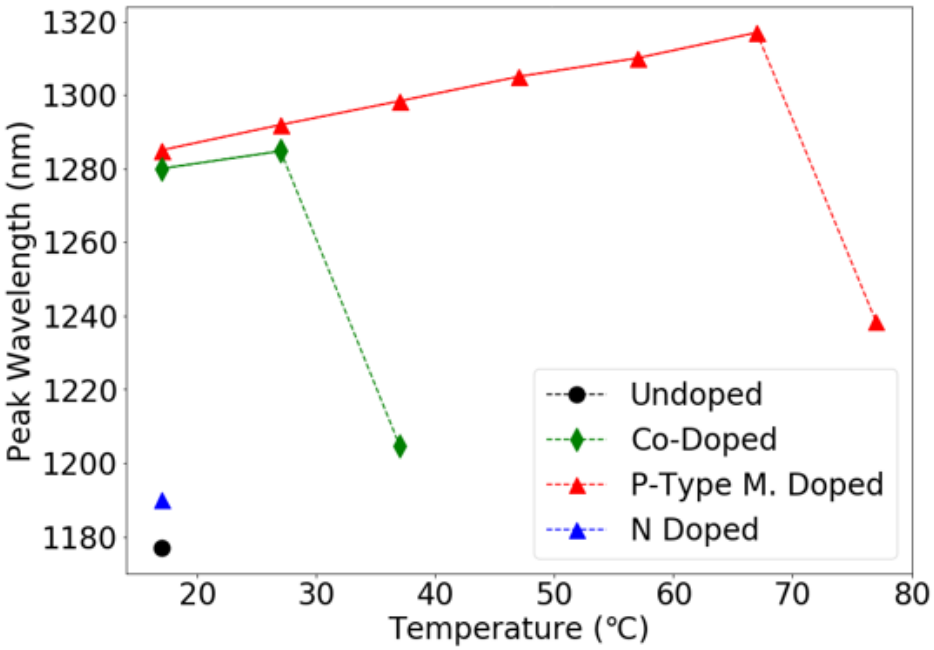

Figure 6.7: Peak wavelength at 1.1xi_{th}, as a function of temperature for a co-doped and p-type modulation doped device with cavity length of 625μm.

excited state lasing at 87 °C, due to the raised quasi Fermi levels.

6.6 Chapter Summary

A novel approach to improve the performance of InAs quantum dot lasers where the active region of laser devices were doped with both p-type modulation doping and direct n-type doping simultaneously, termed co-doping, was investigated experimentally. Performance of co-doped laser devices was compared with devices with p-type modulation doping and direct n-type doping alone, alongside nominally undoped reference devices.

It was found that co-doping improved performance in terms of threshold current density more than either approach individually. At this point, one may wonder whether direct n-doping is simply reducing the effect of the level of p-type modulation doping and fortuitously optimising it to achieve both a low threshold current density and a reduced sensitivity of the threshold current to temperature. However, if this was the case, the direct n-type doping would not reduce threshold current relative to the undoped sample as demonstrated in Chapter 5. It is clear that there are separate and complementary processes by which

direct n-doping and modulation p-doping improve performance.

A co-doped device with a cavity length of 1000μm with uncoated facets showed a reduction in threshold current density from 245Acm^{-2} to 132Acm^{-2} at 27 °C and 731Acm^{-2} to 312Acm^{-2} at 97 °C, compared to the undoped case. Co-doping also improved the temperature dependence of threshold current density and, due to the greater amount of p-dopant than n-dopant, extended the range of conditions over which ground state lasing could occur relative to undoped and direct n-type doped devices. Results indicate that while p-type modulation doping can improve the threshold current temperature dependence, the further addition of direct n-doping is necessary to also reduce the magnitude of threshold current density.

References

[1] T. Inoue, S. Kido, K. Sasayama, T. Kita, and O. Wada. "Impurity doping in self-assembled InAs/GaAs quantum dots by selection of growth steps". In: *Journal of Applied Physics* 108.6 (Sept. 15, 2010).

[2] O. Shchekin and D. Deppe. "Low-threshold high-T0 1.3-μm InAs quantum-dot lasers due to p-type modulation doping of the active region". In: *IEEE Photonics Technology Letters* 14.9 (Sept. 2002).

[3] S. Fathpour, Z. Mi, P. Bhattacharya, A. R. Kovsh, S. S. Mikhrin, I. L. Krestnikov, A. V. Kozhukhov, and N. N. Ledentsov. "The role of Auger recombination in the temperature-dependent output characteristics (T0=∞) of p-doped 1.3 μm quantum dot lasers". In: *Applied Physics Letters* 85.22 (Nov. 29, 2004).

[4] I. P. Marko, N. F. Massé, S. J. Sweeney, A. D. Andreev, A. R. Adams, N. Hatori, and M. Sugawara. "Carrier transport and recombination in p-doped and intrinsic 1.3μm InAs/GaAs quantum-dot lasers". In: *Applied Physics Letters* 87.21 (Nov. 21, 2005).

[5] K. Sears, M. Buda, H. H. Tan, and C. Jagadish. "Modeling and characterization of InAsGaAs quantum dot lasers grown using metal organic chemical vapor deposition". In: *Journal of Applied Physics* 101.1 (Jan. 2007).

[6] Y. Cao, T. Yang, H. Ji, W. Ma, Q. Cao, and L. Chen. "Temperature Sensitivity Dependence on Cavity Length in p-Type Doped and Undoped 1.3-μ m InAs–GaAs Quantum-Dot Lasers". In: *IEEE Photonics Technology Letters* 20.22 (Nov. 2008).

[7] G. Park, O. Shchekin, and D. Deppe. "Temperature dependence of gain saturation in multilevel quantum dot lasers". In: *IEEE Journal of Quantum Electronics* 36.9 (Sept. 2000).

[8] M. Saldutti, A. Tibaldi, F. Cappelluti, and M. Gioannini. "Impact of carrier transport on the performance of QD lasers on silicon: a drift-diffusion approach". In: *Photonics Research* 8.8 (Aug. 1, 2020).

[9] P. M. Smowton, I. C. Sandall, H. Y. Liu, and M. Hopkinson. "Gain in p-doped quantum dot lasers". In: *Journal of Applied Physics* 101.1 (Jan. 2007).

[10] C. Zhang and J. E. Bowers. "Silicon photonic terabit/s network-on-chip for datacenter interconnection". In: *Optical Fiber Technology* 44 (Aug. 2018).

7 Conclusions and Further Work

7.1 Conclusions

This thesis examined three different methods for overcoming the low gain present in III-V quantum dot laser materials.

P-type modulation doping was investigated and optimised for a given wafer structure. The optimal doping level was found to be 10 holes per dot (hpd), which resulted in non-thermal distributions at high temperatures and was evidenced by the temperature dependence of both threshold current density and the spectral width. Increased doping levels of 15hpd extended regions of temperature invariant threshold between $-17\,^{\circ}\mathrm{C}$ and $67\,^{\circ}\mathrm{C}$ for devices with cavity lengths of 2000μm and above, but substantially increased threshold current densities relative to lasers with a nominally identical structure without p-type doping. The thickness and position of the doping layer was investigated and the optimal was and found to be a 10nm layer, 15nm above the quantum well layer. This structure achieved high gain, and reduced the threshold current density relative to the undoped device above temperatures of $37\,^{\circ}\mathrm{C}$ in 1000μm long lasers and above $77\,^{\circ}\mathrm{C}$ in 2000μm long lasers. Ground state lasing was achieved at room temperature for uncoated facet broad area stripe lasers with cavity lengths as short as 400μm ($30.95\mathrm{cm}^{-1}$).

Two series of wafers were grown to investigate direct n-type doping. In the first instance, wafers were fabricated into mesa ridge lasers of different cavity lengths with identical structures with 10hpd p-type modulation doping and no doping. The direct comparison of the two doping strategies in nominally identical devices is novel and was published in the Journal of Physics D [1]. Doping with 1.2 electrons per dot (epd) was found to reduce threshold current significantly relative to undoped devices between $17\,^{\circ}\mathrm{C}$ and $97\,^{\circ}\mathrm{C}$. However, the direct n-type doping significantly narrowed the nearfield lasing spot, due to either changes in the alpha (Henry) parameter or side wall recombination loss. This resulted in modest improvements in threshold current density across the full temperature range in the longer 2000μm cavity lasers, which have lower gain requirements. In contrast, the p-type modulation-doped lasers were found to have a better performance in regimes of higher gain requirements: shorter cavity lengths and higher temperatures. This came at the expense of significantly increasing the threshold current density in lower

temperature ranges 17 °C – 57 °C.

P-type modulation doping improved the characteristic temperature (T_0), a measure of the temperature dependence of the threshold current density. For a p-type modulation doped device with a 2000μm cavity length and a 25μm mesa width, T_0 was found to be 414.9 K from 17 °C to 57 °C and 155.5 K from 57 °C to 97 °C, compared to 70.2 K and 74.0 K for the undoped and direct n-type doped devices respectively across the whole temperature range.

P-type modulation doping also delayed switching of lasing from the ground to excited state compared with the undoped device. A 500μm cavity laser with p-type modulation doping achieved ground state lasing at 77 °C compared to 67 °C for an undoped device. Direct n-type doping had the opposite effect, causing the state switch to occur at a lower temperature and the device ground state lasing up to a temperature of 37 °C.

A second series of wafers was grown with 0, 1.2, 2.4 and 4.8 epd direct n-type doping. Doping with 4.8epd was found to reduce the threshold current density in both 1000μm and 2000μm cavity lengths. Here the nearfield width was not reduced. In 1000μm ridge lasers, direct n-type doping with 4.8epd reduced threshold current from 245Acm^{-2} to 190Acm^{-2} at 27 °C and 731Acm^{-2} to 603Acm^{-2} at 97 °C, compared to the undoped device.

A novel technique of co-doping devices with both p-type modulation doping and direct n-type doping simultaneously was investigated and was demonstrated to greatly improve performance. Co-doping with 10hpd and 1.2epd was found to reduce the threshold current density to a greater extent than either approach individually, lowering threshold current density from 245Acm^{-2} to 132Acm^{-2} at 27 °C and 731Acm^{-2} to 312Acm^{-2} at 97 °C, compared to the undoped device. Co-doping retained the advantage of reduced temperature dependence from the p-type modulation doping and, due to the greater amount of p-dopant than n-dopant. For 1000μm long lasers, the characteristic temperature (T0) is 64.0K for the undoped device, which is increased to 81.3K by the addition of co-doped, compared with 60.6K and 115K for 4.8epd direct n-type doping and 10hpd p-type modulation doping respectively. Co-doping extended the range of conditions (cavity lengths and temperatures) over which ground state lasing could occur relative

to undoped and direct n-type doped devices.

7.2 Further Work

Co-doping shows great promise in reducing the threshold current density in InAs quantum dot lasers. Measurements of the absorption spectra of wafers for the samples discussed in Chapter 6 by the segmented contact approach would allow further examination of the effect of the direct n-type doping and co-doping on the dot distribution.

Building on the effects observed in Chapter 5.6 relating to the unusual nearfield of some n-doped devices, it might be interesting to study structures with different levels of n-doping using broad area laser structures.

The level of co-doping examined in Chapter 6 exhibited excellent results, but this may be possible to improve this further by optimising the ratio of the p-modulation and n-direct doping. In Chapter 5, increasing the amounts of direct n-type doping reduced the threshold current density, so higher levels of doping may increase the effectiveness of co-doping in lowing the threshold current density. Increasing the level n-type doping may not have an effect on the temperature dependence of the threshold current density, as this effect is governed by the p-type modulation doping, and it would be beneficial to establish this experimentally. However, increasing the n-type doping would most likely reduce the temperature at which ground state lasing could occur.

P-type modulation doping is thought to improve the lifetime for laser structures grown directly on silicon due to the lowering of the quasi Fermi levels which increase confinement within the dots and reduce the likelihood of electrons entering defect states, where their recombination drives degradation. Lower carrier density is demonstrated elsewhere reduce degradation. Whilst direct n-type doping lowers threshold current density, it also raises the quasi Fermi levels, potentially reducing charge carrier confinement. This may result in reduced lifetimes and would make an interesting study.

Co-doping with 10hpd and 1.2epd achieved significant reductions in threshold current density and due to the lower amounts of direct n-type doping compared to p-type modulation doping, which may overall

increase carrier confinement in the dots, which alongside the lowed carrier density, has potential to extend laser lifetimes. The reduced threshold current density across a large temperature range makes it an attractive candidate for integration. Optimising the relative amounts of dopant per dot with a smaller proportion of n-dopant than p-dopant, co-doping could be a potential solution to low threshold current density, energy efficient lasers with long lifetimes for silicon photonics.

References

[1] H. Deng, L. Jarvis, Z. Li, Z. Liu, M. Tang, K. Li, J. Yang, B. Maglio, S. Shutts, J. Yu, L. Wang, S. Chen, C. Jin, A. Seeds, H. Liu, and P. M. Smowton. "The role of different types of dopants in 1.3 μm InAs/GaAs quantum-dot lasers". In: *Journal of Physics D: Applied Physics* 55.21 (May 26, 2022).